Evaluation of the Unsteady Propeller Performance behind Ships in Waves

Vom Promotionsausschuss der
Technischen Universität Hamburg-Harburg
zur Erlangung des akademischen Grades

Doktor-Ingenieurin (Dr.-Ing.)

genehmigte

Dissertation

von
Dipl.-Ing. Katja Wöckner-Kluwe
aus Hamburg

2013

Vorsitzender des Prüfungsausschusses:

Prof. Dr.-Ing. Alexander Düster

Gutachter:

1. Gutachter: Prof. Dr.-Ing. Moustafa Abdel-Maksoud
2. Gutachter: Prof. Dr.-Ing. Stefan Krüger

Zusätzliche Gutachter:

Prof. Dr.-Ing. Alexander Düster
Prof. Dr.-Ing. Thomas Rung

Tag der mündlichen Prüfung:

25. 04. 2013

Technischen Universität Hamburg-Harburg
Schwarzenbergstraße 95c
D-21073 Hamburg

Bericht Nr.: 667

ISBN 978-3-89220-667-5

Abstract

Existing computational methods for the design of ship propellers and for the determination of ship-propeller interaction effects only consider the situation in calm water. The propeller is considered to be deeply submerged in all situations and unsteady influences on the operating conditions of the propeller are usually not considered. Oppose to this, a ship operating in heavy seas generates highly unsteady working conditions for the propeller. For typical merchant ships, providing large draughts, the common procedure is sufficient, as the propeller is always deeply submerged. But for smaller vessels, especially for those operating in dynamic-positioning mode (i.e. offshore-supply vessels), the influence of the ship motions and the waves on the propeller should be considered. Due to the large propeller loading in such situations and the small draught of these vessels, the propeller might start to ventilate, which causes large load fluctuations. In the present work a computational procedure is derived, which allows to compute the unsteady working conditions of a propeller in a ship wake under consideration of the wave influence. The method is based on a close and unsteady coupling of a viscous-flow method and a method based on potential-flow theory. Therein, the RANS method is used to compute the flow around the ship hull and therewith the inflow conditions for the propeller, while the inviscid-flow method is used to determine the propeller forces. These forces are afterwards used to model the propeller inside the RANS method by transferring them into a set of equivalent body forces. Henceforth, the influence of the propeller on the flow is considered, but the propeller does not need to be modelled geometrically, which reduces the computational effort significantly. For the computation of the propeller-ship interaction during operation in waves, this procedure is supplemented by a second coupling approach for an efficient wave description. Within this procedure, the RANS method is coupled to an inviscid determined wave description in the far field, which allows the use of very compact domains for the simulation of ship motions in waves and reduces the necessary amount of cells and therefore computational time.

Kurzfassung

Bisherige Berechnungsansätze zu Auslegung und Entwurf von Schiffspropellern und zur Bestimmung der Rumpf-Propeller-Wechselwirkungen berücksichtigen nur Situationen im Glattwasser. Der Propeller ist dabei stets tief getaucht und instationäre Einflüsse auf die Arbeitsbedingungen des Propellers werden nicht berücksichtigt. Operiert das Schiff dagegen im Seegang ändern sich die Anströmbedingungen des Propellers ständig. Für konventionelle Handelsschiffe mit großem Tiefgang ist das bisherige Vorgehen in der Regel ausreichend. Für kleinere Schiffe, die zudem häufig dynamisch positionieren, wie z.B. Plattformversorgungsschiffe ist es dagegen wichtig, die instationären Einflüsse des Seegangs auf den Propeller zu berücksichtigen. Bedingt durch den kleineren Tiefgang dieser Schiffe und die hohe Propellerbelastung bei geringer Fahrt kann der Propeller anfangen zu ventilieren, wodurch große Belastungsschwankungen für den Propeller entstehen. Inhalt der Arbeit ist daher die Entwicklung eines Verfahrens, mit dem die hydrodynamischen Eigenschaften von Propellern im Schiffsnachstrom unter Berücksichtigung des Seegangseinflusses untersucht werden können. Kern des Verfahrens ist eine instationäre Kopplung einer RANS-Methode mit einer Methode, die von einer reibungsfreien Strömung ausgeht. Die RANS-Methode wird dabei verwendet, um die Umströmung des Schiffes und damit die Anströmbedingungen des Propellers zu bestimmen, während die Methode für reibungsfreie Strömung eingesetzt wird, um die Propellerkräfte zu berechnen. Diese Kräfte werden innerhalb der RANS-Methode in ein 3D-Feld von Volumenkräften umgewandelt, welches in der Propellerposition aufgebracht wird. Mit Hilfe dieses Kraftfeldes kann die Wirkung des Propellers auf die Strömung simuliert werden, ohne die Geometrie des Propellers explizit zu modellieren, wodurch sich der Berechnungsaufwand deutlich reduziert. Zur Simulation der Propeller-Schiff-Wechselwirkung im Seegang wird dieser Algorithmus mit einem zweiten Kopplungsansatz zur effizienten Berechnung des Wellenfeldes kombiniert. Diese zweite Kopplung kombiniert ein reibungsfrei bestimmtes Wellenfeld im Fernfeld des Schiffes mit der viskos berechneten Wellenerhebung in der Nähe des Schiffes. Auf diese Weise können für die Simulation der Schiffsbewegungen sehr kleine Berechnungsgebiete verwendet werden wodurch die Rechenzeit sinkt.

Acknowledgements

This thesis is based on my work as research assistant at the Institute of Fluid Dynamics and Ship theory of the Hamburg University of Technology. First of all I would like to express my gratitude to Prof. Dr.-Ing. Moustafa Abdel-Maksoud, who offered me the opportunity to work in his team and who supported my work with fruitful suggestions and great encouragement.

Secondly I would like to thank Prof. Dr.-Ing. Stefan Krüger for being the second evaluator of this thesis, as well as the additional evaluators Prof. Dr.-Ing. Alexander Düster and Prof. Dr.-Ing. Thomas Rung for their work. Additionally I would like to thank Prof. Dr.-Ing. Thomas Rung for his great support during the development of this thesis and Prof. Dr.-Ing. Alexander Düster for chairing the doctorate commission.

The work on this thesis was carried out as part of the MARTEC research project "Propulsion in Seaways" (PropSeas), which was funded by the German Federal Ministry of Economics and Technology (BMWi) and the Research Council of Norway.

Special thanks are due to my colleagues at the institute M8 for the good working atmosphere and the helpful and fruitful discussions throughout the years. Namely, I would like to mention Dipl.-Ing Niels Alexander Lange, who shared the office with me for almost five years, Dipl.-Ing. Martin Greve, who worked with me in the research project PropSeas and last but not least the whole FreSCo team.

A warm word of thanks goes to my family (the Wöckner and the Kluwe side) for the manifold encouragement and to my son Maximilian, who enriches my life very much. Thank you Florian for the good time we have and had together, for your never ending and extensive support not only during my time as research assistant, but also during my studies and for your idea to move to Nortorf.

Contents

List of Figures

List of Tables

List of Symbols

α	Blade angle of attack
α	Shape function
β	Amplitude parameter
$\beta\,, \beta_i$	Hydrodynamic pitch angle
Δ	Displacement of ship
δ	Geometric pitch angle
δ_{ij}	Kronecker delta
$\hat{\zeta}$	Wave amplitude
$\tilde{\zeta}$	Time independent wave amplitude
η_0	Open water efficiency
η_{IA}	Ideal efficiency
θ	Pitch angle of ship
λ	Scale factor
λ	Wave length
μ	Dynamic viscosity
μ	Encounter angle
μ_T	Turbulent viscosity
ν	Kinematic viscosity
ξ	Position inside transition zone
ρ	Fluid density

σ_j	Source strength at panel j
τ_j	Dipole strength at panel j
τ_i	Regression parameters
Φ	Velocity potential
ϕ	Arbitrary transport variable
ϕ	Perturbation potential
ϕ^*	Variable value according to wave theory
ϕ_∞	Potential of the steady inflow velocity
$\mathbf{\Omega}$	Matrix of rotation
$\boldsymbol{\omega}$	Angular velocity
ω	Dissipation rate of turbulence
ω	Frequency of rotation
ω	Wave frequency
ω_e	Encounter frequency
A_0	Area of the propeller disc
A_j	Surface area of panel j
$A_k\,, B_k$	Fourier coefficients
$A_{_P}$	Central matrix coefficient
$A_{_{NB}}$	Matrix coefficients of the neighbouring cells
$\mathbf{b}$	Body force vector
B	Breadth
c	Mixture fraction
c	Wave celerity
c_A	Correlation coefficient
c_F	Frictional resistance coefficient

c_p	Pressure coefficient
c_{TH}	Thrust loading coefficient
Co	Courant number
D	Propeller diameter
dt	Time step size
e_i	Euler parameters
F_n	Froude number
F_{DA}	Friction deduction force
$\mathbf{f}$	Vector of forces
g	Gravitational constant
H	Draft of the propeller shaft
H_W	Wave height
$\mathbf{J}$	Tensor of inertia
J	Advance coefficient
k	Turbulent kinetic energy
k	Wave number
k_Q	Torque coefficient
k_T	Thrust coefficient
L	Length
L_{pp}	Length between perpendicular
LCG	Longitudinal centre of gravity
$\dot{m}$	Mass flux
$\mathbf{m}$	Vector of moments
n	Number of revolutions
n	Surface normal vector

N_B	Number of body panels
N_W	Number of wake panels
P	Propeller pitch
P_D	Delivered power
P_e	Power to tow the ship
Q	Propeller torque
$\mathbf{r}$	Distance vector
R	Propeller radius
r	Radial coordinate
R_e	Reynolds number
R_T	Ship resistance
S	Cell surface
S	Surface tension of the fluid
S	Wetted surface of the ship hull
S_ϕ	Source term
$\mathbf{T}$	Stress tensor
T	Draught
T	Propeller thrust
t	Thrust deduction fraction
t	Time
T_e	Encounter period
TZ	Transition zone
u_0	Axial velocity in propeller plane
$\mathbf{v_B}$	Velocity due to grid movement (vector)
$\mathbf{v_E}$	Interaction velocity

$\mathbf{v_I}$	Induced velocity
$\mathbf{v_N}$	Nominal wake velocity
$\mathbf{v}$	Velocity vector
V	Cell volume
v	Velocity of a vessel
v_A	Volume averaged velocity in propeller plane
v_M	Model speed
v_S	Ship speed
VCG	Vertical centre of gravity
w	Wake fraction
W_e	Weber number
$x\,,y\,,z$	Cartesian coordinates
$\mathbf{x_G}$	Centre of gravity (vector)
y^+	Dimensionless wall distance

1 Aims and Motivation

Numerical methods developed for the investigation of propeller flows usually consider only deeply submerged propellers in calm water. This applies both to methods based on potential-flow theory as well as to viscous-flow methods, whereas the former are mostly used for the design process of a propeller. Therein, the propellers typically works in unconfined flows and the operating conditions for the propeller are considered by applying a previously computed wake field as inflow condition. As viscous effects are crucial for an accurate prediction of the wake field, the input for the potential-flow method has to be determined experimentally or by using viscous-flow methods. Henceforth, an interaction of ship and propeller is typically not directly considered. Due to the recent growth of computer capacities, viscous-flow methods are now used for the simulation of propeller flow as well. But analogues to inviscid-flow methods, the typical procedure considers the propeller in deeply submerged conditions and separates the investigation of ship and propeller. This follows from the assumption that the propeller is deeply submerged in all situations. Then, the main oscillations in the blade loads result from the variation in the wake field (i.e. deviations in the blade angle of attack). The influence of the free surface is negligible. Empirical safety factors are applied to account for an influence of waves.

However, recent investigations show that the load variations of the propeller blades due to waves are much larger than for a long time assumed and what was covered by the safety factors. In heavy seas, the ship motions lead to large variations in the wake field, which rapidly changes the operating conditions for the propeller. Additionally, the fluid density changes by a factor of a thousand, if a blade pierces the water surface. This phenomena known as ventilation, has progressively moved into the focus of research groups due to the increased occurrence of damages on the propulsion systems during the last few years (for example at the gear). These damages are caused by the large thrust variations during a ventilation event. As a result of the damage, the ship may loose its ability to manoeuvre and a safe return to port is not possible under all circumstances. Furthermore, economic losses for shipping companies might be an indirect result of ventilation due to more frequent repairs and therefore, increased operational costs. Especially offshore-supply vessels are found to be at risk for ventilation, since the high propeller loadings during dynamic positioning facilitate the occurrence of ventilation. As this ship type has become more important in the last years due to the increased use of energy resources

from offshore (i.e. wind farms and oil platforms), the importance of an investigation of ventilation increases.

This indicates the demand for new or extended numerical methods, which allow investigations of ship-propeller interaction in waves to estimate the expected load variations during typical operating situations. Thus, the aim of this thesis is to develop a procedure for the simulation of ship-propeller configurations, that is also able to predict the interaction of the propeller with the free surface. Although the capacities of numerical methods have increased during the last years, the challenge of using simulation methods for the investigation of ship-propeller interaction is still very large. On one hand, methods based on potential-flow theory are not able to predict the ship's wake with a sufficient level of accuracy. On the other hand viscous-flow methods (i.e. RANS) are afflicted with large computational costs, especially if the ship motions in waves need to be simulated. However, the simulation of the ship motions with a viscous-flow method is necessary to determine the wake variations in waves and to determine the interaction of the free surface and the propeller. To overcome this dilemma, a computational procedure is developed within the scope of this work, which aims to combine the advantages of potential-flow methods (i.e. small computational times) with the accuracy of viscous-flow methods in a close-coupling algorithm. This coupling procedure shall be able to capture unsteady interaction effects between the hull and the propeller as well as ventilating (surface-piercing) propellers. Here, a RANS method is used for the simulation of the ship motions and with it the computation of the working conditions of the propeller. The inviscid-flow method then uses the calculated flow conditions as input to calculate the propeller forces. Afterwards, these forces are used to model the propeller in the RANS method. Secondly, an approach for efficient RANS based sea-keeping simulations is derived. Within this supplemental method, the RANS method is coupled to an inviscid wave description, which allows the use of very compact domains for the simulation of ship motions in waves and reduces the necessary amount of cells and therefore computational time.

The present thesis is structured into the following parts. The next chapter gives an overview on the relevant physics in propeller flows. Afterwards, available computational methods, suitable for the simulation of ship and propeller and the interaction of both are presented. One section of this chapter describes already existing coupling approaches for ship-propulsion investigations. Additionally, this chapter presents the computational methods, which are used within this thesis. Focus of the fourth chapter is the development of the coupling procedure including a validation of the approach. The fifth chapter is dedicated to an investigation of ventilating propellers. Here, the capabilities of the RANS method *FreSCo*$^+$ and the coupling algorithm are analysed. The approach, which allows sea-keeping simulations in compact domains is described in chapter 6, before the last chapter gives an application example for the developed procedures.

2 Propeller flow physics and fundamentals of ship propulsion

The present chapter describes the relevant physics for ship propulsion and propeller flow. The first subsection summarizes the basics of propeller flow and gives an overview of the general terms and parameters. Here, aspects of ship propulsion are also described. The following subsection is dedicated to the influence of the free surface on the flow around propellers and gives a definition of the ventilation characteristics. The chapter is finalized by a summary of the main scale factors, as model tests are still important in the propeller design process. The focus of this chapter is to give a brief overview of the specifics of propeller flow and to introduce the main propulsion parameters. A more detailed overview of the relevant aspects can be found in Krüger [52] and Bertram [8].

2.1 General aspects

Propellers are the most common propulsion system for ships. Although other forms exist, like Voith-Schneider propellers (Palm et. al. in [65]) or water jets, this thesis is mainly concerned with conventional non-ducted screw-propellers. Generally, propellers can be subdivided into two categories, the fixed-pitch and the controllable-pitch propellers. The simulations in the later chapters will only address fixed pitch propellers, even though in principle the computational methods are also able to simulate controllable-pitch propellers.

Typically, the propeller and the ship are treated separately in many stages of the design process (numerical and experimental), but the interaction of both is very important to cover all relevant characteristics and interaction effects. A working propeller behind a ship generates an additional resistance, compared to the resistance of the bare-hull by increasing the flow velocities and decreasing the pressure on the aft-body of the ship (Krüger [52]). Thus, the thrust (T) delivered by the propeller has to be larger than the resistance (R_T). The difference is typically expressed by the thrust deduction fraction:

$$t = 1 - \frac{R_T}{T}\,. \tag{2.1}$$

As the propeller is typically located behind the ship, the hull shape of the ship has a large influence on the flow towards the propeller. The resulting ship's wake is influenced by various effects, which can be divided into three main parts. Firstly, the potential wake is the wake field that would be generated by a floating body in an inviscid fluid featuring small axial velocity components near the stagnation points directly in front and behind the body. Lateral of the ship's hull the flow is accelerated. Secondly, also the wave system of a ship influences the velocities in the propeller plane due to the orbital velocities and the change of pressure in a wave crest or wave trough situation. These two effects are typically small and can also be predicted by potential flow methods as described in Carlton [14]. However, the most important component is the frictional wake. This component considers the behaviour of the flow in the boundary-layer region due to viscous effects. In addition, possible flow separation and the generation of vortices for example in the bilge region contribute to the frictional wake. Hence, only methods considering the viscosity of the fluid are able to investigate the wake. A more detailed description of the different influences on the wake can be found in Vorhölter [85].

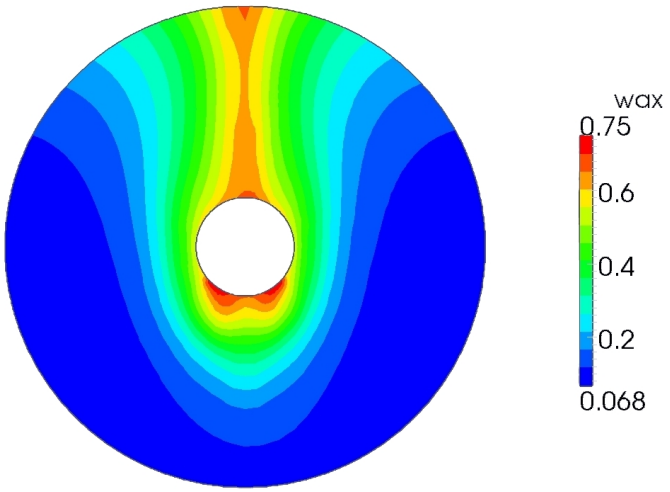

Figure 2.1: Typical nominal (axial) wake field in the propeller plane of a single screw ship. The influence of the ship's hull is clearly seen in the 12 o' clock position.

Figure 2.1 shows a typical wake field of a single-screw ship. The footprint of the hull can be clearly seen in the upper part of the propeller disc and in the vicinity of the stern tube. Overall, the velocity is lower than the ship speed in the wake of a ship. Especially in regions close to the ship's surface, large velocity losses can be observed. The figure is obtained from a RANS (**R**eynolds **A**veraged **N**avier **S**tokes) computation with the solver described in section 3.4 and shows a nominal wake field, as no operating propeller is considered in the calculation. The nominal wake is an important input for the design of wake adapted propellers and is the subject of many design optimization studies as for

example presented in Stück et.al [84]. The target function for such studies is typically based on a criterion that quantifies the non-uniformity of the wake. Further details about such criteria can be found for example in Fahrbach [26].

Of course, the operating propeller changes the velocities in the propeller plane. Then, the wake is referred to as effective wake field. Generally, the corresponding non-dimensional mean wake value is expressed by a single parameter, the wake fraction, which is calculated as follows:

$$w = 1 - \frac{v_A}{v} \,. \tag{2.2}$$

Here, v_A is the volume averaged velocity in the propeller plane, while v is the velocity of the vessel. Usually, the wake fraction is not determined from an analysis of the velocity distribution in the propeller plane, but results from the traditional model test procedure. Within this procedure the propeller is first investigated in open water conditions without the ship and afterwards in a self-propulsion test together with the ship. During an open water test, the propeller is mounted on an open water test rig, where the propeller operates in quasi-stationary conditions. Thereby, the number of revolutions is kept constant, while the inflow velocity is stepwise varied or vice versa. These tests are typically performed in a towing tank or in a "closed" cavitation tunnel. In both cases free surface effects are not considered as the propeller is deeply submerged during the test in the towing tank. Despite this, the parameters are scaled according to Froude's law. This results in a smaller number of revolutions compared to a scaling according to Reynolds law. Further remarks regarding the scaling laws can be found in subsection 2.3. The result of this experiment is the open-water diagram. In such a diagram, the thrust (T) and torque (Q) values of the propeller are plotted in a non-dimensional form over the advance coefficient as shown in fig. 3.1, where k_T and k_Q are defined as follows:

$$k_T = \frac{T}{\rho n^2 D^4} \quad \text{and} \quad k_Q = \frac{Q}{\rho n^2 D^5} \,. \tag{2.3}$$

In these relations, n refers to the number of revolutions and D is used for the propeller diameter. Furthermore, the so-called open water efficiency, which is an important parameter to determine the required power for a certain thrust, can be obtained from such an experiment. This parameter describes the relationship between the thrust power (Tv_A) and the delivered power $(2\pi nQ)$, which can also be expressed in terms of k_T and k_Q and the advance coefficient J:

$$\eta_0 = \frac{T \cdot v_A}{2\pi n Q} = \frac{k_T}{k_Q} \frac{J}{2\pi} \,. \tag{2.4}$$

Afterwards (and after a resistance test), the interaction parameters (thrust deduction fraction and (effective) wake fraction) can be determined from a self-propulsion test. During this experiment the propeller is mounted on the ship, which is self propelled. In the continental method the number of revolutions of the propeller is adjusted until the

required ship speed is achieved. Due to the larger frictional resistance in model tests, the propeller loading of the model propeller is higher compared to the full scale one. To unload the propeller, an additional towing force is applied in the experiment which leads to a reduction of the model resistance in eq. 2.1. This friction deduction force is calculated according to

$$F_{DA} = \frac{\rho}{2} v_M^2 S_M (c_{FM} - c_{FS} - c_a) \,. \tag{2.5}$$

In this formula, the index M refers to model scale parameters and the index S to full-scale values, respectively. The parameter S contains the wetted surface of the hull, ρ is used for the water density and c_a is a correlation coefficient determined by the respective model basin. The frictional resistance coefficient (c_F) is determined according to the ITTC 1957 [23] model-ship correlation line:

$$c_F = \frac{0.075}{(log_{10}(R_e) - 2)^2} \,, \tag{2.6}$$

where R_e is the Reynolds number. The thrust deduction fraction then results from the comparison of resistance test to propulsion test. Comparing the working conditions of the propeller behind the hull and in open water conditions, the wake fraction as defined in eq. 2.2 can be determined. Therefore, the principle of thrust identity is usually used. Following that approach, it is assumed that the propeller in the propulsion test generates the same thrust as in the open water test. Then, a corresponding advance coefficient for the given thrust can be determined from the open water diagram and the velocity in eq. 2.2 can be estimated $(v_A = JnD)$. The propulsion test finally results in the delivered power (P_D) and the propulsive efficiency (η_D) as shown in this formula:

$$P_D = \frac{P_e}{\eta_D} = \frac{R_T v_s}{\eta_D} \quad \text{with} \quad \eta_D = \frac{1-t}{1-w} \frac{T v_a}{2\pi Q_0 n} \frac{Q_0}{Q} \,. \tag{2.7}$$

In this equation P_e refers to the necessary power to tow the ship, which is obtained from the resistance test. The propulsive efficiency (η_D) contains of three parts: The hull efficiency, the open water efficiency and the relative rotative efficiency, which are a result of the different tests in the traditional model test procedure. These parts are especially important for the scaling of the results to the full scale ship. More details on the relevance of the individual contributions to the propulsive efficiency can be obtained from Krüger in [52].

Back to the importance of the effective wake, it can be noted that w is an important parameter to determine the required power, but the corresponding effective wake field can not be directly measured. Computational approaches considering the ship and the working propeller together are in principle able to compute the influence of the propeller on the wake, but it is difficult to separate the approach flow, the induced velocities and the interaction of the induced velocities. Per definition the effective wake contains

the interaction effects between ship and propeller, but it does not contain the induced velocities. As a result of this, the nominal wake field is commonly used for the design of the propeller blades, even though the influence of the propeller on the velocities in the propeller plane is not considered. However, in many cases more detailed investigations of the working conditions for the single blades in unsteady operation conditions are necessary to capture the interaction parameters of the propeller and the approach flow. This is important for propellers in off design conditions, for example operating in heavy seas, where ventilation can occur as described in section 2.2. For a detailed analysis of the propeller forces in situations like this, the large variations in the blade angle of attack a blade faces during one rotation should be taken into account.

In the following, the flow around the propeller blades shall be described in more detail. In principle, a propeller blade is a lift producing foil. The lift is generated by a set of bounded vortices, the strength of these vortices varies along the radius. According to the Helmholtz law a set of free vortices is therefore generated in the wake of each blade. The strength of the free vortices complies with the variation of the bounded vortices along the radius. Applying then the law of Biot-Savart each vortex generates a rotating velocity field. To illustrate the basics of the flow around lifting floating bodies, two examples are displayed in fig. 2.2.

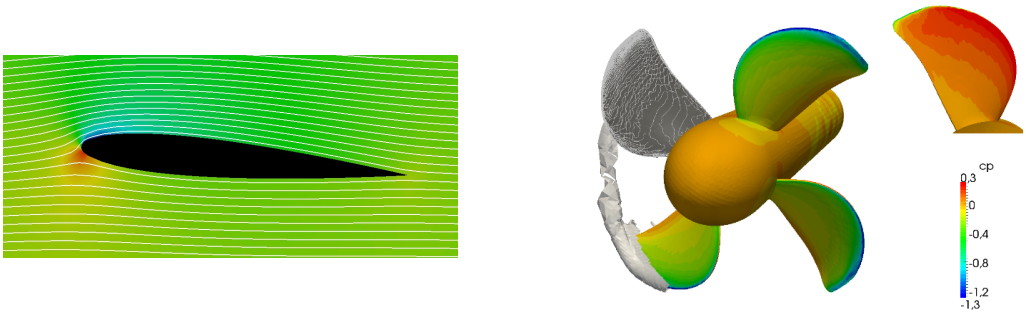

Figure 2.2: Pressure distribution and streamlines of the velocity vector around a two-dimensional hydrofoil (NACA0012) (left) and results for a simulation of a deeply submerged propeller (right). Both figures are obtained from *FreSCo*$^+$ computations.

The left picture depicts a two-dimensional deeply submerged hydrofoil. The foil has a moderate angle of attack of 5°. In this figure, the flow is coloured with the resulting pressure distribution around the foil. Thereby, the red colour marks the maximal pressure, while small pressure values are displayed in blue. Additionally, the stream lines of the velocity vector are illustrated to visualise the flow. A stagnation point is located at the leading edge. Here, the velocity is reduced to zero, while a maximum value is obtained

for the pressure. Due to the Bernoulli equation the flow is accelerated at the suction side of the profile, while values smaller than the inflow velocity can be found at the pressure side. The second example shows a deeply submerged fixed-pitch propeller. Three blades and the hub are coloured with the pressure coefficient (c_p), which is computed as follows:

$$c_p = \frac{p}{\rho/2(v_A^2 + (2\pi n R)^2)} \,. \tag{2.8}$$

Here, p refers to the pressure and R describes the radius of the propeller. The investigated propeller operates in pulling mode. According to this, the suction side of the propeller is visible. The single blade on the right illustrates the pressure distribution on the pressure side. At one blade also the tip vortex is visualised by an ISO-surface for the magnitude of the vorticity vector. Analogues to the two-dimensional example, large pressure values can be found at the leading edge of the pressure side, while the suction side shows small pressure values at the leading edge. On the fourth blade ISO-lines of the shear stress vector, indicating the local flow direction are depicted.

The amount of lift and therefore thrust depends on the effective blade angle of attack (α).

$$\alpha = \delta - \beta_i \,, \tag{2.9}$$

which itself depends on the geometry of the foil and the actual flow condition as illustrated in fig. 2.3 on the left hand side. The angle δ is defined by geometric properties, as this angle describes the pitch of the specific blade section. The pitch (P) is defined as advance distance of a blade section at a specific radius (r) during one rotation:

$$\delta(r) = atan(\frac{P}{2\pi r}) \,. \tag{2.10}$$

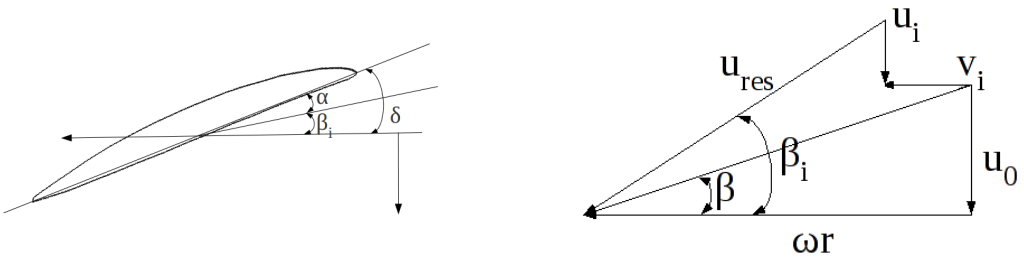

Figure 2.3: Illustration of the relevant angles and velocities at a 2-dimensional foil. The left picture explains the definition of the angles, while the right figure illustrates the velocities in the propeller plane.

The second angle β is defined from the velocities in the plane of the profile as shown in fig. 2.3 on the right. Without a consideration of the propeller induced velocities, this

so-called hydrodynamic pitch angle is defined as:

$$tan\beta = \frac{u_0}{\omega r}\,, \tag{2.11}$$

where u_0 is the inflow velocity towards the propeller in axial direction, and $\omega \cdot r$ refers to the rotational velocity of the propeller, with ω being the frequency of rotation. Another formulation of this relation leads to the equation for the advance coefficient, which is one of the central parameters to compare the performance of different propulsors:

$$J = \frac{v_A}{nD}\,. \tag{2.12}$$

Of course the propeller itself influences the velocities in the propeller plane and so the above described is a strong simplification. Due to the induced velocity components (u_i, v_i) the angle β is changed to β_i as illustrated also in fig. 2.3. The produced thrust is a function of the angle of attack, as an increasing value for α increases the lift until the stall angle is reached and the flow separates from the suction side of the propeller blade. The magnitude of the variations in the blade angle of attack in a wake field can be quite significant over one rotation of the blade, as illustrated in fig. 2.4. The shown example is obtained with *FreSCo*$^+$ for the single-screw ship in fig. 2.1. In contrary to the simulation before, the operating propeller is now considered. In this example the differences between the minimum and maximum value of the angle of attack are nearly 8°. But smaller appendages like pod struts or misaligned shaft bracket arms of twin-screw ships can easily generate much larger variations in the blade angle of attack. Thus, one can imagine that depending on the flow situations large oscillations in the lifting force can occur during one rotation, which can also lead to flow separation.

Moreover, due to waves and manoeuvres and the resulting changes in the wake velocities much larger fluctuations in the blade angle of attack can occur compared to the design condition in calm water. Hence, the analysis of ship propulsion in waves and during manoeuvres is an important aspect for ship safety and can reduce the fuel consumption. Some approaches to determine the change of propulsion characteristics in waves are presented by Faltinsen in [28]. Next to analysing the added resistance in waves, the author investigates the change in the wake velocities due to waves. Analogues to other authors, he found the pitch-motion to be a major reason for increasing wake velocities in waves. Additionally, he analysed how the open water values also for the non-ventilating propeller, decrease in waves. More details on the influence of ventilation on the propeller performance are given in the following section. Summarized, all the investigated effects will lead to a change in the propulsive efficiency in eq. 2.7. Measurements of propellers in waves and especially of the corresponding single blade values are very rare. Thus, computational methods are required to investigate this. They also provide the possibility to perform full scale predictions. In the following chapter computational methods are described which can be used to predict the propulsive efficiency as well as the open water performance. Additionally, the methods used in this thesis are described.

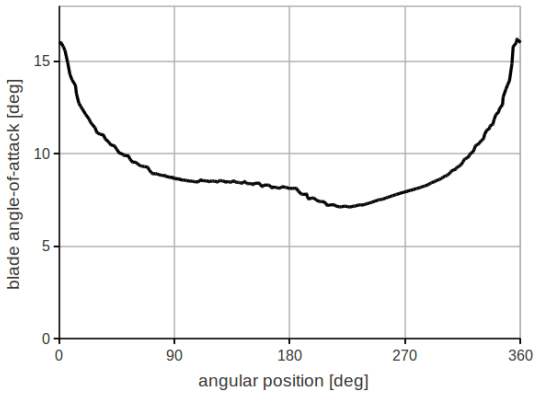

Figure 2.4: Variations in the blade angle of attack over one rotation. The results are obtained from a *FreSCo*$^+$ calculation, where the same ship as in fig. 2.1 is investigated but now with operating propeller.

2.2 Ventilation

Ventilation is one of the most critical issues a propeller can face in waves and it can cause very large thrust losses for the whole propeller. Furthermore large load fluctuations at the single blades are observed. Traditionally, propeller ventilation is only investigated for surface-piercing propellers. But ventilation can also occur at propellers, which are fully submerged in the initial stage, whilst the ship is operating in heavy seas and where large relative motions between the vessel and the free surface arise. At normal merchant vessels with large draughts, ventilation is relatively uncommon, but for smaller ships and therefore smaller draughts, ventilation can become critical. The problem is especially known from offshore supply vessels and other ships in dynamic positioning conditions, where the propeller operates close to the bollard pull condition, so that the propeller is highly loaded. Thus, the problem is becoming more important during the last years, due to the more intensive use of offshore installations for the production of energy as described in Califano [11].

Ventilation is defined as a situation, where the propeller or only parts of the blades are working in air. This might be the case if a blade emerges or in case the propeller is operating in aerated waters. Hence, not only situations, where the propeller emerges are critical but also working conditions of the propeller in the vicinity of the free surface can cause ventilation. In such cases it might happen that the propeller sucks down the free surface or the propeller forms a funnel connecting the free surface to the blade. The funnel is generated by a vortex filled with air and air is transported to the blades as described by Kozlowska in [49]. In this condition, the parts of the blades where the pressure becomes

smaller than the atmospheric pressure ($p < p_0$) start to ventilate. Hence, two conditions are found for the occurrence of ventilation by Califano in [11]. Firstly, the connection between the free surface and the blade and secondly the small pressure values on the suction side of the blade surface. As the suction side is responsible for more than 60% of the generated thrust, large thrust losses are expected during a ventilation event. The parts of the propeller which are ventilated, deliver more or less no thrust and torque. This is for example investigated analytically by Isay [38] and experimentally by Koushan [44]. The latter describes load variations from 0% to 100% between ventilated and non-ventilated conditions. Furthermore, he describes the destructive character of ventilation, especially when the blades come out of the water during one revolution of the propeller. Especially the combination of low-frequency fluctuations due to the ship motions and high frequency fluctuations due to the motion of the blades are described to be the most harmful and destructive for the mechanical parts. During ship operation one can try to minimize the amount of ventilation by adjusting the propeller pitch or the number of revolutions to reduce the loading of the propeller, but this might lead to wear of the mechanical parts (i.e. the gear). Possible damages are for example reported in Califano [11].

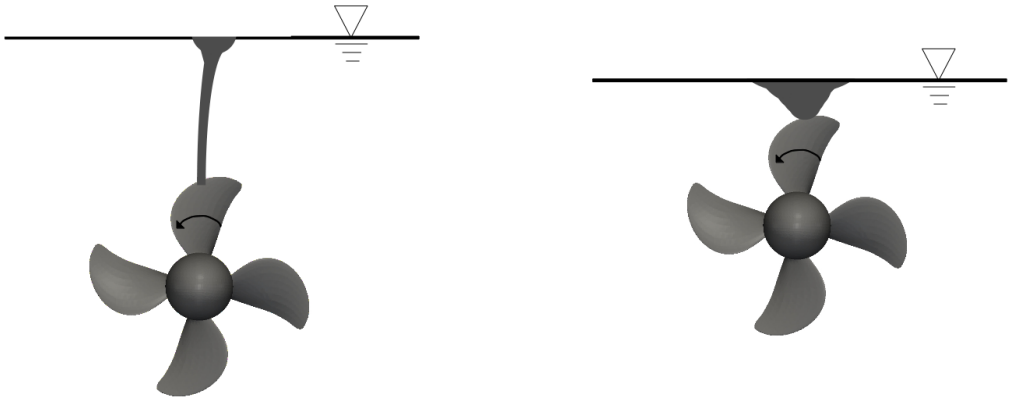

Figure 2.5: Explanation on the different ventilation inception mechanisms. The left figure shows ventilation through an air-filled vortex, while in the right figure the propeller sucks down the free surface.

Different mechanisms for the inception of ventilation are characterized by Kozlowska et. al. in [49]. The authors depict three modes in dependency of the static immersion ratio and the advance coefficient of the propeller. If the propeller operates in a certain distance below the free surface, an air-filled vortex is generated as displayed in fig.2.5 on the left hand side. This funnel connects the suction side of the propeller with the free surface, while the pressure side is still wetted. In the second condition, illustrated in fig.2.5 on the right hand side, the propeller is working close to the free surface. Despite the first condition the propeller starts to ventilate immediately after starting the model test by sucking down

the free surface. In addition, the authors describe an intermediate condition between the first two modes. After the inception phase, where only the downward moving parts of the blades are ventilated, the partial ventilation phase, illustrated in fig. 2.6 on the right, is characterized by some amounts of air-enclosure on all propeller blades. Finally, the authors observe a full ventilation phase, where all blades are completely covered by air independently from the inception mechanism. This ventilation form is depicted on the left hand side of the figure and results in the largest thrust and torque losses.

Figure 2.6: Illustration of different ventilation forms. The left photo shows a fully ventilated propeller, while the right picture depicts a partial ventilated propeller, obtained from a numerical simulation with *FreSCo*$^+$. The photo is taken from model tests at MARINTEK (Norway).

The sensitivity of ventilation on the advance coefficient is investigated during the experiments of Koushan [44]. He finds three different zones in an open-water diagram: The super-critical zone at the lowest advance coefficients, the sub-critical zone at the high advance coefficients and a critical zone between the first two. In this intermediate zone, the occurrence of ventilation depends on the starting point. If the advance coefficient is reached from the supercritical zone (i.e. the inflow velocity is increased), the ventilation remains stable. On the other hand, reaching this zone from larger advance coefficients, ventilation starts at lower advance coefficients. Thus, a hysteresis phenomena can be observed.

The first experiments on propeller ventilation date back to the 1930's, where for example Kempf [39] investigated thrust and torque losses due to ventilation. The dependency of ventilation from the different propeller design parameters was investigated during the 1950's by Shiba [76]. He performed systematically model tests to analyse the influence of the expanded area ratio, the propeller pitch or the skew. He also investigated the influence of the scale on ventilation. Other authors, like Fleischer [30] and Strunk [83] additionally analyse the influence of the ambient pressure. More recently, Koushan performs extensive model tests on thruster-type propeller units, as ventilation problems occur to an increasing

degree on offshore supply vessels equipped with thrusters. In these experiments mainly the bollard pull-condition is investigated, as this situation is found to be the most critical. Furthermore, he investigates ducted propeller [46] or the influence of waves [47] and [45]. All of his experiments show the highly unsteady character of ventilation, which makes the investigations very challenging. For example model test experiments performed by MARINTEK in Trondheim, published in Kozlowska [50] and Wöckner-Kluwe [89] show different ventilation phases for constant flow parameters. But model tests with systematically varied parameters are almost the only possibility to investigate the ventilation phenomena. Only very few examples for the use of computational methods for the investigation of propeller ventilation can be found in the literature. This is mostly due to the large computational effort and the difficulties to model the violent deformations of the free surface. One of the first attempts of simulating the interaction of the propeller with the free surface with RANS methods is the work of Caponnetto [13]. There, water exit and entry phases for surface piercing propellers are computed. Later on Califano and Steen [12] analyse the possibility to use viscous-flow methods for investigations of ventilation for conventional propellers. In this investigation, the authors study ventilation inception mechanisms with the commercial RANS method Fluent. They observe a good agreement in the amount of ventilation in the first half of the rotation, but less amounts of ventilation in the second half of the rotation compared to analogues model tests. It is assumed by the authors that the used grid is too coarse to cover all effects, because there is not enough available computational power. They determine the large computational times to be a limiting factor to compute all forms of ventilation. Another investigation can be found in Palm [65]. Here, the authors compare measurements and computations for a Voith-Schneider propeller and a Voith-Radial propeller, the latter being a ducted propeller. A good agreement is found in the predicted amount of ventilation and in the computed thrust losses. As the large computational times are the limiting factor for the use of viscous flow methods for the investigation of ventilation, potential flow methods are primarily afflicted with problems in modelling the ruptured deformations of the free surface. Accordingly, very few examples for the use of boundary element methods for the prediction of ventilation can be found in the literature. One example is the work of Young and Kinnas [92], where a boundary element method is used to simulate surface-piercing propellers.

Next to numerical simulations and experiments, various authors tried to determine the expected thrust losses by using empirical relations. In these approaches different formulas are used depending on the different ventilation forms and therefore, courses of thrust loss. Firstly, Fleischer [30] addresses the thrust losses due to a loss of disc-area of partly immersed propellers. Secondly, the Wagner-effect [86] contributes to the thrust losses. This effect describes the reduction of lift directly after the blade immerses again. According to Wagner, the lift of a foil is reduced to 50% of the nominal lift during an out-of-water event. After the blade immerses again the lift increases asymptotically to the fully de-

veloped lift during the next rotation. This assumption is applied by Faltinsen [28] and Koushan [44] for propellers . The latter founds that an immersing propeller blade has to fulfil about four rotations in fully submerged condition in order to recover the nominal thrust. Finally, an approximation for the thrust losses due to wave making of the propeller and ventilation can be found in Faltinsen [28]. The results of these empirical relations are compared to measurements in Kozlowska et. al. [49]. There, the authors found a reasonably good agreement between both.

2.3 Scale effects

Although the importance of numerical methods increases recently, model tests are still the most common approach to investigate ship propulsion aspects and propeller performance. To determine the respective data for the full-scale ship, the results have to be extrapolated and possible scale effects have to be handled with care. Especially due to the increasing ship dimensions in the last years, possible scale effects are becoming more important. This follows from the restrictions on the model sizes due to the existing dimensions of the model basins. Thus, the scale factor $\lambda = \frac{L_S}{L_M}$, describing the geometric similarity increases as well. Again, the index S is used for ship dimensions, while M refers to the respective model parameter. A very detailed analysis of scale effects for propeller flows is given by Müller in [61], where a literature review of existing scaling methods is presented, before a new approach based on viscous numerical simulations is derived. While the focus of Müller's work is to analyse scaling effects in the flow around deeply submerged open water propellers, the additional aim of this section is to discuss possible scaling aspects for propellers in behind condition as well as for ventilating propellers.

The most important laws for aspects of ship propulsion are Froude's law describing the ratio of body's inertia forces to the gravitational forces and Reynolds' law describing the ratio of inertial forces to viscous forces. Typically, the Froude number (F_n) is defined with

$$F_n = \frac{v}{\sqrt{gL}} \quad \text{and} \quad R_e = \frac{vL}{\nu} \tag{2.13}$$

is the Reynolds number. In these equations L refers to the length of the vessel and v to the speed respectively, while the parameter g is the gravitational constant and ν is used for the kinematic viscosity. Opposite to this, the Reynolds number for propeller flows is typically defined by

$$R_e = \frac{v_{eff} \cdot c(r/R = 0.7)}{\nu} \quad \text{with} \quad v_{eff} = \sqrt{v_A^2 + (0.7\pi n D)^2}\,. \tag{2.14}$$

Here, c refers to the chord length, which is usually defined at 70% of the propeller radius.

To fulfil the similarity of Froude, the velocity of the ship has to be scaled with $v_S = \sqrt{\lambda} \cdot v_M$, while the velocity has to be scaled with $v_S = \frac{1}{\lambda} \cdot v_M$ to achieve similar Reynolds numbers for the ship and the model respectively. Hence, both laws can not be fulfilled simultaneously. In the common model-test procedure Froude's similarity is used to generate an equivalent wave system in model and full scale. It is assumed that the effect of the different Reynolds numbers mainly affects the frictional resistance, which is scaled according to the ITTC 1957 model-ship correlation line. For the investigation of deeply submerged propellers in open water condition, Froude's law is in principle not relevant, as the propeller does not generate any waves. Thus, it would be possible to fulfil Reynolds law, but the models are mostly scaled according to Froude's law. Referring to Krüger [52], this results in more convenient ranges for the numbers of revolution from a technical point of view. As the flow around propellers is dominated by the lift, the error introduced by neglecting Reynolds' law is small. To determine the respective open water values for the full-scale propeller afterwards, the results have to be corrected with respect to friction effects. Therefore, the kinematic similarity

$$\frac{v_{AM}}{n_M \cdot D_M} = \frac{v_{AS}}{n_S \cdot D_S} \tag{2.15}$$

has to be fulfilled. Common procedures for the correction of the open water values are for example described in Müller [61]. Most of these methods only cover the effect of the Reynolds number on the frictional resistance and they are mostly based on empirical correlations. Additionally, some methods do not cover the whole geometry of the propeller. In these cases, the methods are based on Lerbs' [54] approach, where only one representative profile of a propeller blade is considered. Recently, due to the increasing capabilities of numerical methods, it becomes feasible to investigate the full-scale propeller directly or to determine possible scale effects with viscous flow methods as shown in Müller [61]. A possibility to scale the wake field is described in Abels [5], which is also used by the Hamburg Ship Model Basin. The presented approach is based on the Yazaki method for scaling the wake fraction

$$\frac{1 - w_S}{1 - w_M} = f(w_M, L_{pp}, B, T). \tag{2.16}$$

Methods to scale the propulsion and interaction parameters (w,t, $\frac{Q_0}{Q}$) are for example given in Minsaas [59]. He finds the influence of the scale to be important for the effects in the wake and gives simplified relations to scale the wake number, while he does not find scale effects on the thrust deduction fraction and the relative rotative efficiency. He also describes the effect of turbulence. In model scale the flow can be laminar or turbulent, whereas the flow is always fully turbulent in full-scale. Further, different flow conditions are possible in model scale between the open water test and the propulsion test. While the flow is laminar during the open water test, the flow might be turbulent in the propeller plane, if the propeller operates in the wake of the model. To achieve a turbulent flow

also during the open water test, he suggest $R_e = 3 \cdot 10^5$ as lower limit for the Reynolds number.

All the methods for scaling the open water values or the propulsion parameters are derived for deeply submerged propellers. Due to limiting investigations and the complex flow details, scaling methods are not available for partly submerged or ventilating propellers up until now. Furthermore, full-scale measurements do not exist. Thus, possible scale effects become important to predict the risk of ventilation in full scale. Opposite to pure open water tests, the similarity of the Froude number is important, if the propeller operates in the vicinity of the free surface. In this context the Froude number is commonly defined with the draft of the propeller shaft (H):

$$F_n = \frac{\pi n D}{\sqrt{gH}} \,. \tag{2.17}$$

Analogues to deeply submerged propellers, the discrepancy in the Reynolds number should be kept minimal, otherwise laminar or transition effects can become important in model scale. Minsaas [59] finds a minimum Reynolds number of $Re = 3 \cdot 10^5$ also valid for partly submerged propellers. Above this value, he expects the influence of the Reynolds number to be negligible for ventilation investigations. For typical model test propellers with a diameter of $D = 0.2m$, this results in propeller revolutions of approximately $n = 18\,1/s$. Analogues findings can be found in Shiba [76]. In his experiments he only observes scale effects, for example on the thrust coefficient at small Reynolds numbers and laminar flows. For turbulent flows, he finds the effect of the Reynolds number to be negligible. However, the assumptions on the influence of the Reynolds number are reviewed in chapter 5 by using numerical simulations. Finally, for small model test propellers the surface tension of water can become important. To consider this, the Weber number is defined as follows:

$$W_e = nD\sqrt{\frac{\rho D}{S}} \,. \tag{2.18}$$

Here, S refers to the surface tension of water. Shiba [76] found in his experiments a critical Weber number value of 180. Above this value he found that effects of surface tension can be neglected. Of course, for full-scale propellers this is not critical, but for small model test propellers the number of revolutions and the diameter should be large enough to achieve this value. Analogues to the investigation of cavitation, a ventilation number can also be defined as:

$$\sigma = \frac{p_{at} + \rho g h - p}{1/2 \rho v_{eff}^2} \,. \tag{2.19}$$

In this equation p_{at} is the atmospheric pressure. The analogous parameter used to define the cavitation number is the vapour pressure. The ventilation number should be equal for model and full-scale, which is fulfilled in a natural way, if Froude's law and the kinematic similarity are satisfied.

3 Computational models for ship propulsion in waves

This chapter gives a brief overview on existing methods for simulating the propulsion behaviour of ships. The first subsections are dedicated to methods used to predict the flow around propellers. Here, the description starts with an overview on simplified propeller models and continues with calculation models for geometrically resolved propellers. The aim of these sections is to analyse the suitability of such methods for the development of a coupling procedure between a viscous- and an inviscid-flow method, designed for the simulation of unsteady ship-propulsion aspects. An overview of already existing coupling methods to simulate the propeller flow is then presented. The major aim of these coupling methods is to combine the advantages of inviscid- and viscous-flow simulation approaches to reduce the computational times compared to viscous-flow simulations with a geometrically modelled propeller. The later subsections of this chapter are devoted to procedures simulating the sea keeping abilities of floating vessels. Here, methods based on potential-flow as well as viscous-flow methods are described and analysed on their suitability for the investigation of self-propelled ships with possible propeller ventilation.

This chapter is finalized by a description of the computational methods used in this thesis. Therein, some details on the potential-flow method *panMARE*, as well as on the viscous-flow solver *FreSCo*$^+$ are given. Both methods are used in chapter 4 to develop a coupling procedure. In the explanation of the viscous-flow solver special attention is given to a description of the simulation techniques used in the remainder of this thesis.

3.1 Simulation of the propeller performance

A large number of different simulation approaches to determine the propeller performance can be found in the literature. An intensive survey on the different categories of methods is given in Bertram [8]. In the most simple approaches the exact geometry of the blades is not considered, but their influence on the flow. These methods can therefore only be used for rough estimates and certain specific questions. For a more detailed analysis of

the flow conditions at the blades, the exact geometry has to be modelled. This group of methods is presented afterwards.

3.1.1 Simplified models for simulating the propeller flow

The most simple approach for analysing the propeller performance is the so called momentum theory, where only the momentum of a propeller (i.e. the acceleration of water in the propeller disc) and the resulting pressure difference is modelled. This determines the efficiency of the propeller in a simplified manner. Therefore, the propeller is substituted by a simple disc, which equals the assumption of an infinite number of blades. The influence of the propeller is then modelled by the change of the pressure and in turn by the axial velocity inside this disc. The most important parameter, which can be obtained from the momentum theory, is the ideal efficiency

$$\eta_{IA} = \frac{2}{1+\sqrt{1+c_{TH}}}, \quad \text{with} \quad c_{TH} = \frac{T}{\rho/2{v_A}^2 A_0}\,. \tag{3.1}$$

This parameter later on serves as an upper limit for the efficiency of the real propeller design. In eq. 3.1 c_{TH} refers to the thrust loading coefficient, which is defined by the ratio between the generated thrust and the hydrodynamic pressure multiplied with the area of the propeller disc (A_0). Of course, this approach is not suitable to design the geometry of the propeller. But this approach is often used in RANS methods to model the impact of the propeller with a set of equivalent body forces. These so-called actuator disc methods are also the initial stage for the development of coupling procedures and are therefore described in more detail in section 3.2.2.

The next step towards the exact modelling of the flow around propellers is to use methods based on the lifting line theory. Such methods are based on the assumption that every cylindrical cross section of the propeller blade acts as a lift producing foil. The lift is generated by a set of vortices located typically on a straight or curved line, connecting the points at 25% chord length from the root of a propeller blade to the tip. Thus, only the effect of a profile and not the exact geometry is modelled. According to Helmholtz' law, the strength of a vortex is constant over the length of the vortex. Hence, the change in the strength of the vortices over the span of the blade results in a set of trailing vortices, with the resulting lift vector being oriented orthogonal to the local inflow velocity. In these approaches the three-dimensional effect generated by a possible rake or skew of the blade is not considered and the blade thickness is neglected. Another drawback of lifting-line methods is the inability to model the propeller hub as stated by Bertram in [8]. Hence, the ability of such approaches to simulate unsteady flow-effects around propellers is limited.

To increase the accuracy of the computational method, lifting-surface methods can be used instead of lifting lines. The most common numerical approaches based on lifting surfaces are called vortex-lattice methods (VLM), where the blade is modelled by a grid of vortices. Additionally, the wake of the single blades is modelled with a system of vortices. In many cases, the geometry of these wake surfaces is kept constant during the simulation and the pitch of the wake system is computed in a simplified manner. This makes the respective methods inaccurate for non-uniform inflow conditions towards the propeller. Vortex-lattice methods are able to handle arbitrary blade geometries, but they do not consider the blade thickness. Additionally, the propeller hub is not simulated, which produces inaccurate results in the vicinity of the hub. To overcome the problem of the missing blade thickness, vortex-lattice methods can be supplemented with a source/sink distribution based on the thin-wing theory. Then, also a simplified simulation of sheet cavitation is possible. Both, the sources and the vortices are typically placed on the mean chord surface of the blade. Applying the kinematic boundary condition on the blades, the pressure distribution is computed by using the Bernoulli equation. Finally, thrust and torque of the propeller can be calculated from the pressure distribution. More details of the computational approach inside vortex-lattice methods are described in Bertram [8], while the application of such a method is for example demonstrated in Abels [5]. Therein, the author uses the method QCM (Quasi-Continues Method), which is a variant of a VLM to simulate the propeller in a previously determined wake field. Aim of his study is to investigate the pressure pulses on the aft ship, generated by the propeller.

3.1.2 Geometrically resolved propellers

In the group of geometrically resolving propeller flow methods, the main methods used, are boundary-element methods (BEM) considering only the inviscid flow and RANS based finite-volume methods.

In boundary-element methods, the propeller blades as well as all other geometrical boundaries are covered with panels. Compared to lifting-surface methods, the correct blade geometry including the thickness is modelled and the pressure distribution on the pressure and suction side can be computed. The flow around the propeller is simulated by applying the kinematic boundary condition (no flow through the panels). Analogues to lifting-surface methods, the pressure on the blades is derived from the Bernoulli equation. Again, a second group of panels is used to model the wake surfaces behind the blades to fulfil the Kutta condition. Opposite to lifting-surface methods, the deformation of these surfaces is mostly computed according to the local flow characteristics. A serious task in boundary-element methods is the implementation of the Kutta condition. With the help of this condition, which suppresses the flow around the trailing edge, the lift of the profiles is generated.

Boundary-element methods are used for the simulation of propeller flows since the 1980's due to the increase of computational power. A short historical overview is given by Hess [37], who himself is one of the first developers of boundary-element methods. In the article a short summary of the different possibilities for applying the Kutta condition is given, where he suggests a formulation based on equal pressure values on both sides of the trailing edge. Differences in the available BEM approaches can also be found in terms of the unknown variable. Here, Morinos approach [60] becomes very popular, where directly the velocity potential is computed and the velocities are determined by differentiation. Today, boundary-element methods can be used for a large number of propeller flow simulations including cavitating and ventilating propellers as shown for example in Kinnas and Young [41]. Furthermore, it is also possible to investigate surface-piercing propellers and therefore to include the free surface covered with panels into the simulation. One example of such a simulation is presented by Young and Kinnas as well [92]. In this example the BEM, which is used to simulate the propeller, the shape of the cavity and the free surface is coupled with a finite-element method. This investigates the deformations and vibrations of a surface-piercing propeller blade. But, the simulation of a propeller in the wake of a ship is not possible with boundary-element methods due to the negligence of viscosity in potential-flow theory. Hence, the impact of the propeller on the ship and therefore the propulsion efficiency including all interaction effects can only be investigated with viscous-flow methods.

In general, viscous-flow methods are able to compute all interaction effects between ship and propeller. However, the computational effort is sufficiently larger than for potential-flow methods, which strongly restricts the application of these methods for the analysis of ship-propulsion in practice. One of the first examples for viscous propeller-flow simulations can be found in Stern [81], where the author computes the flow around a simplified propeller geometry with rectangular blades and infinite pitch in open water conditions. To reduce the computational effort, he further uses a moving frame of reference approach in combination with periodic boundary conditions to restrict the computational domain to a single blade. This insists that the simulation becomes steady. Laminar and turbulent calculations using the $k-\epsilon$ turbulence model are then performed to study the flow in the blade region. As the results of Stern were very promising, various other authors started to use viscous-flow methods in the 1990's to study the propeller flow (see Abdel-Maksoud et.al. [2] for example). In the following years, the increasing capability of computational power allowed for more and more simulations with real propeller geometries. For simulations in uniform inflow conditions the moving frame of reference approach is still used to limit the computational times. Examples for this practice can be found in Maksoud et.al. [4] or Berchiche and Janson [7], where local flow details such as the pressure reduction in the tip vortex as well as the computed open water values are compared to experimental results. The effort for this kind of calculations is relatively small, but the uniform inflow condition is only sufficient for an open water analysis in undisturbed

inflow conditions. In the case of non-uniform inflow, the computational effort increases significantly. Then, all blades have to be modelled, the simulation becomes unsteady and the domain moves with the propeller. This approach is used later on in chapter 5 to calculate the free surface influence on the propeller. Furthermore, the complexity in grid generation increases as pointed out by Maksoud et.al. [3]. He describes the high demands on the grid generation due to the complex shape with large skew angles of modern propeller blades, especially if all blades of the propeller have to be modelled. The effort for the grid generation further increases, when it has to be performed in the restricted space in the aft-ship region.

Additional to this, the complexity of the numerical approaches increases significantly if the propeller is operating behind a ship. Multiple domain approaches like sliding interfaces or overlapping grids are then necessary to model the different parts of the computational domain and the relative motions of ship and propeller. Exemplary applications can be found in Bugalski [10] and Muscari [63], where the sliding-interface as well as the overlappping-grid technique are used to model the rotating propeller behind a hull.

Moreover, both grids can be moved together to simulate the movements of a manoeuvring vessel in waves. In this case, another problem occurs in conjunction with the different time scales between the rate of rotation of the propeller and the typical periods of ship motions in waves. This can be illustrated by a simple numerical example, which clearly indicates the importance of efficient computational methods to investigate ship propulsion in waves: A typical roll period of a ship is in the magnitude of 15s. Hence, far more than a hundred seconds have to be simulated to investigate the motion behaviour. On the other hand, a propeller rotates typically with a frequency in the magnitude of 0.5s and a common time-step size in RANS computations to resolve the propeller rotation is in the magnitude of 2°-4° per time step. With these parameters a minimum of 800 time steps are necessary to simulate one period of the roll motion. This problem is discussed in Carrica [15] and Simonsen [77]. Due to these problems only very few examples of RANS investigations of ship-propeller interaction can be found in the literature. An overview of some examples is given in the following.

3.2 Methods for the simulation of ship-propeller configurations

3.2.1 Geometrically modelled propeller

One of the first authors who carried out simulations of a rotating propeller in a ship's wake are Kim et.al. [40] in 2002. Within these simulations, the overlapping-grid technique is

used to perform a study on the flow details in the aft-ship region. Later on, Pankajakshan [66] performs self-propelled manoeuvring simulations using the sliding-interface technique. As the investigated vessel is a submarine, free surface effects are not considered.

During the last few years, the number of authors investigating a rotating propeller behind a ship increased due to the growing computational power. Especially the group of Carrica ([15] and [17]) performs extensive simulations of self-propelled ships. In the first paper the typical experimental procedure of resistance, open water and self-propulsion test is performed numerically for different types of ships. The second paper consists of manoeuvring simulations and therefore computations of the propeller in off-design conditions. In both cases the RANS solver CFDShip-Iowa (Paterson [67]) including a level-set approach for simulating the free surface and the overlapping-grid technique are used. Analogues to the typical model-test procedure, they control the number of revolutions to obtain a target speed. Afterwards, they analyse the propulsional parameters as well as the interaction of the vortical structures generated by the propeller, with the rudder. The predicted results are in line with experimental results, but the large computational grids (typically 5-20 million cells) and the immense simulation times restrict the application to very few simulations.

Further investigations were performed during the last Gothenborg-CFD workshop [1], where self-propelled computations for the Kriso container ship (KCS) are one of the defined test cases. At this workshop, the most detailed study was performed by the group of Carrica, where the ship-propeller configuration was investigated in full-scale [18] and with free trim and sinkage [16]. More results for different available commercial RANS solvers can be found, where the sliding-grid technique is used to simulate the relative motions of ship and propeller (Greve [33], Bugalski [9], Lee [53]).

In all these simulations firstly, the time-step size has to be estimated according to the rate of rotation of the propeller, which results in very small time steps and very large computational times. Secondly, a large number of cells is necessary to resolve the geometry of the different bodies. Especially the propeller and other small appendages create high demands on the grid resolution. To overcome these difficulties many authors use coupled approaches instead of a geometrically modelled propeller. An overview of the fundamentals of these procedures is given in the following.

3.2.2 Coupling strategies

As indicated in the previous subsection, a geometrically resolved propeller requires a large computational effort in RANS computations, especially if the propeller is simulated behind a ship. To reduce the computational times, the propeller can be substituted by a set of equivalent forces. In most of the coupling approaches these forces are obtained from a

potential-flow solver. The aim of this technique is to combine the benefits of the two baseline methods, i.e. the small computational times of inviscid-flow methods and the accuracy of viscous-flow methods in predicting the effects in a ships wake. The basics of this procedure are derived from the momentum theory (see section 3.1.1), where the propeller is only modelled by the change of the velocity and the pressure in the propeller position. Inside the viscous-flow solver, this impact is generated by a distribution of discrete forces, which are added as volumetric body-forces to the momentum equation as shown in the following formula:

$$\frac{\partial}{\partial t}\int_V \rho \mathbf{v} dV + \int_S \rho \mathbf{v}\mathbf{v}\cdot\mathbf{n} dS = \int_S \mathbf{T}\cdot\mathbf{n} dS + \int_V \rho \mathbf{b} dV\,. \tag{3.2}$$

In this equation $(\mathbf{v})$ refers to the velocity vector , while p denotes again to the pressure, t is used for the time and T is the stress tensor. Integrals are defined over the cell volume (V) or the cell surface (S) with n being the vector normal to the surface. The last term of this equation $(\int_V \rho \mathbf{b} dV)$ contains the above described volumetric body forces representing the propeller as well as any other external forces. In the standard and most simple variant, the propeller forces are determined from a previously determined open water diagram. The forces are then applied on a so-called actuator disc, which has the same radius as the original propeller and a thickness estimated by the axial distance between the leading and the trailing edge. To distribute the propeller forces to the disc cells at the different radii, a function derived from the typical radial distribution of the circulation is defined, while the forces are averaged in circumferential direction. As a rule, the open water diagrams are provided inside the procedure in a linearised form: $k_t = c_{T_1} - c_{T_2}\cdot J$. This simplification is valid for standard open water diagrams, especially if the linear regression is developed around the typical operating point of the propeller, represented in fig. 3.1.

From this relationship the thrust and torque can be determined in dependency of the advance coefficient and the inflow velocity:

$$\begin{aligned} T &= \rho n^2 D^4 \cdot (c_{T_1} - c_{T_2}\cdot J) = (\frac{c_{T_1}}{J^2} + \frac{c_{T_2}}{J})\rho D^2 v_A^2\,, \\ Q &= \rho n^2 D^5 \cdot (c_{Q_1} - c_{Q_2}\cdot J) = (\frac{c_{Q_1}}{J^2} + \frac{c_{Q_2}}{J})\rho D^3 v_A^2\,. \end{aligned} \tag{3.3}$$

The propeller forces have to be determined in an iterative procedure, as neither the inflow velocity nor the number of revolutions are known for the propeller in the specific flow condition. Therefore, two different possibilities exist, which deviate in the constant and dependent variables:

- The number of revolutions is set at a constant. The inflow velocity is determined from the momentum theory as illustrated in fig. 3.2, where the thrust is calculated from the mass flux through the propeller plane (A_P) and the difference of the

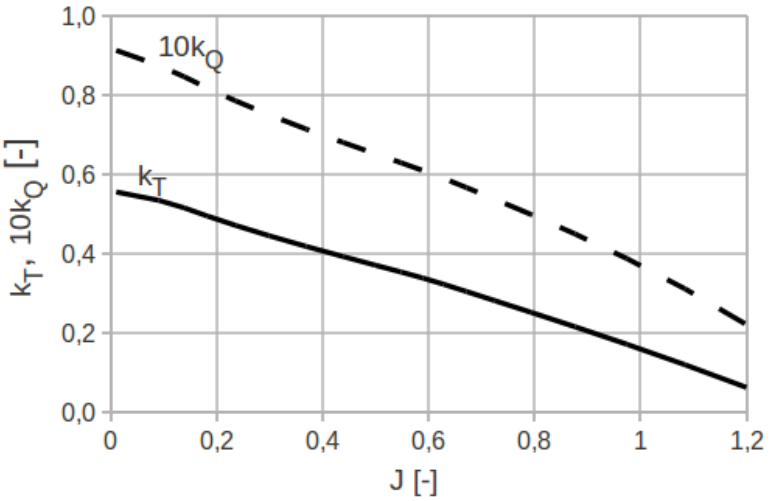

Figure 3.1: Typical open water diagram with an almost linear dependency of the thrust and torque coefficients from the advance ratio.

velocities in front of and behind the propeller plane:

$$T = \rho v_P A_P (v_B - v_A) = 2\rho v_P A_P (v_P - v_A) \quad \text{with} \quad v_P = \frac{1}{2}(v_B + v_A)\,. \tag{3.4}$$

Within this equation v_A denotes to the velocity in front of the propeller plane, while v_B refers to the velocity far behind the propeller. As shown in fig. 3.2, the index P is used for variables directly in the propeller plane. Combining eq. 3.3 and eq. 3.4, the unknown inflow velocity can be determined iteratively.

- The number of revolutions of the propeller is varied until the self-propulsion point of the ship is reached. This procedure is similar to a propulsion test, where also the number of revolutions is iterated until an equilibrium between the propeller thrust and the ship resistance together with the thrust deduction fraction is found.

This approach is commonly called body-force or actuator-disc model and it is implemented in many RANS solvers. More details about this procedure can be derived from Manzke [56] and Xing [90].

As the propeller forces are determined beforehand and for a propeller in uniform flow, the ship's influence on the propeller flow is not considered in simple actuator-disc methods. To overcome this inaccuracy, an additional numerical method can be used to determine the propeller forces. The basic idea of this kind of approaches is to use a two-way coupling of a potential-flow and a viscous flow method (i.e. a RANS method). Therein, the RANS

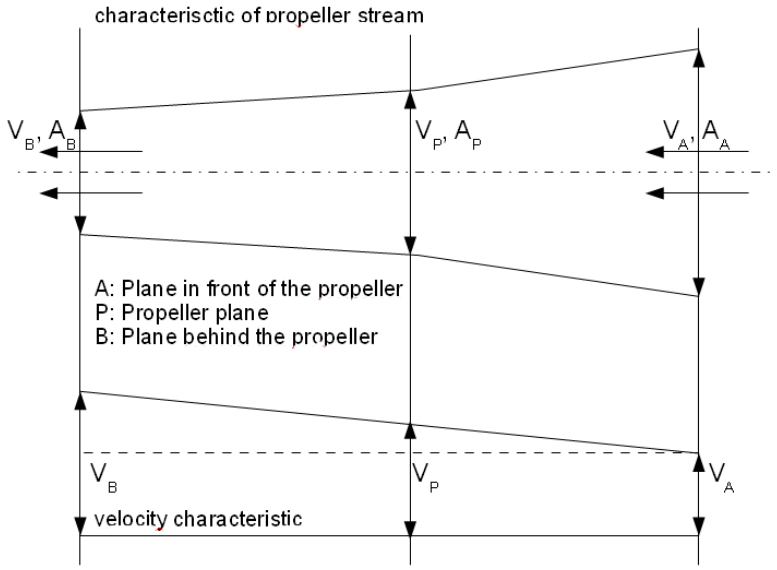

Figure 3.2: Illustration of the momentum theory displaying the characteristics of the propeller stream.

method is used to simulate the flow around the ship and therefore, to predict the inflow velocities towards the propeller. As the inflow towards the propeller contains the total wake, including the propeller's own influence, the propeller induced velocities have to be determined by the inviscid-flow method to subtract them from the total flow. As the effective wake remains, it can be used as inflow condition for the inviscid simulation of the flow to determine the propeller forces. These forces are transferred back to the viscous-flow solver, where they are applied inside the propeller disc to account for the propeller influence.

The origin of these coupling and actuator disc approaches dates back to the 1970's, where first Sparenberg [79], [80] and then Schetz and Favin [74], [75] simulated the impact of a propeller by applying forces to an actuator disc. Sparenberg starts with an analytic method for inviscid fluids and later on, he analyses how the efficiency of an actuator-disc propeller changes in viscous flow. In the approach of Schetz, the forces are afterwards applied in a viscous-flow method. Within this, the Navier-Stokes equations are solved numerically including turbulence effects. In all these methods the forces inside the disc as well as the floating body are considered to be axisymmetric. Additionally, in the theory of Sparenberg the influence of the propeller is considered only in a linear way by assuming that the propeller induced velocities are small compared to the total velocity along the body.

Later on, Stern [82] uses a vortex-lattice method to simulate the propeller behind a ship. He is one of the first researchers using a coupling approach in a narrower sense, where two numerical methods are combined to investigate ship-propeller interactions. In his approach the ship is simulated in a zonal approach, where viscous effects are considered only in the boundary layer and in the wake, while the outer flow is assumed to be inviscid. The interaction of hull and propeller is considered in an iterative procedure. Hence, the propeller works in the effective wake of the ship. The obtained thrust and torque of the propeller are then distributed within the propeller plane according to a typical radial distribution of the circulation. A variation of the forces in circular direction is not considered in this approach, which reduces the approaching flow towards the propeller to an axisymmetrical flow. This method is used to simulate stationary interaction effects for simplified ship geometries and it shows good results in determining for example the thrust deduction fraction.

Considering a typical wake field (c.f. fig. 2.1), it is obvious that the flow towards the propeller is not axisymmetrical. Hence, in the 1990's various authors started to develop coupling approaches, which consider also the circumferential variation of the thrust. In the method of Zawadzki et.al. [93] an unsteady version of a BEM method is used to determine the propeller forces on each panel for different circumferential positions. For each panel and circumferential position a time averaged force value is obtained. This force is then transferred to the RANS solver, where it is applied to the cells at the corresponding circumferential and radial position. The RANS simulation itself is steady and therefore, the actual blade positions are not relevant. An analogues approach is used in Hally et. al. [35]. Here, the authors also use circumferential and radial varied force data in a steady RANS simulation to cover the interaction between ship and propeller. They validate the method by comparing the propeller induced velocities computed by the BEM, with the induced velocities obtained from the RANS solver for open water simulations. During this comparison, they find a relatively good agreement between the different methods. They conclude that the remaining discrepancies are due to the flow inside the blade in the BEM. If this flow is corrected by enforcing the mass conservation across the blade surface, a better agreement between the induced velocities is achieved. In the approach of Chao [19] a very similar method is used to transfer the propeller forces from the potential flow solver to the RANS solver. This approach also considers a circumferential and radial varying force distribution in a steady RANS simulation. Opposite to the procedures described beforehand, the author uses a variant of a vortex-lattice method (QCM) instead of a BEM to compute the propeller forces. The described method is then used to investigate the influence of rudder and propeller positions on the propulsion characteristics.

Except for Chao's investigations, only simplified geometries in steady flow are considered in the examples described beforehand. Recently, coupling approaches are more frequently used for the simulation of realistic applications with complex geometries or for investigations of the manoeuvring capabilities. For example Philips et.al. [69] uses a coupling of

a RANS solver and a method based on blade-element theory to compute manoeuvring derivatives. Another possibility is to use coupling approaches to investigate the efficiency of propulsion improvement devices like ducts as shown in Hafermann [34]. In this publication, the author uses a coupling of a vortex-lattice method and a RANS method to simulate a self-propelled ship with different configurations of appendages. This determines the required shaft power and the effective wake fields. Furthermore, Han [36] uses a coupling method to optimize hull/propeller/rudder configurations. In her approach, the flow around the ship is computed with a zonal approach, where the RANS equations are solved only in the aft ship region. Around the fore body the fluid is considered to be inviscid except for a thin boundary layer. For the simulation of the propeller a vortex-lattice method and a method based on lifting lines are used. The presented approach is validated with open water calculations for a series of Wageningen B4-70 propellers, where good results with a maximal deviation of 8% compared to the experimental values are obtained. Finally, the author uses the coupling for the analysis of self-propelled ships. This coupling includes the rudder and achieves promising results with an accuracy within 5% for the global quantities (i.e. resistance, thrust). Even though the exact propeller geometry is not considered in the coupling procedures, sufficient results are obtained in most of cases. Furthermore the computational effort is significantly smaller than for a geometrically resolved propeller as shown by Müller et. al. in [62]. Here, the authors compute a twin-screw ship with an operating propeller. In one simulation the propeller is geometrically modelled, while in the second simulation the propeller is modelled on the basis of a mathematical model for the different blade sections. Using the propeller model, the computational times are reduced by a factor of eleven, by achieving a good accuracy in the predicted results.

3.3 Methods for sea-keeping simulations

In the following subsections, available methods for sea keeping simulations are briefly described. The main focus of this section is to analyse what kind of methods can be used for the simulation of ship propulsion in waves, including a possible ventilating propeller.

3.3.1 Methods based on potential theory

Most commonly, methods based on potential-flow theory are used to predict the sea keeping behaviour of a vessel. According to Söding [78], viscous effects are less important in sea-keeping applications due to the instationarity of the flow. Hence, the accuracy of potential-flow methods is sufficient for most applications. Compared to viscous-flow methods the computational times are much smaller due to the simplified flow equations.

Instead of solving the Navier-Stokes equations, only one equation (the Laplace equation) has to be solved. Secondly, potential-flow methods are mostly boundary-element methods. Hence, only the body surface and the free surface have to be covered by panels. The first methods developed for the prediction of the sea-keeping abilities are strip-methods, which are suitable for slender-bodies. Here, only the flow in two-dimensional cross sections (stripes) is considered. Furthermore, most of these methods are linear by assuming the movements of the floating body to be proportional to the wave amplitude, which allows a solution in the frequency domain. A description of the basics of strip theories can be found for example in Bertram [8]. Additionally, the influence of natural seaways can be considered by a superposition of the results for regular waves with different wave parameters. A solution in the time domain becomes necessary, if a non-linear dependency of the ship motions on the wave amplitude is regarded. Examples for non-linear strip methods can be found in Pereira [68] and Kröger [51].

The second class of methods are panel or boundary-element methods. Here, the flow is considered to be three-dimensional, which makes the methods suitable for arbitrary marine structures. Depending on the used approach for the elementary solutions (sources), mainly two sub-classes of methods exist (see again Bertram [8]):

- Methods based on Green functions: Here, the boundary condition on the free surface is fulfilled implicitly by the formulation of the source terms and therefore only the hull boundary has to be discretized. Hence, the number of unknowns is relatively small, but the formulation of the elementary solution for ships with forward speed is difficult as indicated by Söding [78].
- Rankine-source methods: In these methods the body surface as well as the free surface is covered by panels. Thus, the resulting equation systems are larger than in Green-function methods, but the drawback for $v \neq 0$ vanishes.

The simulation of the ventilating propeller requires an accurate prediction of the flow in the aft-ship region, where viscous effects become important. Also, the modelling of a ruptured free surface due to ventilation is difficult to handle in boundary-element methods. Thus, methods based on potential theory are not suitable for the scope of this thesis.

3.3.2 Viscous-flow methods for sea-keeping applications

The increasing computer performance over the last few years facilitates the use of viscous-flow methods for sea-keeping applications. However, the computational effort is still very high, which limits the application of viscous-flow methods to only a few seconds of simulation time, while the study of long term (statistical) ship responses to natural seaway is still far beyond the feasibility of RANS methods. Here, potential-flow methods as described in the previous subsection have proven to be effective and are therefore

the most common practice. On the contrary, viscous-flow methods are an attractive possibility for the simulation of single and short term scenarios, where viscous effects are crucial for the determination of extreme wave loads. This includes the computation of slamming loads, the simulation of green-water events or the computation of wave loads on offshore structures amongst others. For applications like this, sometimes a combination of RANS and potential flow methods is used as described by Shellin et. al. in [73]. Here, the authors use potential-flow methods to determine critical situations and these wave scenarios are then simulated with a RANS method to compute slamming loads. The large computational times for these applications mainly result from the required amount of cells to accurately compute the propagating waves towards the floating body without an inadequate wave damping. Due to the Courant number

$$Co = \frac{v\Delta t}{\Delta x}\,, \tag{3.5}$$

the requirements on the cell size, specified by Δx strongly restrict the possible time-step size (Δt). In section 3.4.2, the importance of the Courant number is outlined in more detail.

Next to the large computational times, another problem occurs in conjunction with the modelling of the outlet boundary to suppress wave reflections. The most common approaches to overcome this difficulty are numerical-beach methods, which are applied mainly in two variants. The first possibility is used for example by Xing [90], where the grid is stretched in front of the outlet boundary to damp the waves by an increasing amount of numerical diffusion. Secondly, wave damping can be achieved by modifying the atmospheric pressure in a certain distance in front of the outlet boundary as proposed in Kleefsman [42] or Clement [22]. The drawback of both approaches is the extended length of the computational domain, resulting in an increased amount of cells and, in consequence, computational time. To reduce the dimensions of the computational domain, various authors recommend the use of non-reflecting boundary conditions (NRBC), based on the Sommerfeld condition:

$$\frac{\partial \phi}{\partial t} + c\frac{\partial \phi}{\partial x} = 0\,. \tag{3.6}$$

In this equation, ϕ is an arbitrary transport variable travelling with the waves, for example a velocity component and c is the wave celerity. The problem that occurs within these approaches is determining the celerity at the outlet boundary. For an undisturbed wave, one can use the wave celerity of the incoming wave but for diffracted waves the wave celerity is unknown. In case of an inappropriate choice for the velocity, wave reflections can occur at the boundaries. To overcome this, Wellens et.al. [87] suggest to use an approximated version of the dispersion relation to compute the wave celerity of the approaching wave, while Givoli et.al. in [32] recommend using higher order approaches, which allow arbitrary values for c.

Another possibility to model the boundary conditions in sea keeping applications are coupling approaches. In this group of methods the RANS equations are only solved in an inner domain, while simpler approaches like potential-flow theory are applied in the outer part of the domain. One example for this is the SWENSE approach (Spectral Wave Explicit Navier Stokes Equation), developed by Gentaz et.al.[31]. The authors use a modified version of the Navier-Stokes equations by splitting the unknowns in an inviscid part, which automatically fulfils the transport equations and a supplement containing the influence of wave diffraction. In the far-field, the diffracted part vanishes and the wave field is equivalent to the propagating waves. Keeping in mind, that no floating body is considered in the inviscid solution. Two other possibilities are described in Kleefsman [42] and Yeung et. al.[91], where a spatial decomposition of the domain is used. In chapter 6 an approach developed for *FreSCo*$^+$ is described, that shows some similarities to the SWENSE approach. In both methods uniform boundaries are applied on all sides of the computational domain, which results in an increased flexibility compared to NRBC methods and the simulation of different wave directions becomes possible within one computation.

In addition to the modelling of the boundary conditions, the motions of the ships have to be simulated in sea keeping simulations. This is commonly done by coupling the equations of motion with the RANS equations. Applications of this method can be found widely in the literature, the approach itself is described in more detail for example by Xing [90].

3.4 Description of the employed viscous-flow solver

The viscous-flow method used in this thesis is the in-house code *FreSCo*$^+$, which uses a finite-volume approach to solve the RANS equations. *FreSCo*$^+$ is a joint development of Hamburg University of Technology (TUHH) and the Hamburg Ship Model Basin (HSVA). In the next subsection a brief description on the fundamentals of the method is presented, while the following two subsections are devoted to a description of the numerics, which are especially relevant for the applications in this thesis. More details about *FreSCo*$^+$ can be found in Rung et. al.[72], while the numerical procedure is described in Ferziger and Peric [29].

3.4.1 General description

The governing flow equations, which are solved numerically in *FreSCo*$^+$ with the help of a finite-volume method, are the conservation of mass:

$$\frac{\partial}{\partial t}\int_V \rho dV + \int_S \rho \mathbf{v}\cdot\mathbf{n} dS = 0\ , \tag{3.7}$$

and the conservation of momentum:

$$\frac{\partial}{\partial t}\int_V \rho \mathbf{v} dV + \int_S \rho \mathbf{v}\mathbf{v}\cdot\mathbf{n} dS = \int_S \mathbf{T}\cdot\mathbf{n} dS + \int_V \rho \mathbf{b} dV \ . \tag{3.8}$$

In these equations V denotes to the volume of a cell, while S is the surface area with $\mathbf{n}$ being the surface normal. The variable t is used for the time, $\mathbf{v}$ denotes to the velocity in a cell and ρ is the fluid density. External forces like the gravitation are considered in the second term on the right hand side. The variable $\mathbf{T}$ denotes to the stress tensor with:

$$T_{ij} = -p\delta_{ij} + \mu\left(\frac{\partial u_i}{\partial x_j} + \frac{\partial u_j}{\partial x_i}\right) \ , \tag{3.9}$$

being the components of the tensor. Here, p refers to the pressure, μ is the dynamic viscosity and δ_{ij} is the Kronecker delta.

For typical Reynolds numbers in marine applications ($R_e > 10^6$) a direct numerical solution of these equations is not possible. Due to the very small turbulent vortex structures, the necessary amount of cells in the boundary layer and the resulting limitations on the time step, the computational effort is far beyond an acceptable range for practical applications. To overcome this problem, mainly two groups of methods exist. In LES (large eddy simulations) or DES (detached eddy simulations) approaches only the larger vortical structures are resolved, while a turbulence model is used to model the influence of the smaller vortical structures. In the second group of methods, a turbulence model is used to capture all the turbulent effects. To derive such a model Reynolds decomposition of variables is used, which splits the unknowns in eq. 3.8 and 3.7 in an averaged value and a fluctuating one, viz.

$$\phi(\mathbf{x},t) = \bar{\phi}(\mathbf{x},t) + \phi'(\mathbf{x},t) \ . \tag{3.10}$$

The resulting equations have the same form as the Navier-Stokes equations. Though, an extra term with additional unknown variables appears in the convective term in the momentum equations, because of the non-linearity of this term. Hence, the number of unknowns exceeds the number of equations. Using the Boussinesq method, the extra term can be replaced by a term analogues to eq. 3.9, which results in a larger and non-constant effective viscosity ($\mu_{eff} = \mu + \mu_T$) and a term containing the turbulent kinetic energy (k). The variable μ_T is used for the turbulent viscosity, which is variable during a simulation. For the modelling of these two extra variables various turbulence models exist. The most common models are the so-called two-equation models, where two additional transport equations are solved. For the simulations in this thesis, the k-ω turbulence model, proposed by Wilcox [88] is used. Within this, one equation is solved for the turbulent kinetic energy(k) and one for the dissipation rate (ω).

To apply the system of equations on each control volume of the computational grid, the integrals have to be approximated. For integrals over the volume of a cell, the conventional

mid-point rule is used. The approximation of the integrals over the cell surface requires variable values in the centre of the cell surfaces. As the variables for all transport equations are stored in the centres of the control volumes, the values at the faces have to be interpolated from the cell centres. In the present thesis mostly flux-blending schemes are used, but a large number of other techniques proposed in literature are available as well. The integral approximations are formulated in an unstructured manner in *FreSCo*$^+$, which allows the use of arbitrary-shaped cells. In the cases presented in this thesis, unstructured hexaeder grids with local refinements are used.

The governing equations have to be solved in a segregated and iterative solution procedure, because of the non-linearity of the momentum equations and the coupling of the momentum equation with the mass conservation equation. For this coupling a SIMPLE-type pressure correction is used in *FreSCo*$^+$. To avoid a decoupling of eq. 3.7 and 3.8, the method proposed in Rhie and Chow [71] is implemented. For unsteady calculations the implicit Euler scheme or a three-time level scheme is available within *FreSCo*$^+$. Because of the very small time steps in the present simulations, only the implicit Euler scheme is used, which is of first order.

The resulting linear equation systems are solved with iterative solution procedures offered by the PETSc-library. To reduce the simulation times, the algorithm can be parallelised with a domain-decomposition approach. Here, the computational domain is subdivided into a number of subdomains. For the load-balancing between the subdomains, the parMETIS partitioning library is applied. Afterwards the same *FreSCo*$^+$ executable is used on the different domain parts. The inter-processor communication for this single-program, multiple data (SPMD) message-passing model is organised by the MPI library.

3.4.2 Free surface modelling and wave generation

In most of the simulations presented later on, the ship or the propeller operates in the vicinity of the free surface. Hence, the location of the free surface has to be determined during the simulation. Therefore, a volume-of-fluid (VoF) method is applied. In this group of methods, the computational domain contains multiple phases, i.e. the water phase as well as the air phase. The distribution of water ($c = 0$) and air ($c = 1$) in the computational domain is then determined by an additional transport equation for the mixture fraction $c \in [0, 1]$:

$$\int_V \frac{\partial}{\partial t} \rho c dV + \int_S \rho c \mathbf{v} \cdot \mathbf{n} dS = 0 \,. \tag{3.11}$$

Afterwards, the fluid properties are calculated according to the mixture fraction:

$$\begin{aligned} \rho &= \rho_w \cdot c + \rho_a \cdot (1 - c)\,, \\ \mu &= \mu_w \cdot c + \mu_a \cdot (1 - c)\,. \end{aligned} \tag{3.12}$$

Within this, the index a denotes the air phase and the index w refers to the water phase. The interpolation of the face values from the cell centres is more complex than for other properties and requires a special interpolation scheme. The method used in *FreSCo*$^+$, is the downwind biased interpolation scheme HRIC (High Resolution Interface Capturing), proposed by Muzaferija and Peric [64], which predicts the face values of the mixture fraction without significant amounts of numerical diffusion and in a bounded range. The interpolation is sensitive to the dimensionless time step, specified in eq. 3.5 . In the HRIC scheme the respective maximum values are limited to $Co \leq 0.7$, otherwise large amounts of numerical diffusion are introduced. Moreover, the HRIC scheme is supplemented by an additional interface-sharpening approach, which prohibits an unphysical mixture of water and air in a conservative way. The limitations on the time step are necessary for the VoF equation, but not for the other equations. To accelerate the solution process, a subcycling technique is applied, wherein smaller time steps are used for the VoF equation than for the others. Thus, within one time step of the momentum equation, the distribution of c is updated several times. In combination with a variable time-step size, a remarkable speed up of the solution procedure can be achieved as illustrated by Manzke et.al.[57]. The major benefit of VoF-type interface capturing schemes is the larger flexibility compared to interface tracking systems in terms of large deformations of the free surface. As the interface between water and air is not a domain boundary, also ruptured deformations of the interface including breaking waves or splashes, can be simulated.

To account for the seaway, waves have to be generated at the inflow boundaries. Consequently, different wave theories (i.e. Airy, Stokes), external programs or a moving body simulating a wave maker, can be used. For the calculations in this thesis the Airy theory [27] is applied. The Airy theory is based on potential flows, thus no viscous effects are considered. Furthermore, the theory is linear and only valid for waves with a small wave height / wave length ratio. Linearity in this context means that the combined boundary condition (combination of kinematic and dynamic BC) at the free surface is linearised and fulfilled for the still water level. Thus, strong limitations on the wave steepness have to be accepted. On the other hand, a superposition of single wave components is possible, which makes the theory highly flexible. Accordingly, the Airy theory is also often used in potential flow methods to model a natural seaway by a superposition of single Airy waves.

Figure 3.3 illustrates the coordinate system that is used for the definition of the waves. In this example, the waves are travelling in the positive x-direction, while the z-coordinate points upwards. Furthermore, the definition of the wave length (λ) and the wave amplitude

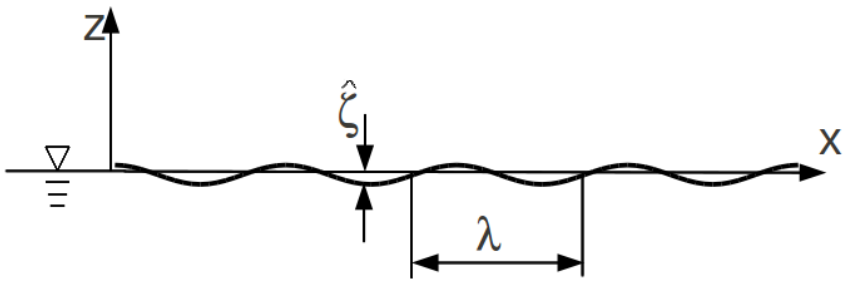

Figure 3.3: Coordinate system used for the description of waves.

($\hat{\zeta}$) are given in this figure. The resulting wave elevation is a harmonic function and depends on the actual location ($\mathbf{x} = (x, y, z)^T$) and the time:

$$z(t) = z_{SW} + \hat{\zeta} cos(\omega t - kxcos\mu - kysin\mu)\,. \tag{3.13}$$

Here, z_{SW} is the still-water height of the free surface and ω denotes to the wave frequency. The angle μ is the encounter angle between the direction of the ship speed and the direction of the travelling waves, which is defined according to figure 3.4.

The Cartesian coordinates of the velocity vector follow from the equations for the orbital velocities:

$$\begin{aligned} v_x &= v_{s_x} + \omega\,\hat{\zeta} e^{-k(|z-z_{SW}|)}\,\cos(\omega t - kx\,\cos\mu - ky\,\sin\mu)\,\cos\mu\,, \\ v_y &= v_{s_y} + \omega\,\hat{\zeta} e^{-k(|z-z_{SW}|)}\,\cos(\omega t - kx\,\cos\mu - ky\,\sin\mu)\,\sin\mu\,, \\ v_z &= -\omega\,\hat{\zeta} e^{-k(|z-z_{SW}|)}\,\sin(\omega t - kx\,\cos\mu - ky\,\sin\mu)\,. \end{aligned} \tag{3.14}$$

For the velocities in air the following relations can be used:

$$\begin{aligned} v_x &= v_{s_x} - \omega\,\hat{\zeta} e^{-k(|z-z_{SW}|)}\,\cos(\omega t - kx\,\cos\mu - ky\,\sin\mu)\,\cos\mu\,, \\ v_y &= v_{s_y} - \omega\,\hat{\zeta} e^{-k(|z-z_{SW}|)}\,\cos(\omega t - kx\,\cos\mu - ky\,\sin\mu)\,\sin\mu\,, \\ v_z &= -\omega\,\hat{\zeta} e^{-k(|z-z_{SW}|)}\,\sin(\omega t - kx\,\cos\mu - ky\,\sin\mu)\,. \end{aligned} \tag{3.15}$$

In these equations $k = \frac{2\pi}{\lambda}$ denotes to the wave number. The quantities v_{s_x} and v_{s_y} represent the Cartesian coordinates of an optional domain or ship velocity. Equations (3.13)-(3.15) are valid for deep water waves with $\frac{\lambda}{2} \leq$ *water depth*.

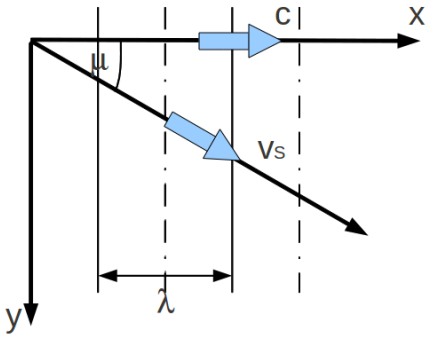

Figure 3.4: Definition of the encounter angle between the wave direction and the ship's course.

The equations are then used to determine the boundary variables for the transport variables in eq. 3.8 and 3.11. Alternatively to the Airy theory, also the Stokes theory can be used to compute the boundary variables. In the Stokes theory, the boundary condition at the free surface is fulfilled at the actual free surface position. This makes the theory non-linear, but valid for a larger wave steepness compared to the Airy theory. The available implementation in *FreSCo*$^+$ refers to third order stokes waves. The required equations for the velocity components and the height of the free surface can be found in Cieslawski [20]. For offshore applications the Stokes theory of 5th order is used sometimes to compute impact loads of extreme waves (see Kleefsman [42] for details). Another possibility for generating the waves is to use an external program. Then, waves of arbitrary shape or a superposition of wave components can be generated at the inflow of the computational domain as demonstrated in Clauss [21]. Here, the author couples a potential-flow based finite-element method with a VoF-based RANS solver to compute wave loads. This coupling allows the use of very compact domains in the RANS solver and therefore, reduces the computational times.

3.4.3 Modelling of moving bodies

To determine the motions of a vessel in waves, a 6 degree-of-freedom motion solver is coupled to the RANS equations. Another type of motion model is used to account for the rotations of the propeller. In this case, the axis of rotation is constant over time, which makes the solution of the equations of motions unnecessary. For both types of movements, rigid-body motions of the whole computational domain including the body are applied. Thus, in every time step the grid is moving and a resulting mass flux through

the faces of a control volume is generated:

$$\dot{m} = \int_S \rho(\mathbf{v} - \mathbf{v_B}) \cdot \mathbf{n} dS \,, \tag{3.16}$$

with $\mathbf{v_B}$ being the velocity due to the movement of the grid and $\dot{m}$ being the mass flux. This relative flux has to be considered in the governing transport equations by replacing the velocity $(\mathbf{v})$ with the relative velocity $(\mathbf{v} - \mathbf{v_B})$. The conservation of mass and the conservation of momentum then become:

$$\frac{\partial}{\partial t} \int_V \rho dV + \int_S \rho(\mathbf{v} - \mathbf{v_b}) \cdot \mathbf{n} dS = 0 \,, \tag{3.17}$$

and

$$\frac{\partial}{\partial t} \int_V \rho \mathbf{v} dV + \int_S \rho \mathbf{v}(\mathbf{v} - \mathbf{v_b}) \cdot \mathbf{n} dS = \int_S \mathbf{T} \cdot \mathbf{n} dS + \int_V \rho \mathbf{b} dV \,, \tag{3.18}$$

respectively. Naturally, an analogues substitution is also applied for all other scalar transport equations.

During a simulation using the moving-grid technique, the new position of the body has to be determined in each time step. For the prescribed motions (i.e. the rotations of a propeller), the position of the body can easily be computed, as the direction of the rotational axis does not change in time and also the angle of rotation is constant. This technique is used to simulate the rotating propeller in chapter 5. Thus, the propeller is not simulated in a moving frame of reference approach as described in section 3.1.2, since the periodic boundary condition for the flow around the different blades can not be applied for propellers interacting with the free surface.

However, prescribed rotations can not be used to describe the motion of a vessel in waves. Instead of this, in each time step the new position of the vessel has to be determined as part of the solution procedure by coupling the equations of motions to the flow solver. This coupling is done by computing the forces and moments acting on the body inside the RANS solver and by using this data in the equations of motion to determine the accelerations of the body. To simplify the coupling, two coordinate systems are used:

- A global (inertial) coordinate system: This frame of reference is non-moving and it is used to describe the flow equations. Typically, the z-axis is pointing upwards, while the x- and y-axis span the horizontal plane.
- A body-fixed (local) coordinate system: This reference frame is attached to the centre of gravity of the floating body and moves with it. Typically, the x-axis points to the bow of the ship, while the z-axis is directed upwards. This coordinate system is used to simplify the equations of motion.

For non-moving bodies and at the beginning of a simulation, both coordinate systems are aligned parallel. For moving bodies a rotation matrix is necessary, which describes the relation between a vector in the inertial and the local coordinate system and vice versa:

$$\hat{\mathbf{x}} = \mathbf{\Omega}^{\boldsymbol{T}}\mathbf{x}. \tag{3.19}$$

In this equation $\mathbf{x}$ is an arbitrary vector and $\mathbf{\Omega}$ is the matrix of rotation. Here and in the remainder of this section vectors described in the local coordinate system are marked with the $\hat{(\cdot)}$ accent.

According to the rotation theorem of Euler, a coordinate transformation can be described by a single rotation around an appropriate axis. Thus, the kinematic of a moving body can also be depicted, if this axis is known (see Magnus and Müller in [55]). A common procedure to determine this rotational axis for an arbitrary movement of a body is to use Euler angles, as described by Xing [90]. Using these, the rotation is described by three consecutive rotations in a specified order. An alternative formulation for the rotational matrix can be derived on the basis of Euler parameters or quaternions, which is used in *FreSCo*$^+$. Then, a transformation can be described using four parameters, i.e. three coordinates of the rotation axis n_i and the angle ϕ . These four Euler parameters

$$e_0 = cos\left(\frac{\phi}{2}\right), e_i = (e_1 \;\; e_2 \;\; e_3)^T = n_i \; sin\left(\frac{\phi}{2}\right) \tag{3.20}$$

define a unit quaternion in the scalar-vector representation (e_0, e_i). The resulting four-component vector:

$$\mathbf{p} = (e_0 \;\; e_1 \;\; e_2 \;\; e_3)^T \tag{3.21}$$

describes the position of the body in space. Using this definition the matrix of rotation becomes:

$$\mathbf{\Omega} = \begin{bmatrix} 2({e_0}^2 + {e_1}^2) - 1 & 2(e_1e_2 - e_0e_3) & 2(e_1e_3 + e_0e_2) \\ 2(e_1e_2 + e_0e_3) & 2({e_0}^2 + {e_2}^2) - 1 & 2(e_2e_3 - e_0e_1) \\ 2(e_1e_3 - e_0e_2) & 2(e_2e_3 + e_0e_1) & 2({e_0}^2 + {e_3}^2) - 1 \end{bmatrix} \tag{3.22}$$

The benefit of the quaternion representation is the avoidance of limitations for the rotational motions. Compared to this, singularities can occur in the coordinate transformation, if the formulation is based on Euler angles.

Henceforth, the kinematics of the floating body are described with the aforementioned formulations. To derive the relations between the forces and moments acting on the body and the resulting motions, Newtons second law is applied. Using this, the translatory accelerations follow from the conservation of the linear momentum

$$\mathbf{f} = \frac{d}{dt}(m \cdot \dot{\mathbf{x}}_{\mathbf{G}}) = (m \cdot \ddot{\mathbf{x}}_{\mathbf{G}}), \tag{3.23}$$

where the latter expression is valid, if the mass of the body (m) does not vary over time. In this equation, the vector $\mathbf{f}$ contains the forces acting on the body and $\ddot{\mathbf{x}}_\mathbf{G}$ is the vector of translational acceleration of the centre of gravity. The rotational accelerations can be determined from the conservation of angular momentum:

$$\mathbf{m} = \frac{d}{dt}(\mathbf{J} \cdot \boldsymbol{\omega}) = \mathbf{J} \cdot \dot{\boldsymbol{\omega}} + \boldsymbol{\omega} \times \mathbf{J} \cdot \boldsymbol{\omega}, \tag{3.24}$$

where $\boldsymbol{\omega}$ denotes to the angular velocity and $\mathbf{m}$ contains the moments acting on the body. Analogues to eq. 3.23, the last formulation is only valid if the tensor of inertia ($\mathbf{J}$) does not depend on the simulation time. However, in the global coordinate system this is not the case, but in the body-fixed coordinate system. Using the orthogonal matrix $\boldsymbol{\Omega}$ and the relation $\boldsymbol{\Omega}\,\hat{\mathbf{J}}\,\boldsymbol{\Omega}^{\boldsymbol{T}}$, the tensor of inertia can be expressed in the local coordinate system, while the conservation of angular momentum is still formulated in the global coordinate system, viz.:

$$\mathbf{m} = \boldsymbol{\Omega}\,\hat{\mathbf{J}}\,\boldsymbol{\Omega}^{\boldsymbol{T}} \cdot \dot{\boldsymbol{\omega}} + \boldsymbol{\omega} \times \boldsymbol{\Omega}\,\hat{\mathbf{J}}\,\boldsymbol{\Omega}^{\boldsymbol{T}} \cdot \boldsymbol{\omega} \tag{3.25}$$

In the body-fixed coordinate system, the tensor of inertia can be calculated according to the following formula:

$$\hat{\mathbf{J}} = \int_V \rho \begin{bmatrix} \hat{y}^2 + \hat{z}^2 & -\hat{x}\hat{y} & -\hat{x}\hat{z} \\ -\hat{y}\hat{x} & \hat{x}^2 + \hat{z}^2 & -\hat{y}\hat{z} \\ -\hat{z}\hat{x} & -\hat{z}\hat{y} & \hat{x}^2 + \hat{y}^2 \end{bmatrix} dV, \tag{3.26}$$

with $\hat{x}, \hat{y}, \hat{z}$ being the coordinates of one mass point in the local coordinate system. The use of the local coordinate system results in an uncoupling of rotatory and translatory degrees of freedom. Single degrees of freedom can easily be suppressed, if the corresponding acceleration in the local coordinate system is set to zero.

After the accelerations are computed, the velocity and the position of the body can be determined by integration. For the translational degrees of freedom the integration is straightforward, but for the rotational degrees of freedom the procedure is more complex: The angular acceleration ($\dot{\boldsymbol{\omega}}$) can be integrated to obtain the angular velocity ($\boldsymbol{\omega}$), but a second integration to obtain the rotational position is not possible. However, a formulation is feasible, which correlates the angular velocity and the Euler parameter $\mathbf{p}$, to describe the angular position in the quaternion formulation:

$$\frac{d}{dt}\,\mathbf{p} = \frac{1}{2}\mathbf{L}^{\mathbf{T}}\hat{\boldsymbol{\omega}}, \quad \text{with} \quad \mathbf{L} = \begin{bmatrix} -e_1 & e_0 & e_3 & -e_2 \\ -e_2 & -e_3 & e_0 & e_1 \\ -e_3 & e_2 & -e_1 & e_0 \end{bmatrix} \tag{3.27}$$

More details on the quaternion approach, which is used in *FreSCo*$^+$ can be found in Koliha [43]. Further explanations on the coupling of the motion solver and the flow equations can be derived from Manzke [56].

3.5 Description of the used boundary-element method

The second computational method used in this thesis is the boundary-element method *panMARE*, which is used as one of the baseline methods in the coupling approach described in chapter 4. Analogues to *FreSCo*$^+$ also *panMARE* is an in-house development of the Institute for Fluid Dynamics and Ship Theory at Hamburg University of Technology. The program is based on a propeller-flow code initially developed at the University Duisburg-Essen. More details about *panMARE* can be found in Bauer et. al. [6]. In *panMARE* the flow is considered to be irrotational, incompressible and inviscid. Thus, the Navier-Stokes equations can be simplified to the Laplace equation and the flow can be described by a velocity-potential

$$\nabla\Phi = \frac{\partial^2\Phi}{\partial x^2} + \frac{\partial^2\Phi}{\partial y^2} + \frac{\partial^2\Phi}{\partial z^2} = 0\,. \tag{3.28}$$

The total potential (Φ) contains the potential of the steady inflow velocity (ϕ_∞) as well as the perturbation potential (ϕ)

$$\Phi = \phi_\infty + \phi\,. \tag{3.29}$$

For the calculation of the velocity potential, the body surfaces as well as a possible existing water surface are covered with two-dimensional panels. For each of these panels the perturbation potential can be determined numerically. Due to the linearity of the Laplace equation, the potential can be expressed by a superposition of elementary solutions. Applying Green's third identity on the Laplace equation, the following expression can be derived for the perturbation potential at an arbitrary point $(\mathbf{x})$ in the flow:

$$\phi(\mathbf{x}) = -\frac{1}{4\pi}\left(\sum_{j=1}^{N_B}\sigma_j\int_{A_j}\frac{1}{\mathbf{r}_j(\mathbf{x})}ds + \sum_{j=1}^{N_B+N_W}\tau_j\int_{A_j}\mathbf{n}_j\nabla\frac{1}{\mathbf{r}_j(\mathbf{x})}ds\right) \tag{3.30}$$

Here, σ_j refers to the respective source strength at the panel j. N_B refers to the number of panels on the body surface, while τ_j is the dipole strength. The doublets are placed at the panels of the body surface as well as at the panels on the trailing wake (N_W). A_j denotes the surface area of the specific panel, with n_j being the surface normal pointing into the flow. The distance between the point x and the centre of an arbitrary panel j is stored in the vector $\mathbf{r}$. The strength of the sources is estimated by fulfilling the boundary condition $(\nabla\Phi = 0)$ on the body surface:

$$\sigma = -\mathbf{n}\cdot\mathbf{v}_\infty \tag{3.31}$$

By using this boundary condition, which prohibits the flow through the panel surface, the displacement of the floating body is modelled. The respective lift of the body is generated

by the doublets at the body surface and on the wake panels. To determine the respective strength, another boundary condition is necessary, as only N_B equations for $N_B + N_W$ unknowns are available. This missing condition is the Kutta condition, which is applied at the panels directly at the trailing edge (TE) to achieve a vanishing pressure difference at the trailing edge between the pressure and the suction side:

$$\tau_{TE} = \tau_{suction} - \tau_{pressure} \tag{3.32}$$

Here, $\tau_{suction}$ is the dipole strength of the directly attached panel on the suction side, while $\tau_{pressure}$ is the analogues value on the pressure side. The subsequent panels in the wake of each blade are deformed according to the local flow direction as can be seen in fig. 3.5.

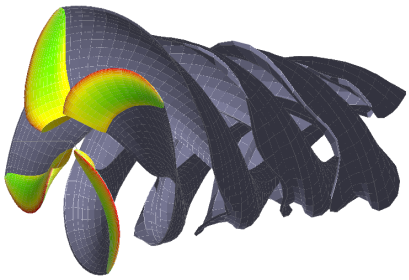

Figure 3.5: Exemplary result of *panMARE*: The blades are coloured with the pressure distribution and the wake panels are deformed according to the flow condition.

Afterwards the equation system can be solved to determine the unknown dipole strength of the doublets at the N_B body panels. In the standard approach of *panMARE* the direct formulation is applied, where the velocity potential itself is computed and the velocities at the panel centres are determined by differentiation. This is done by using the velocity derivatives of the surrounding panel centres to determine the velocity value at the actual panel. Finally the Bernoulli equation is used to compute the pressure (p) at each point x:

$$-\frac{p(\mathbf{x})}{\rho} = \nabla\phi(\mathbf{x})^2 + \nabla\phi_\infty\nabla\phi(\mathbf{x}) + \dot{\tau}_x. \tag{3.33}$$

Due to the missing rotation in potential theory, friction effects can not be computed directly. Instead of this, empirical correlations are used in *panMARE* to determine the friction forces. Analogues to the moving frame of reference approach in RANS-type propeller computations, described in section 3.1.2, symmetry effects can be used for the simulation of propellers in open water conditions. Then, only one blade has to be considered by using a periodic-boundary condition. However, in the method described in the following chapter and in the remainder of this thesis, this approach can not be used, due to the non-uniform inflow conditions in most cases.

4 Coupling procedure to calculate the propeller flow

The coupling algorithm described in this chapter combines the potential-flow method *panMARE* and the viscous-flow method *FreSCo*$^+$ to simulate the flow around propellers. The approach shows some similarities to the procedures described in section 3.2.2. Analogues to these procedures, the major aim of this present development is to combine the proven capabilities of RANS-based methods in predicting the velocities in a wake field, and the fast computational times of potential-flow methods. During a coupled simulation, the propeller is not geometrically modelled in the viscous-flow solver, which reduces the computational times compared to RANS simulations of the appended hull as described in chapter 3.2.1. Contrary to the already existing coupling methods, the approach presented here shall also be able to predict the performance of partly submerged and ventilating propellers. Henceforth, the flow around the single blades has to be captured. Radial or circumferential averaging of forces as proposed for example in Stern [82] or an averaging in time as described in Zawadzki [93] can not be used in this case. Instead of this, the procedure aims to model the single blades as accurate as possible.

The following section describes the required data transfer to couple the two baseline methods, before the different variants of the unsteady procedure are explained. In the subsequent section, the extended version of the coupling procedure for ventilating propellers is outlined. Finally, the coupling procedure is validated with the help of three test cases.

4.1 Description of the algorithm

Analogues to the approaches described in section 3.2.2 the propeller is not modelled geometrically in the viscous-flow solver. Instead of this, volumetric body forces are imposed in the viscous-flow solver to model the impact of the propeller. To capture the flow around the propeller blades as closely as possible, the respective forces shall be applied in the actual blade positions without any averaging of forces. Thus, only the cells in the actual blade positions are covered with forces and the position of the body forces is not

geometrically fixed during the computation. The required forces are determined by the potential-flow method *panMARE*, while the viscous-flow method is used to calculate the inflow condition towards the propeller. In doing so, the approach combines the advantages of both methods. Potential-flow methods have proven capabilities to predict the propeller forces and moments, if the inflow and the operating conditions of the propeller are known. In addition to this, the computational effort is significantly smaller than in field methods. On the other hand, the correct prediction of viscous effects in a ships wake is crucial for computing the inflow conditions towards the propeller. Henceforth, this part of the computation should be done with a viscous-flow method. Thus, the coupling approach comprises of two parts:

- The calculation of the forces and moments by *panMARE* and
- the simulation of the inflow condition by *FreSCo*$^+$.

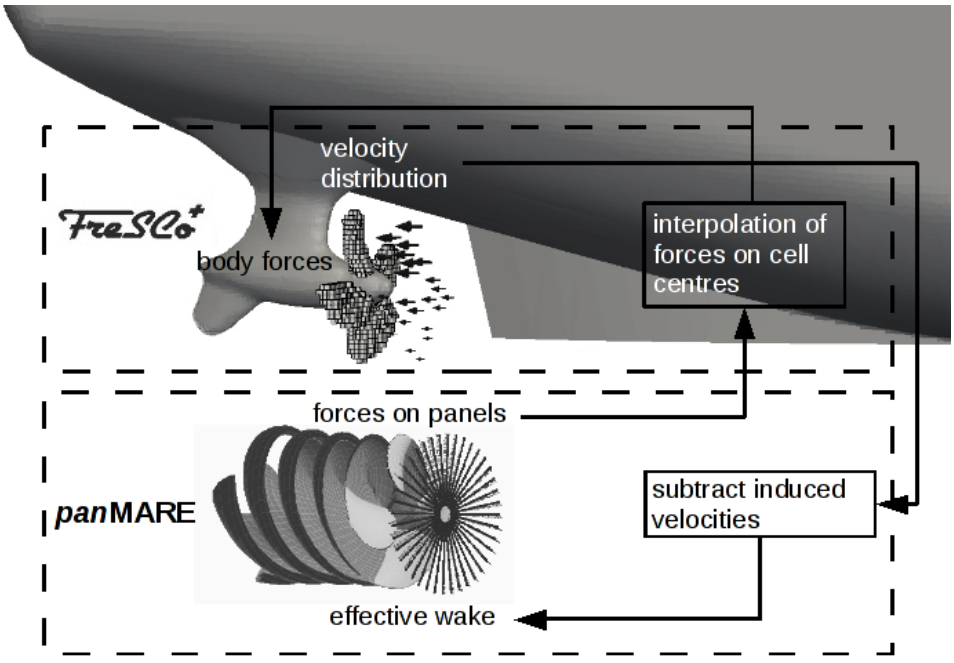

Figure 4.1: Illustration of the data transfer in the coupling approach.

Figure 4.1 illustrates the necessary data transfers during a coupled simulation and shows the tasks of the two baseline methods. Each coupling cycle starts by extracting the approach flow in a plane in front of the propeller inside the viscous-flow method. Afterwards, the velocity data is transferred to the inviscid method, where the induced velocities have to be subtracted to determine the effective wake. Using this wake as inflow condition,

the forces on the propeller blades are determined by *panMARE*. This force distribution is then transferred back to *FreSCo*$^+$, where the forces are distributed to the cells in the actual blade positions.

For the transfer of the velocity data a circular plane is defined, which is typically located 0.2D-0.5D upstream from the propeller. The locations for the single velocity data inside the plane are defined by the corresponding angular and radial points as shown in fig. 4.2 on the left hand side. The number of coordinates is one of the input parameters to *FreSCo*$^+$. Additionally, a non-equidistant distribution of wake-field points can be achieved with the input settings. This may be necessary for an improved capturing of regions with large gradients in the wake field. These points in the transfer plane are not necessarily points of the computational grid used in *FreSCo*$^+$. Thus, an interpolation routine is necessary to determine the velocities at the wake-field points. For each point of the transfer plane, the cell is searched, which contains the point. Afterwards, the neighbouring cells of this cell and the distances between the respective cell centres and the actual velocity point are determined. Using the reciprocal value of these distances as interpolation weights, the velocity value at the actual point can be determined.

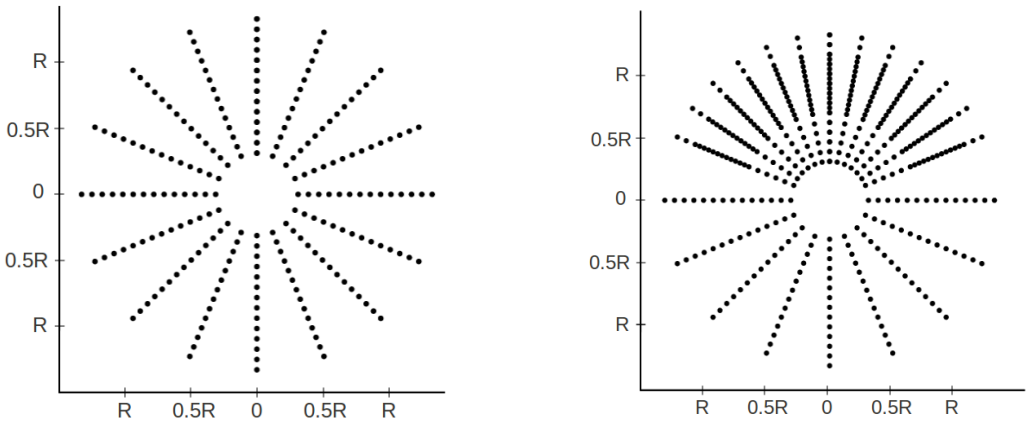

Figure 4.2: Positions for the velocity transfer between the viscous- and the inviscid-flow method. The positions are described in polar coordinates. The picture on the right hand side illustrates the possibility to use a local refined grid.

During a coupled simulation, the communication between both solvers is achieved via reading and writing of ASCII data-files. The file for the velocity transfer is defined in the XML data-format to use an already existing functionality of *panMARE*.

The transfer of forces from the potential-flow method to the RANS solver follows a different procedure without an additional transfer grid. Instead of this, for each panel of the *panMARE* grid, one force vector is transferred. Thus, separate forces for the pressure and suction side of the blade are considered. Inside *FreSCo*$^+$, the forces are then

distributed to the adjacent fluid cell centres of the RANS mesh as volumetric body forces. The corresponding mapping-procedure is illustrated in fig. 4.3 for a two-dimensional blade section. In the background of both pictures the RANS mesh is indicated by grey lines. As the grid for the viscous-flow method does not contain the geometry of the blade, an equidistant Cartesian grid can often be used in the propeller plane. However, cells of arbitrary shape and dimension are possible as well due to the unstructured data-structure of *FreSCo*$^+$. The sketch on the left hand side of fig. 4.3 illustrates the first step of the interpolation procedure, where one panel of the *panMARE* grid is displayed in red. The red cross marks the centre of this panel, where the value of the respective force vector is stored. The interpolation algorithm then determines the cell of the RANS mesh, which contains the centre of the actual panel. This cell is highlighted in the picture with black lines and the corresponding cell centre is depicted as well. Analogues to the interpolation of the velocity data, the algorithm then determines the neighbouring cells and the distances between the cell centres and the position of the panel centre. This second step of the interpolation procedure is depicted in the figure on the right. The neighbouring cell centres are marked with red dots and the distances are illustrated with the black arrows. Again, the reciprocal value of these distances is used as interpolation weight to distribute the forces to the involved cells of the RANS mesh. Although this procedure allows the use of significantly different grids in the two baseline methods especially in means of the grid density, the mapping procedure maintains force conservation.

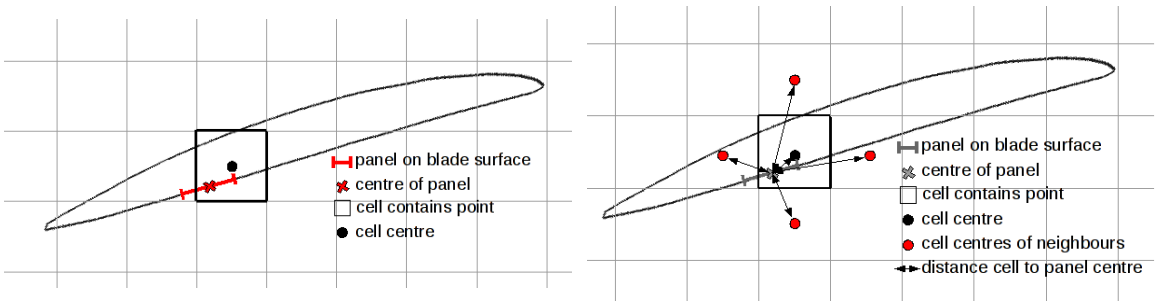

Figure 4.3: Illustration of the procedure for the transfer of the forces calculated by *panMARE*. The left picture displays the first step of the interpolation, where the cell is determined which contains the actual panel centre. The following step is illustrated on the right hand side, where the neighbouring cells are determined.

An exemplary result of the force transfer is shown in fig. 4.4. The figure depicts the cells in the blade positions, which are covered with body forces. The color code refers to the magnitude of the body-force vector. If the grid density in the RANS method is sufficiently fine, the algorithm is able to predict the shape of the blade contour accurately and different force-distributions for the pressure and suction side of a blade are obtained. Henceforth, compared to other coupling approaches with averaged distributions of forces,

the flow in the blade regions is captured in more detail in the present method. For example, the trailing vortices in the wake of each blade are generated as well, due to the pressure difference between the pressure and suction side.

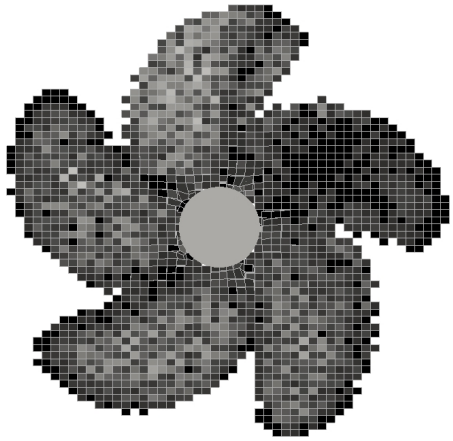

Figure 4.4: Example for a propeller modelled with body forces, applied in the actual blade positions.

The described data transfer is done in each cycle of the coupling procedure. In the following subsection, the different variants of the unsteady algorithm are described and it is explained how often the data is exchanged between the two involved methods.

4.1.1 Baseline approach for deeply submerged propellers

This subsection describes the general work-flow of the baseline coupling procedure. The baseline version contains the exchange of velocity and force data in the single coupling cycles and is suitable for deeply submerged propellers. The implemented unsteady algorithm is developed in two variants. The first one refers to an explicit algorithm using one data exchange per time step, while the second one is an implicit mode with multiple data exchanges per time step. The differences between both methods and the general work-flow of the unsteady coupling method are illustrated in fig. 4.5.

Except for open-water calculations, each coupled simulation is started by using the result of a RANS computation without the working propeller as initial condition. The nominal wake field resulting from this simulation can then be used in the first coupling cycle as inflow condition for the potential-flow solver. Additionally, a number of steady iterations inside *panMARE* is simulated beforehand to determine a converged solution of the inviscid flow. Henceforth, at the starting time of the algorithm the viscous flow towards the

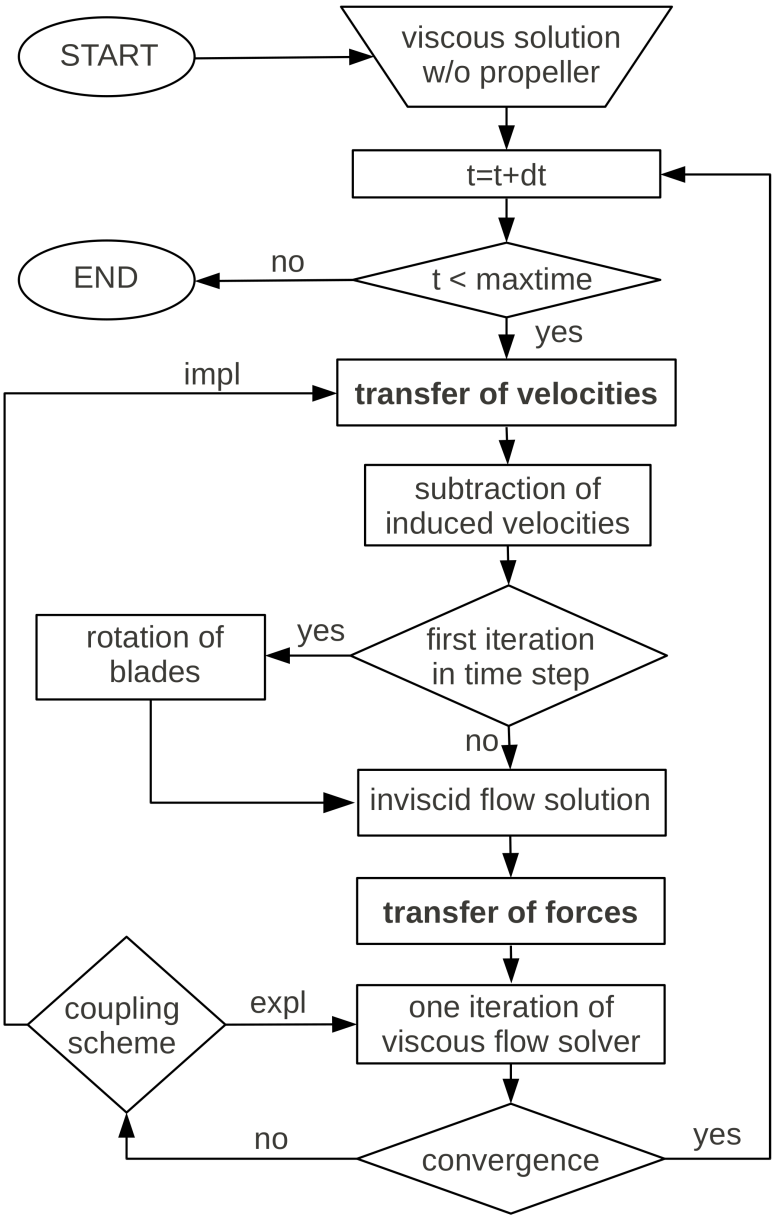

Figure 4.5: Work-flow of the coupling procedure.

propeller plane as well as the inviscid flow around the propeller is fully developed. At the beginning of each coupling cycle the velocity distribution upstream of the propeller plane is transferred to the inviscid-flow method. These velocities refer to the nominal wake field in the first time step. In the subsequent time steps the velocity distribution is determined including the effect of the working propeller. Thus, the transferred velocities contain the effective wake as well as the propeller induced velocities. In the next step, *panMARE* uses this total wake field to determine the propeller induced velocities, as these velocities have to be subtracted from the total velocities before the propeller forces can be computed. Otherwise the impact of the propeller induced velocities would be considered twice. The result of this effort is the effective wake, which is used as inflow condition. The algorithm proceeds with the solution of the equation system inside *panMARE* to determine the propeller forces. This force distribution is transferred back to the viscous-flow method. In the explicit mode only one coupling cycle is performed at the beginning of each time step. Afterwards, the time step is finalized by the solution of the governing equations in *FreSCo*$^+$ until a converged solution in the respective time step is achieved. Then, the next time step and therefore a new coupling cycle starts by transferring a new velocity distribution to the inviscid-flow solver. Thus, the explicit mode is not time accurate as the velocities and therefore the inflow condition for *panMARE* is based on the flow condition of the previous time step of the viscous-flow solver, as illustrated in the flowchart in fig. 4.5.

In the implicit version of the coupling algorithm, multiple coupling cycles are performed in each time step. Here, the inviscid solution is embedded into the outer iteration process of *FreSCo*$^+$. As depicted in the flowchart, this is implemented by exchanging the respective force and velocity data after each outer iteration in *FreSCo*$^+$. Thereby, the algorithm becomes time accurate as the inflow condition used in *panMARE* corresponds to the actual blade position. However, this increased accuracy results in remarkable larger computational times. Additionally, a third technique is implemented, which is placed between the explicit and implicit version in terms of accuracy and computational effort. This semi-explicit variant iterates the induced velocities to convergence before a new distribution of forces is determined. The general work flow of this mode follows the explicit mode, but the equation system of *panMARE* is solved several times within one coupling cycle. In each of these additional inviscid iterations, a new set of induced velocities is computed based on the induced velocities of the former iteration and the total wake field provided by *FreSCo*$^+$. A new set of propeller forces is then transferred to the RANS method, when a converged solution for the induced velocities is found. Although this approach is questionable due to the obvious inconsistencies between the involved velocity fields, it might provide an improved accuracy compared to the fully explicit mode and decreases the computational effort compared to the implicit strategy. In section 4.2.2 all variants of the coupling procedure are analysed in terms of computational efficiency and accuracy to obtain the most promising and efficient procedure for practical applications.

4.1.2 Variant for propellers interacting with the free surface

The algorithm described beforehand can be used for the simulation of the propeller flow in deeply submerged conditions in uniform or non-uniform inflow. To account for possible ventilating propellers, the coupling procedure has to be extended for two-phase flows. Inside the viscous-flow method, free surface effects are modelled with the help of a volume of fluid method as explained in section 3.4.2. Therewith, the interaction of the body-force propeller and the free surface is simulated in *FreSCo*$^+$. To consider the interaction of the propeller and the free surface also in *panMARE*, the interface position must be transferred to the inviscid-flow method. Inside *panMARE* the position of the free-surface is kept constant during one time step, and it is assumed that the panels on the free surface are disregarded in the solution process by neglecting the pressure on these panels. The position of the interface is used to determine the emerged propeller panels. The dipole strength of these panels is then set to zero to account for the thrust losses due to the out-of-water effect. In doing so also partly immersed propellers can be simulated with the coupling procedure. Due to a partly emerged and ventilating propeller, the shape of the free surface can be rather complex as displayed in fig.4.6.

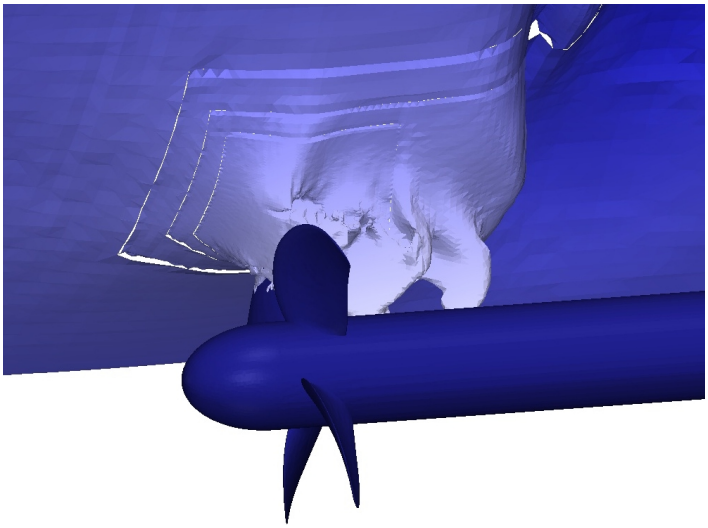

Figure 4.6: Example for a complex free surface shape above a ventilating propeller. The picture is obtained from a *FreSCo*$^+$ calculation.

The picture depicts a result of a *FreSCo*$^+$ calculation with a propeller in open water conditions operating at an advance ratio of $J = 0.15$ and an immersion ratio of $H/R = 1.5$. As can be seen from the figure, the interface between water and air is not necessarily a closed surface without any defects. Thus, an algorithm is required, which can capture this highly unsteady behaviour of the free surface, by providing the possibility of

transferring an arbitrarily shaped free surface from *FreSCo*$^+$ to *panMARE*. Furthermore, the grid density in the two baseline methods might differ significantly, which requires a grid-independent transfer method for the free surface shape. Otherwise, unnecessary restrictions to the two baseline methods and their respective numerical grids would occur. Another problem occurs, due to the used volume of fluid scheme in *FreSCo*$^+$. In this group of methods the free surface is not a boundary of the computational domain and so the interface has to be reconstructed from the local distribution of the mixture fraction by interpolation. Moreover, boundary element methods are not able to handle a ruptured free surface. Thus, the interface inside the inviscid method has to maintain a fair level of geometric continuity. To comply with these requirements, a three step algorithm of data-preparation is implemented in *FreSCo*$^+$ to provide the information of the free surface shape to *panMARE*:

- Reconstruction of the interface between water and air from the mixture fraction,
- interpolation of the free surface data on a structured grid,
- Fourier transformation of the free surface data.

The first step of the implemented algorithm reconstructs the free surface position from the VOF-based mixture fraction by detecting the cell faces in the free surface region. Thereby, the designated faces are those, where one neighbouring cell has a mixture fraction of $c <= 0.5$ while the other one has a mixture fraction of $c > 0.5$ as illustrated by fig. 4.7 on the left hand side. The algorithm uses the position of the cell centres only (marked with red dots) and is therefore independent of the given cell shape. In a second step a linear interpolation, illustrated by the right hand picture is performed. The aim of this step is to determine one point of the reconstructed interface by using the values of the two neighbouring cells.

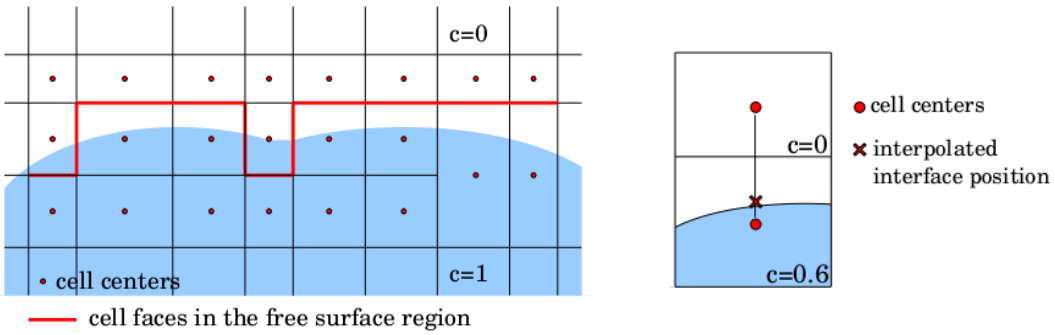

Figure 4.7: Reconstruction of the free surface positions. The left picture illustrates the search for cells in the free surface region, while the right picture explains how one point of the interface is determined by interpolation.

Finally, this results in an unstructured representation of the free surface. To prepare the data for the following Fourier transformation, the data has to be mapped to a structured grid. Therefore, a regular distribution of grid points in the two horizontal directions is created. The orientation of the coordinate directions of this intermediate grid is specified as one of the input parameters for *FreSCo*$^+$. At these points, the height of the free surface is determined by interpolation. The interpolation procedure is illustrated in fig. 4.8 for a two-dimensional example. For each point of the structured grid the two closest points of the unstructured free surface description are detected. Then, the height at the point of the structured grid can be computed based on the surface height at the two neighbouring points.

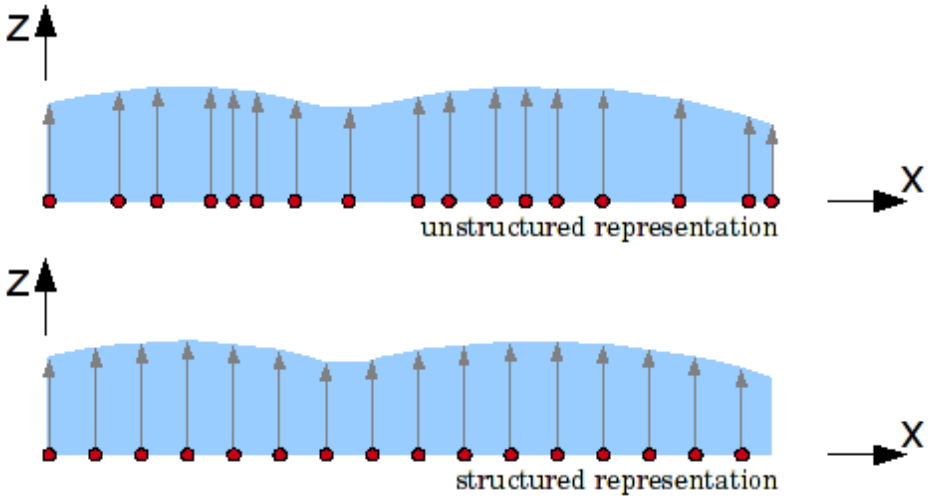

Figure 4.8: Interpolation of the unstructured free surface representation on a structured grid.

Afterwards, the Fourier transformation can be performed on the data of the structured grid. This results in an analytical description of the free surface. The respective Fourier coefficients are then transferred via a XML-formatted file to *panMARE*. Inside the potential-flow solver, the free surface height can then be computed at arbitrarily chosen positions of the panel grid by applying the following formula to each coordinate:

$$z_{panMARE} = A_0 + \sum_{k=1}^{n} \left(A_k cos(2\pi k \frac{x}{L_x}) + B_k sin(2\pi k \frac{x}{L_x}) \right). \tag{4.1}$$

In this equation $z_{panMARE}$ denotes the free surface height at one specific point, while A_k and B_k are the Fourier coefficients calculated by *FreSCo*$^+$. The variable x is the actual position of the interface point and L_x is the domain length. For a two-dimensional case

the position of the interface can be described by eq. 4.1. To determine the shape of the free surface for a three-dimensional case, several sets of Fourier coefficients are necessary. Normally, the direction of approach flow towards the propeller coincides with the direction of the Fourier transformation. Thus, the different sets of coefficients are used for the different locations in transverse direction. Inside *panMARE* the free surface is modelled as a fixed boundary in each time step. Thus, the interface positions are not adapted to fulfil the kinematic or dynamic boundary condition in the solution process of the BEM. To implement this transfer of free surface data into the coupling procedure shown in the flowchart in fig. 4.5, a supplementary file containing the free surface data is transferred to *panMARE* every time the velocity distribution is exchanged to also update the position of the interface.

4.2 Verification and validation of the coupling procedure

The following subsections are dedicated to a validation of the before described coupling approach. The first test case refers to the simulation of an open-water propeller. The computed thrust and torque coefficients are compared to experimental values. The further aim of this case is to determine the influence of different computational parameters on the results. Afterwards, the propeller induced velocities for a one-bladed variant of the before investigated propeller are studied. Since the coupling algorithm assumes that the propeller induced velocity field calculated by *panMARE* equals the velocity field induced by the body-force propeller in *FreSCo*$^+$, the determination of the induced velocities is one of the most critical aspects of the coupling algorithm with respect to the computational accuracy. For propellers operating in the vicinity of the free surface the accuracy of the free surface transfer is important as well, to ensure equivalent working conditions of the propeller in both solvers. This aspect is investigated in the third subsection. The present section is finalised by the investigation of an operating propeller behind a container ship.

4.2.1 Propeller in open water

This test case investigates the functionality of the baseline algorithm by simulating a propeller in open water. Further aim of this test is to study the performance of the different coupling modes, as this parameter is crucial for the computational times. The used propeller geometry refers to the one investigated experimentally by MARINTEK within the research project *PropSeas* (Kozlowska [50]). The same geometry is used for the simulations in chapter 5. According to the coupling procedure, no propeller geometry

is modelled inside *FreSCo*$^+$ and a simple Cartesian grid can be used for the computations. The left figure of fig. 4.9 shows a detail of the grid in the propeller plane. The coloured cells represent those blade regions, where the body forces determined by *panMARE* are applied. Overall, the *FreSCo*$^+$ grid consists of 15000 cells, where approximately 2500 cells are located in the blade positions. Thus, significantly smaller grids can be used for coupled computations compared to simulations of a geometrically resolved propeller. The resolution of the panel-grid in *panMARE* with 544 panels per blade is shown in the right hand picture in fig. 4.9.

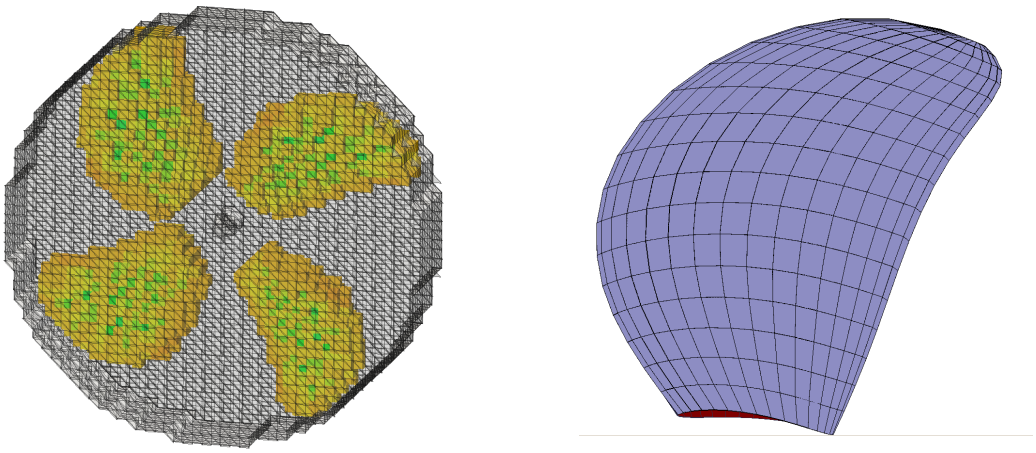

Figure 4.9: Computational grids for the simulation of the propeller in open water. The left hand picture displays the grid of the viscous-flow solver. In this figure, the cells in the actual blade positions are coloured with the magnitude of the respective body-force vector. In the right picture the panel grid of *panMARE* is shown for one blade.

The simulations are performed with the explicit and implicit coupling mode. In both cases ten outer iterations are performed in each time step and the time-step size is set to $dt \cdot n = 3.78°$. The convergence of the computed thrust coefficient for an advance ratio of $J = 0.9$ is shown in fig. 4.10 on the left. The figure reveals almost equivalent thrust values for the implicit and explicit coupling algorithm in the individual time steps. Due to the increased number of coupling cycles in the implicit mode, remarkably larger computational times are observed in this case.

To reduce the computational effort of the implicit algorithm, the convergence of the computed thrust values is monitored in the single outer iterations, as displayed in the picture on the right hand side of fig. 4.10. The figure depicts the thrust prediction for three consecutive time steps. The beginning of each time step is marked by a solid vertical line, while the dashed line represents the outer iteration, where the relative thrust change between two iterations falls below 1%. It is therefore possible to limit the amount of outer

iterations to this threshold, which reduces the necessary number of outer iterations to 5. In consequence, the computational times of the implicit are reduced by a factor of almost 2.

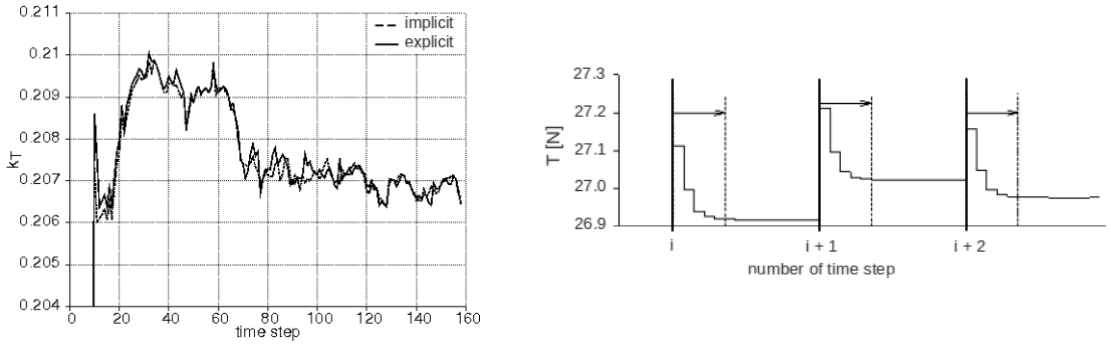

Figure 4.10: Convergence study of the predicted thrust values. The left diagram shows the computed thrust coefficient obtained with the explicit and implicit coupling algorithm for the first 160 time steps. The right figure shows the convergence behaviour of the implicit coupling mode within three subsequent time steps. The dashed lines indicate the fifth outer iteration.

Despite the reduced computational effort for the implicit mode, the simulation times are still significantly larger than for the explicit variant. Henceforth, the explicit mode is in the following used to compute the open-water values displayed in fig. 4.11. The figure depicts a comparison between the results for the coupling algorithm and the experimental values obtained by MARINTEK. Additionally, the results for pure inviscid simulations with *panMARE* are shown. A satisfactory agreement can be observed for the predicted thrust values, while larger deviations are visible in the torque values and therefore also in the values for the open water efficiency. As the results of the two computational approaches are in line, the discrepancy to the experimental values indicates inaccuracies inside the inviscid baseline method. A possible reason for this error can be the empirical determination of the surface-friction losses inside the inviscid-flow solver, which have a larger influence on the torque. The small deviation between the coupled result and *panMARE* might be a result of the different resolution of the pressure peak at the leading edge between the geometrically modelled propeller in the inviscid-flow solver and the body-force representation of the propeller in the viscous-flow solver.

4.2.2 Determination of induced velocities

This subsection is dedicated to an analysis of the propeller induced velocities. Inside the coupling procedure the induced velocities are determined by *panMARE* and are

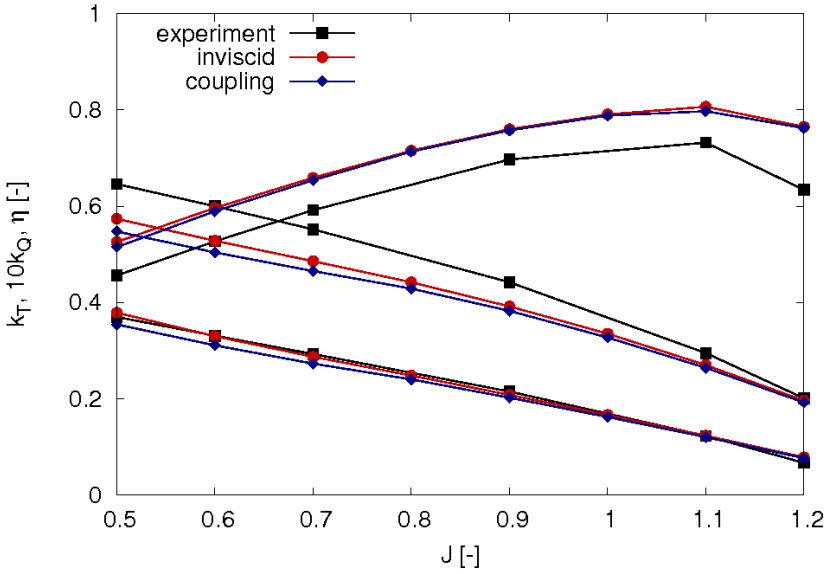

Figure 4.11: Comparison between the computed and measured open water values.

subsequently subtracted from the total velocities computed by *FreSCo*$^+$. Hence, it is important that the induced velocities computed by *panMARE* and the induced velocities of the body-force propeller in *FreSCo*$^+$ are similar. Otherwise non-equivalent working conditions for the propeller are obtained. In general, the approach flow towards the propeller (v_A), which is computed by the viscous-flow method consists of the nominal wake (v_N), the velocities due to the interaction of ship and propeller (v_E) and the propeller induced velocities (v_I):

$$\mathbf{v_A} = \mathbf{v_N} + \mathbf{v_E} + \mathbf{v_I}\,. \tag{4.2}$$

Without the presence of a floating body in front of the propeller, the interaction velocities vanish and the nominal wake reduces to the parallel inflow. Thus, it becomes possible to determine the propeller induced velocities from the approach flow by subtracting the parallel inflow. Then, the induced velocities can be compared to the induced velocities determined by *panMARE* to validate the accuracy of the coupling procedure. To further reduce the computational effort and for an easier comparison, a one-bladed propeller is used for the comparison of the induced velocities. The equivalent four-bladed propeller is the same as in the previous subsection and also the same computational grids and simulation parameters can be used. Table 4.1 provides an overview of the parameters, which are varied during the analysis of the induced velocities. In the table, the parameters marked with bold letters are set constant during a variation of one of the other parameters.

parameter	**values**
advance coefficient	0.2, **0.5**, 0.8
time-step size $(dt \cdot n)$	1.26°, **3.78°**, 7.56°
coupling mode	**explicit**, semi-explicit, implicit
distance to propeller plane	**1/2R**, 3/4R, R

Table 4.1: Parameters for the investigation of the propeller induced velocities.

In the following investigation, the propeller induced velocities are monitored at one fixed time step and a propeller radius of $r/R = 0.7$. For this blade position, which corresponds to the topmost position, the induced velocities are displayed for one variation of the circumferential coordinate between 0°and 360°. The induced velocities are displayed by means of the axial, radial and tangential velocity component and they are normalized with the respective parallel inflow velocity as depicted in fig. 4.12. As the flow towards the propeller is directed against the positive x-axis, negative axial velocity values denote for an acceleration of the flow. In the figure, the three components of the velocity vector are displayed with different symbols. The curve for the axial velocity shows a sharp decrease until it reaches a minimum at approximately 30°, which coincides with the position of the trailing edge of the blade. In the trailing path of the blade the curve shows a more smooth increase. This region is influenced by the free vortices leaving at the trailing edge of the blade. The maximum of the curve is reached after 315° in a region directly effected by the leading edge. The radial component of the induced velocity is directed inwards and shows a nearly constant course over the circumferential direction. The maximum of the tangentially induced velocities is directed in the direction of rotation and can be found at approximately 340°, which corresponds to one third of the chord length.

During the following analysis, only the results of the induced velocities in axial direction are shown. For this component a comparison is made between the velocities determined from the velocity field inside the viscous-flow solver and the velocities computed by *panMARE*. The curves obtained from the velocity field in *FreSCo*$^+$ are displayed with closed symbols and labelled with "RANS", while the curves showing the inviscid results for the induced velocities are plotted with open symbols and marked with "BEM". Both sets of curves are obtained from one coupled simulation. The first varied parameter refers to the advance coefficient as depicted in fig. 4.13. The displayed results are obtained for a time-step size of $dt \cdot n = 3.78°$ and the explicit coupling mode. The axial distance between the centre of the propeller and the plane, where the velocity distribution is extracted, is set to $dx/R = 0.5$. In general, the curves for the different advance coefficients show similar characteristics. The largest values for the propeller induced velocities are of course obtained for the smallest advance ratio, where the propeller loading is maximal. For this case significant deviations between the two methods can be observed, especially near the

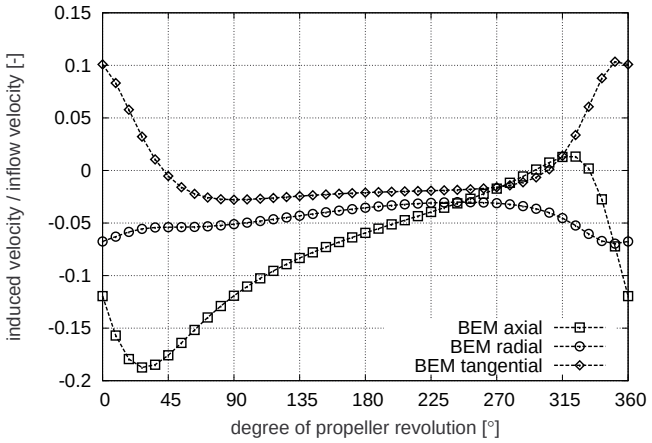

Figure 4.12: Components of the induced velocity vector ($J = 0.5$, $dx = 1/2R$, explicit coupling, $dt \cdot n = 3.78°$).

topmost position and in front of the leading edge. Under consideration of the difficulties in simulating highly loaded propellers with inviscid methods, this result seems to be still sufficiently accurate for the purpose of the coupling algorithm, as the error is in the range of 10% with respect to the total velocity. Additionally, the results for the two larger advance ratios show a better agreement.

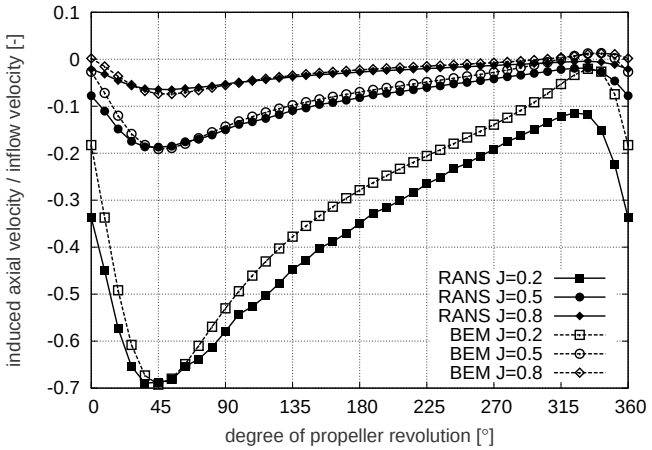

Figure 4.13: Comparison of the axial component of the induced velocity vector for different advance ratios.

The second investigation refers to the influence of the applied coupling mode on the

results. To facilitate the comparison, both pictures portray only the results for the upper half of angular positions. The advance coefficient is set constant to $J = 0.5$ during these computations and the velocities are again extracted in a distance of $dx/R = 0.5$ in front of the propeller. In the left picture of fig. 4.14 the results for the explicit and the implicit coupling mode are compared, while the right sketch displays the corresponding comparison between the results of the explicit and the semi-explicit mode. Overall the

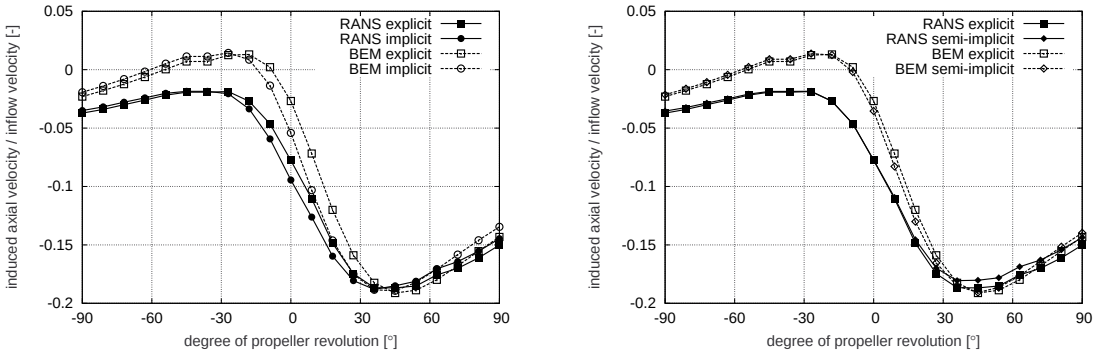

Figure 4.14: Comparison of the axial component of the induced velocity vector for the three implemented coupling modes ($J = 0.5$, $dx/R = 0.5$ and $dt{\cdot}n = 3.78°$).

results of the different coupling modes are quite similar. The main deviations between the different modes can be found with respect to the steep decrease of induced axial velocities between the leading and the trailing edge, which can be attributed to the different handling of the accuracy in time in the different variants of the algorithm. Here, the axial velocities computed with the implicit algorithm show a more steep decrease compared to the explicit results. Additionally, this decrease starts slightly earlier. The same tendency is also visible for the semi-implicit algorithm, but less measurably visible. The comparison between the results obtained from the viscous computed velocity field and the induced velocities determined by *panMARE* reveals a good agreement of the predicted minima, while larger maxima are predicted by the BEM. Apart from this, the deviations between the coupling approaches are small. In conclusion of this result, the explicit algorithm seems to be the most sufficient solution in terms of effectiveness and accuracy as the computational effort for the implicit algorithm is considerably larger. Henceforth, the explicit algorithm is used for the remaining computations in this chapter and also for the simulations in chapter 5 and 7.

Afterwards, the distance between the propeller and the plane, where the velocity data is extracted, is varied. The respective results are displayed in fig. 4.15 on the left hand side. For these simulations the time step amounts $dt \cdot n = 3,78°$ and the advance coefficient is again set to $J = 0.5$. The largest values for the induced velocities are of course obtained

for the smallest distance, but overall a satisfying correlation between the two methods is observed. Smaller distances between propeller and velocity plane can not be investigated, as the plane then coincides with the area swept by the propeller blades. However, the outcome of the comparison is that very small distances between propeller and transfer plane can be used without generating large discrepancies in the induced velocities. This is important for the simulations of propellers in behind conditions as the limited space between hull and propeller does not allow for a large distance between the velocity plane and the propeller.

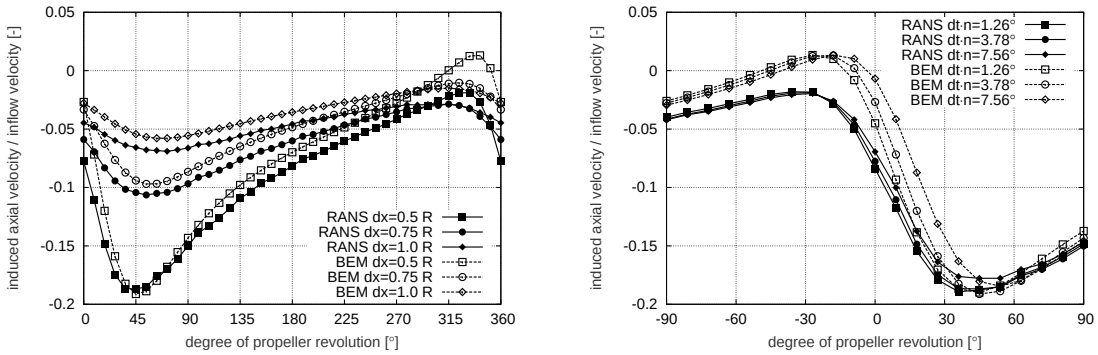

Figure 4.15: Comparison of the axial component of the induced velocity vector for different time-step sizes and distances between propeller and velocity plane.

From the right figure it is obvious that a larger time step increases the differences between the two methods. In case of the largest time step, a deviation in the position of the curve maximum can be observed additionally. This is due to the fact that the induced velocities are determined for different instants in time in the explicit coupling mode, as explained in section 4.1.1.

As the results described beforehand are obtained for a one-bladed propeller, the last results presented in fig. 4.16 display the analysis for the corresponding four-bladed propeller. Here, all components of the velocity vector are depicted for a simulation using the explicit coupling mode, an advance ratio of $J = 0.5$, the medium time step size and the smallest distance between velocity plane and propeller position. Overall a fair agreement for all components of the velocity vector is obtained, which allows to use the investigated parameter set in further simulations and demonstrates that the working conditions for the propeller in both solvers are similar.

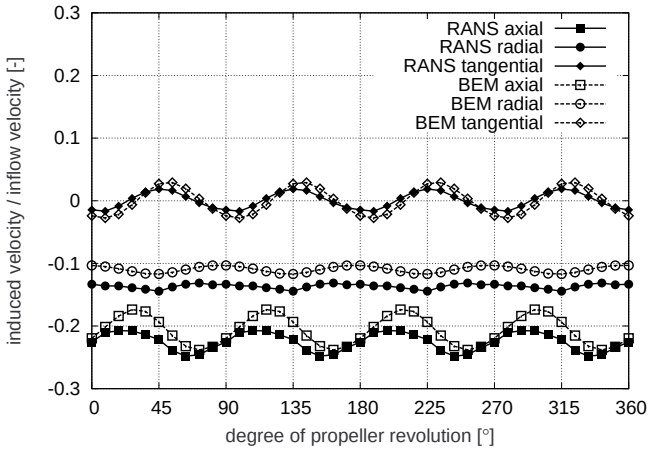

Figure 4.16: Comparison of the Cartesian components of the induced velocity for the four-bladed propeller operating at $J = 0.5$. The results are obtained with the explicit coupling mode.

4.2.3 Validation of the free-surface transfer

The quality of the interpolation algorithm for the transfer of the free surface position is evaluated with a simple two-dimensional test case, simulating the flow over a submerged hydrofoil. Experimental data for this case can be found in Duncan [25], where the shape of the free surface above the foil is measured. From these experiments a steady non-breaking wave contour is expected in the investigated case. The foil itself is a NACA0012 profile and it is placed in a distance of $H/c = 1.034$ below the free surface, where c is the chord length of the foil. The dimensions of the computational domain and the position of the foil can be derived from the left picture in fig. 4.17. During the simulations, the hydrofoil operates with a Froude number of $F_n = 0.567$ by a given length of $c = 0.203m$.

In the first step the accuracy of the Fourier transformation shall be validated. For this purpose a non-coupled simulation with a geometrically modelled foil is performed with *FreSCo*$^+$. The grid used is illustrated in fig. 4.17 on the right and has approximately 50000 cells. A sketch of the obtained wave field is shown in fig. 4.18 on the left. The figure shows the volume fraction distribution after a simulation time of $t = 40s$. Due to the resolution of the grid the amplitudes of the second and third wave crest are slightly damped. A comparison is then made between the computed free-surface contour and the reconstructed free-surface shape after a Fourier transformation with 12 Fourier coefficients as depicted on the right hand side of fig. 4.18. Both curves are in a very good agreement and only slightly smaller wave crests are observed after the Fourier transformation. Hence,

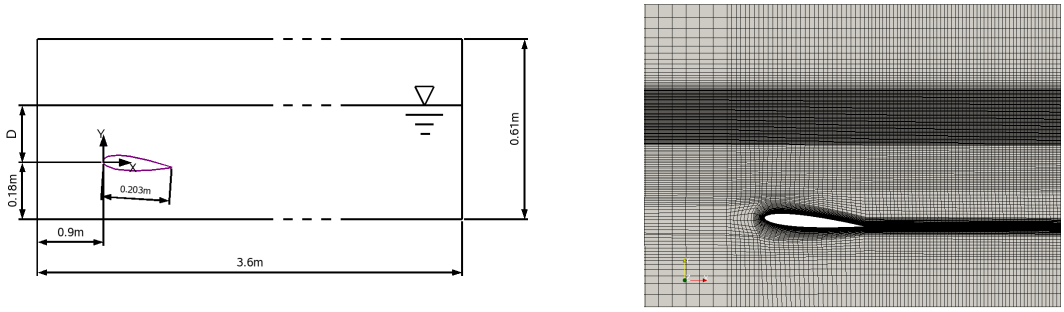

Figure 4.17: Left: Dimensions of the computational domain, which is used for the validation of the free surface transfer. The right figure shows a detail of the grid used for the simulations with the geometrically modelled foil.

the shape of the free surface can be transferred to *panMARE* with a sufficient accuracy to simulate equivalent floating conditions.

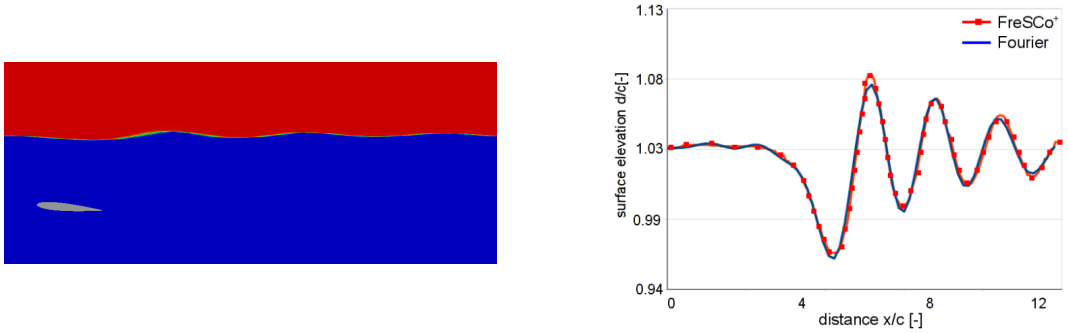

Figure 4.18: The left picture depicts the distribution of the volume fraction computed with *FreSCo*$^+$. The right figure shows a comparison between the *FreSCo*$^+$ result for the interface contour and the reconstructed contour after the Fourier transformation.

Afterwards, a coupled simulation is performed for the same case. Accordingly, the geometry of the hydrofoil is only modelled within *panMARE*, while inside the viscous-flow method a simple two-dimensional Cartesian grid of about 45.000 hexahedral cells is used. Since the test case refers to a steady state solution as outlined above, both the explicit and the implicit coupling algorithm result in the same converged solution. As the maximum time step size depends on the Courant number inside the viscous-flow solver and not on the requirements of the coupling method, the explicit algorithm is more efficient in this case. The left picture of fig. 4.19 shows the stationary wave pattern determined with a coupled simulation. As can be seen from the figure, the foil does not exist geometrically,

but the location of the foil can be identified by the resulting distribution of body forces. The cells in this region are coloured with the magnitude of the imposed force vector.

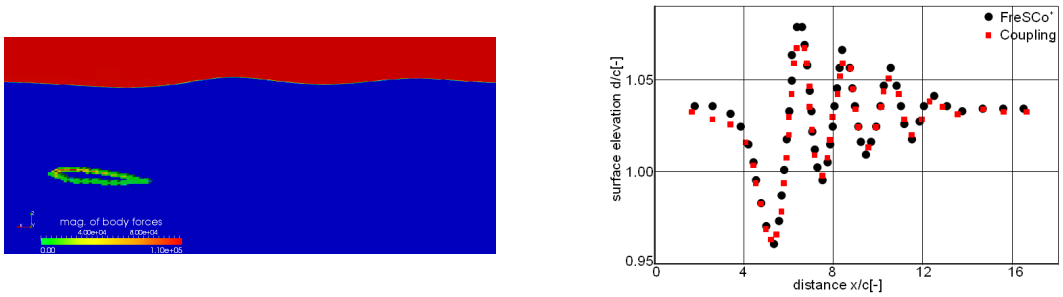

Figure 4.19: Results of the coupled simulation of the submerged hydrofoil. The left picture shows the hydrofoil modelled with body forces and the resulting distribution of the volume fraction. The right picture depicts the comparison of the surface elevation between a coupled and a geometric resolved calculation.

Finally, the surface elevation obtained from the coupled simulation shall be compared to the results of the geometry-resolving viscous-flow simulation. As depicted on the right hand side of fig. 4.19 the surface elevation predicted by the coupling algorithm - indicated by the red closed squares - is slightly lower than the results from the RANS computation. But overall the results demonstrate that the method is suitable for a qualitative assessment of the flow conditions, and that the simulations of a propeller interacting with the free surface shall be possible.

4.2.4 Operating propeller behind a moving ship

As a final verification case for the coupling procedure, an operating propeller behind a ship shall be simulated. The vessel refers to the KCS (Kriso Container Ship), investigated at the Gothenborg CFD workshop in 2010 [1]. The results of this analysis shall be then compared to simulations with a geometrically modelled propeller. The results using the geometrically resolved propeller refer to the computations carried out by Greve et. al [33]. Therein, a block-structured hexahedral grid with approximately 10 million cells is used. The simulations are performed with the software package CFX[1] by using the sliding-mesh technique. Compared to the simulations with a geometrically modelled propeller, a grid with a significantly reduced amount of cells (1.8 million cells) can be used for the coupled simulations. The computational grid for the *FreSCo*$^+$ part of the coupled simulation is shown in fig. 4.20 on the left hand side. The picture shows the refinements in the free

[1] www.cfx-germany.com

surface region and along the hull. The right picture depicts a detailed view of the grid at the aft ship. Here, the Cartesian grid, which is used in the propeller plane, is visible.

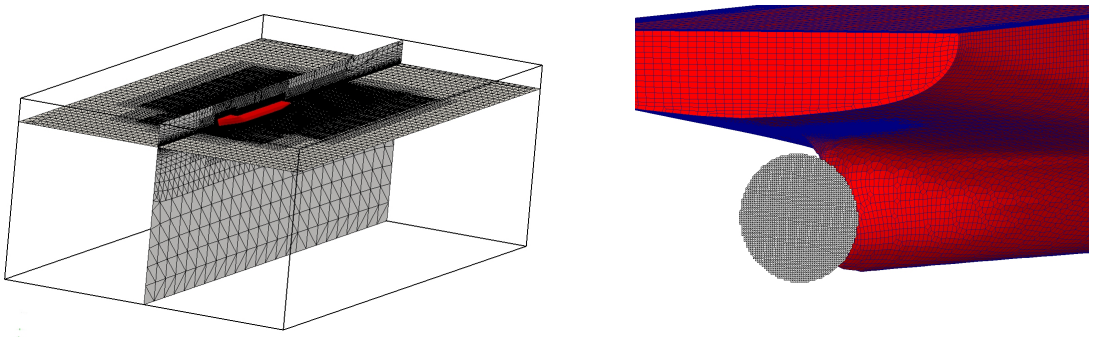

Figure 4.20: Computational grid used for the coupled simulations of the container vessel. The left figure shows the grid refinements in the free surface region and along the hull, while the right picture displays the Cartesian grid which is used in the propeller plane.

During the simulations the propeller operates at a constant working point to ensure a comparability to the case defined for the Gothenborg workshop. Hence, the number of revolutions is kept constant and no equilibrium between propeller thrust and the ship resistance is achieved. The ship speed is therefore simulated by applying a constant inflow velocity. An overview of the main computational parameters used for the coupled simulations can be found in table 4.2.

parameter	**value**
Froude number	0.26
number of revolutions	9.5rps
propeller diameter	0.25m
time-step size ($dt \cdot n$)	3°
number of time steps	720 (6 rotations)
coupling mode	explicit
number of cells (*FreSCo*$^+$)	1.8mio
number of panels (*panMARE*)	1920

Table 4.2: Parameters for the coupled simulations of the container vessel.

In the first step, a simulation without the operating propeller is performed with *FreSCo*$^+$ to obtain the nominal wake field, which is displayed in fig. 4.21. This nominal wake is

afterwards used as inflow condition for *panMARE* in the first time step of the coupled simulation. Typically, for a single-screw ship, the velocities in the upper part of the wake field and near the stern tube are reduced. The right picture of fig. 4.21 shows the wake field including the operating propeller. Due to the induced velocities and the interaction velocities caused by the hull and the propeller, larger velocities are obtained in the upper part compared to the nominal wake field. Additionally, the circumferential velocity components generated by the propeller lead to visible asymmetric contours of the wake field.

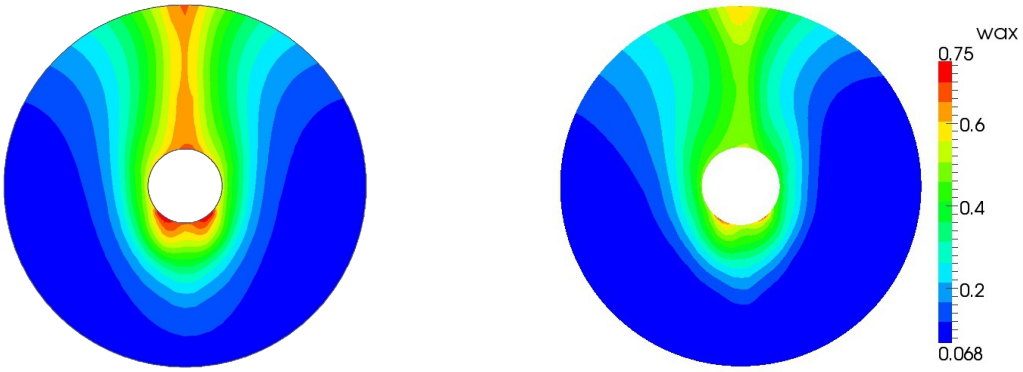

Figure 4.21: Comparison of nominal (left) and effective (right) wake fields for the container vessel.

Overall, the smaller axial velocities in the wake decrease the advance coefficient compared to open water simulations. Furthermore, a moving blade in the wake faces different working conditions during one rotation. In the upper positions the smaller axial velocities in combination with the larger tangential velocities decrease the local advance coefficient, which increase the blade angle of attack as displayed in fig. 2.4. In this region of the wake, the respective blade produces a larger amount of lift and therefore thrust. This results in remarkable blade-thrust variations during one revolution as illustrated in fig. 4.22. A comparison is made between the coupling method and simulations obtained by Greve et. al. [33]. The results for the coupled simulation are plotted with the red curves, while the CFX results are displayed in black. For both cases the thrust for one blade (solid lines) as well as the propeller thrust (dashed lines) are depicted. The blade-thrust variations due to the wake are visible in both cases. But overall, larger fluctuations are obtained for the coupling method. This deviation may be attributed to the fact that the inflow velocity field in *panMARE* is updated only once per time step. Additionally, the direct simulation of the linear equation system in *panMARE* and the lack of the consideration of viscous effects causes a more instantaneous reaction on disturbances.

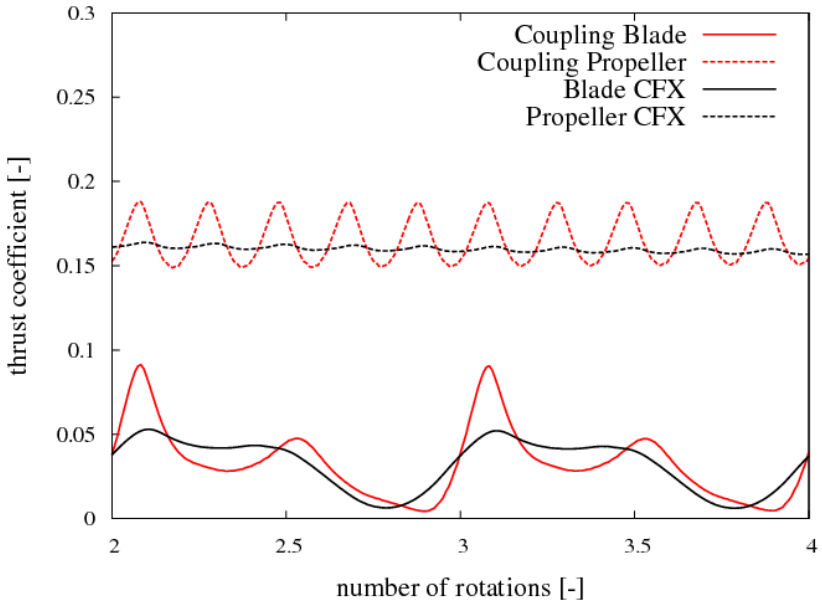

Figure 4.22: Comparison of propeller and blade thrust coefficients between a coupled and a pure RANS simulations.

5 Study of the free surface influence on the open water characteristics

The objective of this chapter is a numerical investigation of the free surface influence on the flow around an open-water propeller. As indicated in section 2.2, a propeller in the vicinity of the free surface might start ventilating, which causes large load fluctuations. In such conditions, experimental investigations for example in Koushan [44] reveal thrust losses up to 100% for a fully ventilated propeller compared to a deeply submerged one. Furthermore, large thrust fluctuations can occur due to the unsteady character of ventilation. Henceforth, ventilation might be one of the most critical aspects for the investigation of ship propulsion in waves. The numerical results presented in this chapter are obtained with the viscous-flow solver *FreSCo*$^+$ and the coupling procedure (c.f. chapter 4). The aim of the geometrically resolving viscous-flow calculations is to analyse to what extent a RANS method is able to predict ventilation and to study the dependency of ventilation on the advance coefficient and the immersion ratio. The obtained results are afterwards validated with measurements. However, a large computational effort is expected for these simulations and so the coupling procedure is also used for the investigation of propeller ventilation. The main purpose of this effort is to analyse, whether the coupling approach is able to compute equivalent thrust losses and amounts of ventilation, compared to simulations with a geometrically resolved propeller.

The used propeller geometry refers to the one investigated during the research project *PropSeas* (c.f. section 4.2.1). The corresponding experimental data is determined by MARINTEK (Norway) and published in Kozlowska et. al. [50]. The configuration used in the experiments is shown in fig. 5.1 on the left hand side. Analogues to the original full-scale configuration, where the propeller is mounted on a pod housing, the open water propeller is investigated in pulling mode. Thus, the propeller shaft is located in the wake of the propeller. The picture on the right illustrates the geometry used in the simulations with *FreSCo*$^+$. In the experiments and during the calculations, the number of revolutions of the propeller is set to $n = 18\,rps$. Accordingly, surface-tension influences are negligible due to a Weber number above the critical value of $W_e = 180$. Different advance coefficients are realised by a variation of the inflow velocity. A summary of the main propeller parameters can be taken from table 5.1.

Figure 5.1: Geometry of the investigated propeller. The experimental set up is shown on the left, the picture on the right displays the used geometry for the simulations with a geometrically modelled propeller.

The Reynolds number based on the chord length at $r/R = 0.7$ is in the regime of $R_e = 0.5 \cdot 10^6$. In the next section, the set up used for the simulations is described in more detail. Afterwards an overview on the computed results including a comparison to the measurements is given. At the end of this chapter an investigation on scale effects for ventilating propellers is presented.

parameter	**value**
number of blades	4
number of revolutions	18 rps
propeller diameter	0.2 m
hub diameter	0.06 m
propeller pitch (P/D)	1.2

Table 5.1: Main parameters of the investigated propeller.

5.1 Description of the computational set up

During the viscous-flow simulations with *FreSCo*$^+$, the propeller is geometrically resolved and modelled in a cylindrical domain as illustrated in fig. 5.2 on the left. Periodic boundary conditions can not be used for the present simulations due to the expected unsteady behaviour of the propeller and the non-uniform flow conditions at the single blades. Thus, all four blades of the propeller have to be modelled. To account for the rotations of the propeller, the whole domain is moving with the propeller. The inflow

conditions, including the inflow velocity and the position of the free surface are specified at the blue-coloured region of the figure. These values and the vector of the gravity force are defined in an earth-fixed coordinate system. Thereby, the position of the free surface remains constant, while the propeller is rotating. The outflow boundary marked

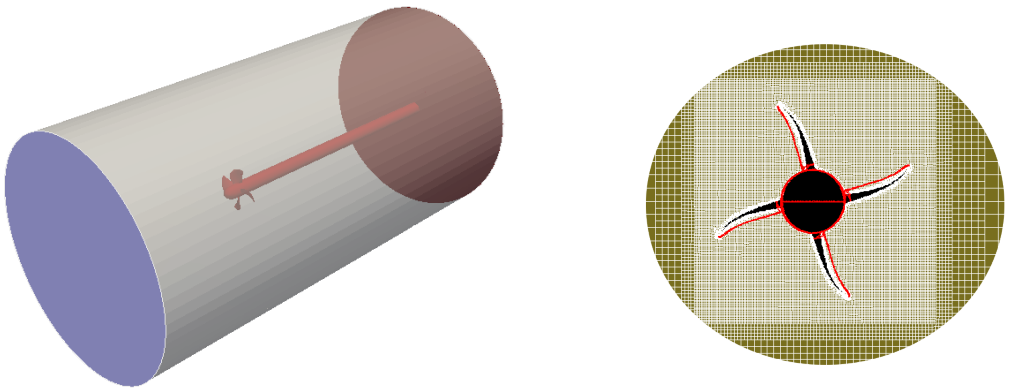

Figure 5.2: Sketch of the computational domain (left) and illustration of the grid in the propeller plane (right) for the simulations with a geometrically resolved propeller.

in red is idealised as pressure boundary, and a hydrostatic pressure distribution is set. The outer boundary is modelled as a slip wall. There, the normal velocity component is set to zero, but the tangential velocity is non-zero. The whole domain is not drawn to scale in the figure. In original, the domain has a diameter and a length of 10D, whereof approximately 4D are located in front of the propeller. Due to the rotation of the grid, the position of the free surface relative to the grid varies during the different time steps. Thus, for an adequate resolution of the expected free-surface deformation, cell-refinements are necessary in the whole range around the propeller, as displayed in fig. 5.2 on the right. The resulting computational grid has a number of approximately 2.9 million cells.

For the simulations with the coupling procedure, a stationary and Cartesian grid can be used inside the viscous-flow solver, as the propeller rotations are applied by a rotating set of forces. A grid similar to the one in section 4.2.1 with additional refinements in the free surface region is used as depicted in fig. 5.3 on the left. The picture shows that most of the cells are located around the propeller. The grid is relatively coarse and has larger cells in the free-surface area compared to the grid used for the simulations with a geometrically resolved propeller. Overall, the grid consists of approximately 270000 cells. Thus, a significantly smaller grid is used as in the RANS computations and remarkable smaller simulation times are expected. With respect to simulations of a ship-propeller configuration such a grid size might be viable for practical applications. Henceforth, the additional aim of the coupled simulations is to estimate the feasibility of computations

with such a coarse grid. The right hand side of fig. 5.3 displays the configuration used in *panMARE* during the coupled simulations. In addition to the 544 panels per blade, 1600 panels are used to model the free surface.

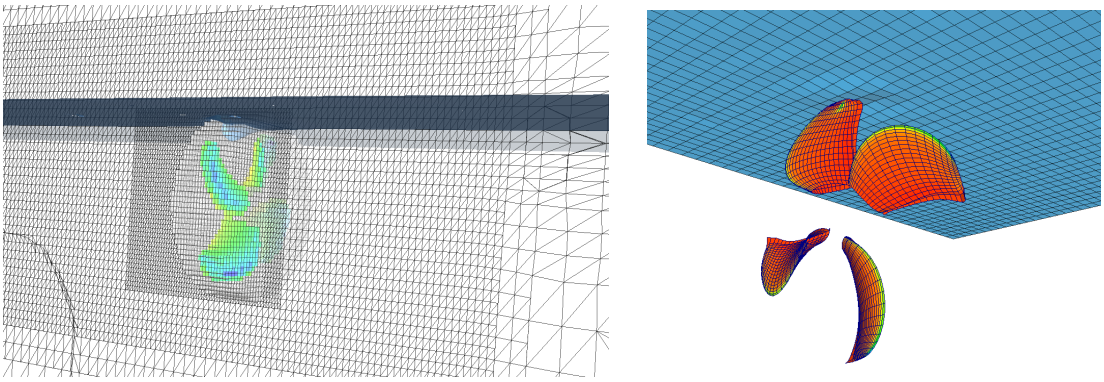

Figure 5.3: Computational grids used for the coupled simulations. The *FreSCo*$^+$ grid is depicted on the left, while the right picture displays the configuration used in *panMARE*.

Before investigating the influence of the free surface on the propeller, the propeller is investigated in deeply submerged conditions with *FreSCo*$^+$ for validation purposes. Analogues to the validation of the coupling procedure (cf. section 4.2.1), no ventilation occurs in this case and constant thrust and torque values are obtained for the single advance coefficients. For these computations a simpler grid with approximately 800000 cells is used, as no refinement for the free surface is necessary. Simulations are performed for both, laminar and fully turbulent flow conditions. In general, the flow is expected to be fully turbulent as the Reynolds number, based upon the chord length at 70% of the radius is approximately $R_e = 0.5 \cdot 10^6$. For the turbulent case, a $k - \omega$ turbulence model in conjunction with a wall-function approach is used. The resulting y^+-values are in the regime $20 \leq y^+ \leq 60$. A comparison of the computed open water characteristics to the experimental values can be found in fig. 5.4. Overall, a good agreement is observed between the turbulent *FreSCo*$^+$ results displayed with the dark green curves and the experimental results (red curves). Only the values for the open water efficiency are slightly under-predicted by *FreSCo*$^+$ at the larger advance coefficients due to the increased torque values. The laminar values are approximately 8% larger (light green curves).

As a second preliminary study, the influence of turbulence on propeller ventilation is studied. The aim of this effort is to analyse, whether laminar simulations are sufficient to capture the relevant flow features. Compared to the turbulent case, the computational effort for laminar simulations is smaller due to the reduced number of transport equations and the lower requirements on the grid resolution in the wall regions. The laminar and turbulent results are compared in terms of the free surface shape and the computed thrust

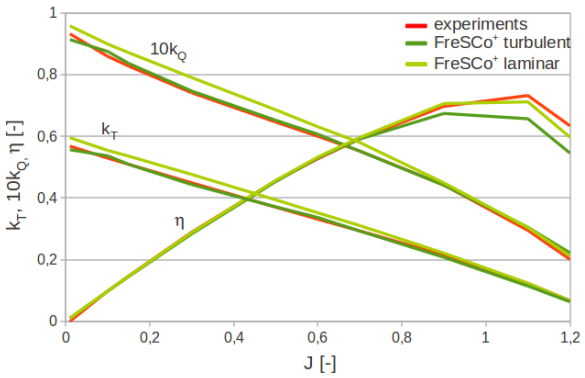

Figure 5.4: Open water diagram for the deeply submerged propeller showing the comparison between the computed *FreSCo*$^+$ results and the experimental values.

losses for a single blade. Here, the thrust loss is defined as ratio between the thrust generated by a ventilating propeller blade and the corresponding value of a deeply submerged one. Figure 5.5 reveals only small differences between the laminar and the turbulent case, which allows the performance of laminar simulations to study the interaction of the propeller with the free surface. Then, the number of cells can be reduced to 2.7 million.

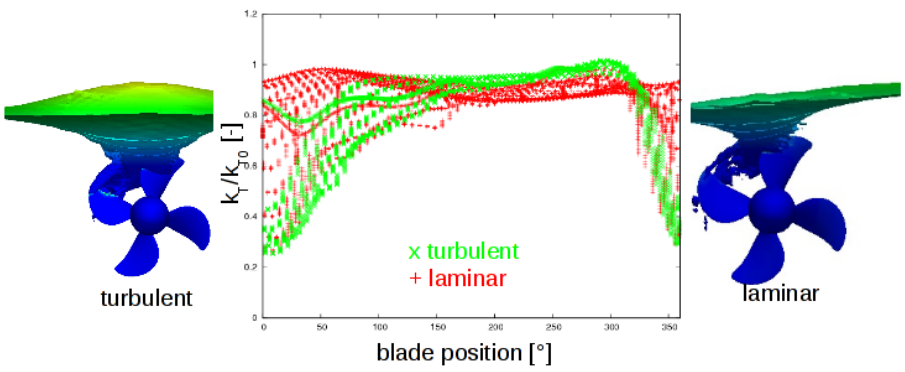

Figure 5.5: Comparison of laminar and turbulent results for a partly ventilated propeller ($J = 0.01$, $H/R = 1.5$).

In spite of this simplification, the grid resolution in the free-surface region requires a time-step size of approximately $dt \cdot n = 0.45°$ to achieve Courant numbers in the magnitude of $Co = 0.5$. Thus, the computational effort also for the laminar calculations is very large. The simulation of one propeller rotation requires approximately 800-1000 time steps and a computational time of almost one week in case of a parallelization of the computational domain on 16 processors. Due to the coarse grid, the computational times for the coupled

simulations are much smaller and one revolution of the propeller can be computed in less than one day. Moreover, larger time steps can be used in the coupled simulations due to the larger cells in the free surface area. The selected time-step size refers to $dt \cdot n = 3°$, which results in only 120 time steps for one rotation of the propeller.

5.2 Influence of the advance coefficient

Investigations from Koushan [44] and Kozlowska [49] reveal a strong influence of the propeller loading on the amount of ventilation. In this study, it shall be investigated whether *FreSCo*$^+$ is able to predict this correlation as well. During these computations the immersion ratio is assigned to a constant value of $H/R = 1.5$, while the inflow velocity is varied to achieve the different advance coefficients. The investigated advance coefficients and the corresponding inflow velocities can be taken from table 5.2. From the experiments, the propeller is expected to ventilate for the smaller advance coefficients, while no ventilation will occur for the larger ones.

advance coefficient [-]	**inflow velocity [$\frac{\mathbf{m}}{\mathbf{s}}$]**
0.01	0.036
0.15	0.54
0.3	1.08
0.6	2.16
0.9	3.24
1.2	4.32

Table 5.2: Investigated advance coefficients and corresponding inflow velocities.

A comparison of the predicted free surface shape above the propeller is displayed in fig. 5.6 for the three smallest investigated advance coefficients. Therein, a contour plot for the nominal air-water interface $(c = 0.5)$ illustrates the predicted shape. The propeller itself is coloured with the resulting air-volume fraction at the propeller surface. The result for the smallest advance coefficient $(J = 0.01)$ is displayed in the leftmost picture, while the right picture portrays an equivalent instant in time for $J = 0.3$. All three pictures are obtained after the first couple of rotations. Partial ventilation of the propeller blades is visible for the two smallest advance coefficients. Here, the free surface is sucked down by the propeller, which leads to surface piercing and partly-ventilated blades in the upper positions. On the way down, the blade looses its contact to the free surface and fully wetted blades are visible after passing the lowest position in all cases. The influence of the propeller on the free surface becomes smaller, if the advance coefficient is increased

and only a small deformation of the free surface is visible in case of $J = 0.3$. Thus, a clear dependency of the advance coefficient and thereby of the propeller loading, on the amount of ventilation can be seen.

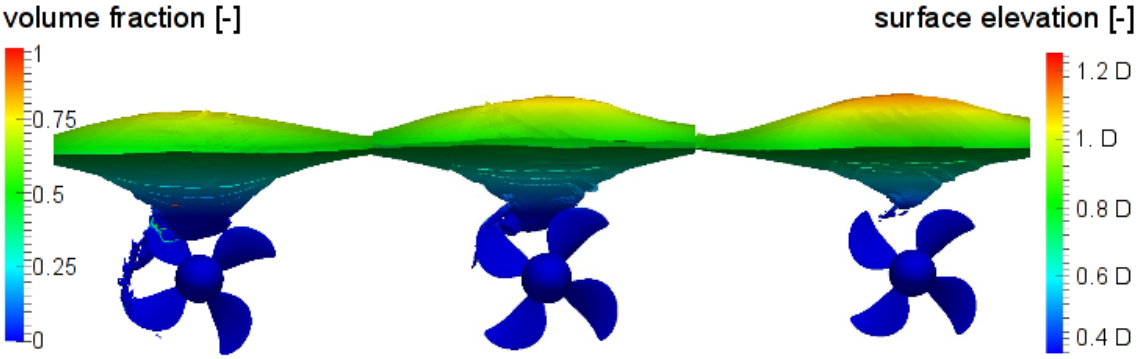

Figure 5.6: Sketches of the free surface contour for different advance coefficients and $H/R = 1.5$ ($J = 0.01$ (left), $J = 0.15$ (middle), $J = 0.3$ (right)).

Furthermore, the occurrence of ventilation is also visible in the predicted thrust values. Overall, the thrust generated by a ventilating propeller is smaller than the corresponding one of a deeply submerged propeller and the obtained values are not constant over time. In the following analysis the thrust losses due to ventilation are displayed in terms of the blade thrust ratio k_T/k_{T0} over the blade position. Therein, k_T and k_{T_0} are defined as

$$k_T = \frac{T_{blade}}{\rho n^2 D^4} \quad \text{and} \quad k_{T_0} = \frac{T_{0\,blade}}{\rho n^2 D^4}\,. \tag{5.1}$$

The index $blade$ indicates the thrust calculated for a single blade, while the index 0 refers to the corresponding value computed for one blade of the deeply submerged propeller. The definition for the blade position refers to 0° in the topmost position and to 180° in the lowest position.

Figure 5.7 displays the computed blade thrust ratio for the advance coefficients analysed in fig. 5.6. In the figure, red dots display the results for $J = 0.01$. Here, thrust losses up to 80% can be found near the upright position, while nearly no thrust losses are obtained in the lowest blade positions. The thrust losses near the topmost position become smaller when the advance ratio is increased to $J = 0.15$ (black dots) and to $J = 0.3$. Hence, these results illustrate a direct correlation between the amount of ventilation and the computed thrust losses. An analogues tendency is also visible within a single calculation as illustrated in fig. 5.8 for an advance coefficient of $J = 0.01$. In the figure, the thrust loss for the blade marked with a red circle is plotted over the blade position. In addition,

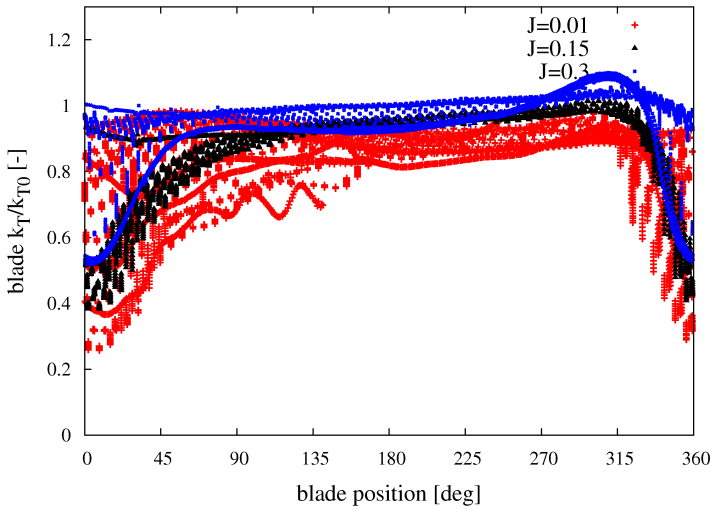

Figure 5.7: Computed blade thrust ratio for the three smallest advance coefficients at $H/R = 1.5$.

the corresponding volume fraction on the propeller blades is shown for two positions. Near the topmost position more than half of the blade's surface is ventilated. On the way down the blades looses the contact to the free surface and the ventilated parts of the blade become wetted again. Thus again, the picture reveals the direct correlation between the thrust loss and the amount of ventilation on the respective blade.

A similar correlation can be derived from the time series of the computed thrust in combination with corresponding pictures of the free-surface shape. As illustrated in fig. 5.9 a time interval with more pronounced thrust losses adheres to larger amounts of ventilation, while a non-ventilating propeller corresponds to almost constant thrust values. In addition to this, the figure illustrates the highly unsteady behaviour of ventilation. Next to variations during one revolution, ventilation and non-ventilation phases can occur during one simulation. This is also shown in Kozlowska [50], where different ventilation forms are observed during a single experiment.

5.3 Influence of the immersion ratio

In addition to the previous subsection, a clear correlation is expected between the static immersion ratio H/R and the amount of ventilation. To investigate this, three different immersion ratios between $H/R = 1.5$ and $H/R = 0$ are simulated. Figure 5.10 illustrates

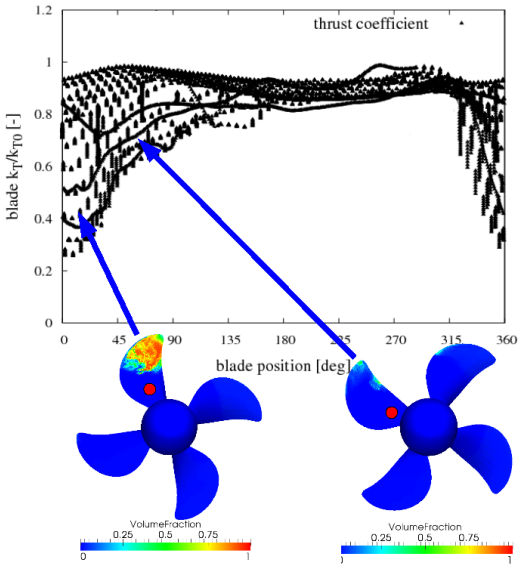

Figure 5.8: Correlation of the amount of ventilation on the blade surface and the predicted thrust losses.

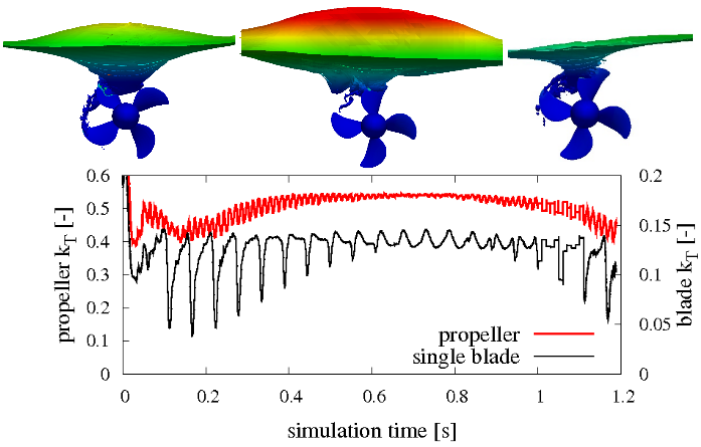

Figure 5.9: Time series of the computed thrust coefficient for a single blade and the propeller for $J = 0.01$ and $H/R = 1.5$. The upper pictures display the corresponding free-surface shape for three time instants.

the definition of the immersion ratio, where the propeller draught is defined as distance between the free surface and the centre of the propeller shaft. Thus, in case of $H/R = 1$ the blade tips touch the free surface in the initial stage, while in case of the smallest immersion ratio $(H/R = 0)$ half of the propeller is out of the water in static conditions.

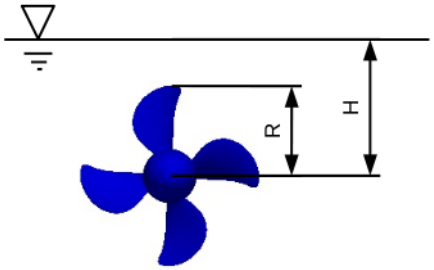

Figure 5.10: Definition of the immersion ratio.

Sketches of the free-surface contour obtained for a constant advance coefficient of $J = 0.3$ and the different immersion ratios are displayed in fig. 5.11. Again, the propeller blades are coloured with the volume fraction, while the free surface is coloured with the resulting elevation. For comparison, the previously investigated immersion ratio of $H/R = 1.5$ is shown on the left. Only a small influence of the propeller on the free surface shape can be found in this case and all blades are fully wetted. Due to the reduced distance between the free surface and the propeller tips, surface-piercing blades in the upper positions and partly ventilated blades in the lower positions can be observed, if the immersion ratio is reduced to $H/R = 1$. But analogues to the cases investigated beforehand, the blades become again wetted after passing the lowest position. Due to the static immersion of the propeller in case of $H/R = 0$ the blades are completely out of water in the upper positions and even the blades near the lowest position are not fully wetted.

The respective blade-thrust ratios along the angular position for these three cases can be found in fig. 5.12. Again, a clear correlation can be found between the amount of ventilation on a blade and the resulting thrust loss. The red dots show the results for the smallest immersion ratio. In this case no thrust is generated, if the respective blade comes out of water, while near the lowest position a thrust recovery of up to 60% can be found due to the still ventilated blades. In case of $H/R = 1$ (black dots), thrust losses of up to 80% compared to the deeply submerged propeller are obtained near the topmost position. Here, the nominal blade thrust is generated only in a small range behind the lowest position where the blade looses contact to the free surface and becomes freshly wetted. The largest load variations are observed in this case. The blue dots show again

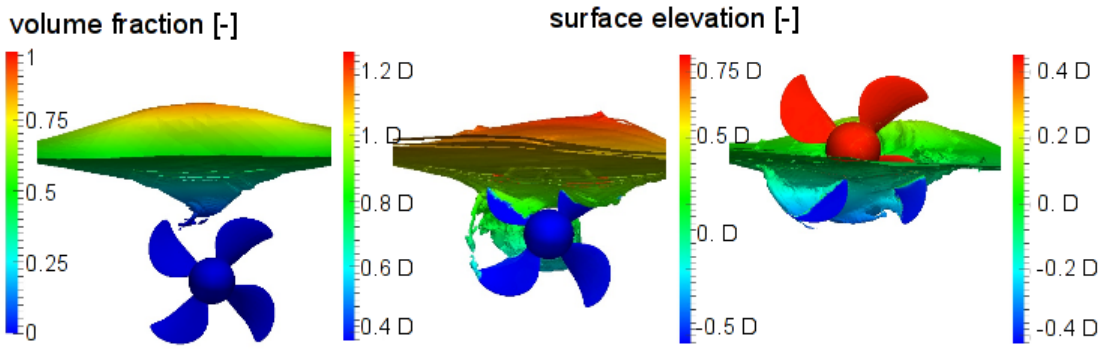

Figure 5.11: Pictures of the free-surface contour for different immersion ratios and $J = 0.3$ ($H/R = 1.5$ (left), $H/R = 1$ (middle), $H/R = 0$ (right)).

the results for the largest immersion ratio, where nearly no ventilation of the blades is observed.

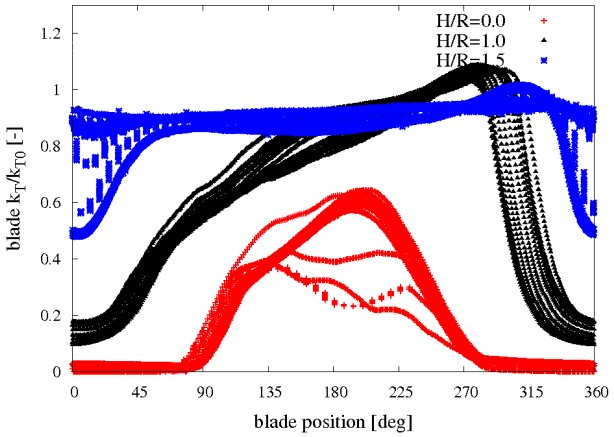

Figure 5.12: Influence of the immersion ratio on the thrust losses due to ventilation for $J = 0.3$ and the three immersion ratios.

5.4 Comparison to experiments

The previous subsections investigate the influence of the advance coefficient and the immersion ratio on the occurrence of ventilation. To validate these results, comparison is

made to towing tank experiments performed by MARINTEK under the aegis of *PropSeas*. Therein, the propeller is mounted on an open-water test rig as shown in fig. 5.1. Flow visualisation is obtained from two high-speed cameras, one being located above the free surface and one below. The forces and moments on the propeller as well as on a single blade are measured. Thus, the single blade loads can also be compared to the computed results. More details on the experiments and on the used sensors can be found in Kozlowska [50] and Koushan [48].

The left picture of fig. 5.13 depicts the comparison of the blade-thrust losses for $J = 0.15$ and $H/R = 1.5$. The results of the simulations are displayed in green, while the measured values are represented by the red dots. Similar to the results presented before, the thrust losses are displayed in dependency of the blade position. As the computational effort for the computations is very large, a significantly longer observation time is feasible in the experiments and consequently, more measured data points are available. The magnitude between minimum and maximum thrust is almost equal in the experiments and the simulations. But a stronger variation over one rotation is observed in the computations with nearly no differences between the single rotations. In the experiments the thrust losses are almost constant over one rotation, but different levels of thrust loss can be found depending on the time of the experiment. During ventilation periods, the whole propeller is covered with air (fig. 5.13, right) in the experiments, while the blade looses contact to the free surface behind the lowest position in the simulations (central picture of fig. 5.6).

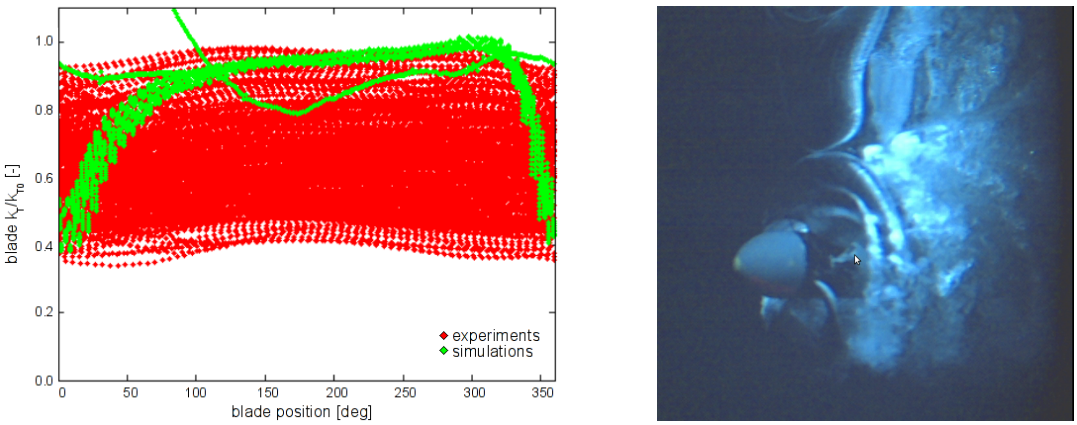

Figure 5.13: Comparison between measurements (red) and simulations (green) for an advance coefficient of $J = 0.15$ and an immersion ratio of $H/R = 1.5$ (left) as well as a photo from the experiments for the same case (right).

Analogues findings can be derived from fig. 5.14. On the left hand side of the figure the computed thrust losses are compared to the experimental values for $J = 0.3$ and

$H/R = 1.5$. The picture depicts that different levels of thrust loss and therefore different forms of ventilation are obtained in the experiment, while only small variations are visible within one rotation. The computed results are in the upper regime of the measured values, where only small amounts of ventilation can be observed. The corresponding time series of the experiment can be found in the right picture. Here, it becomes clear that in the beginning of the experiment the flow changes very rapidly between ventilation phases and non-ventilating phases, while stable ventilation occurs only after a longer time of the experiment. The larger thrust values observed in the first part of the experiment are in the same order of magnitude as the results of the simulation. Thus, it is possible that the results of the computations show only one possibility for the behaviour of the propeller, and longer simulation times would be necessary to predict a fully ventilating propeller.

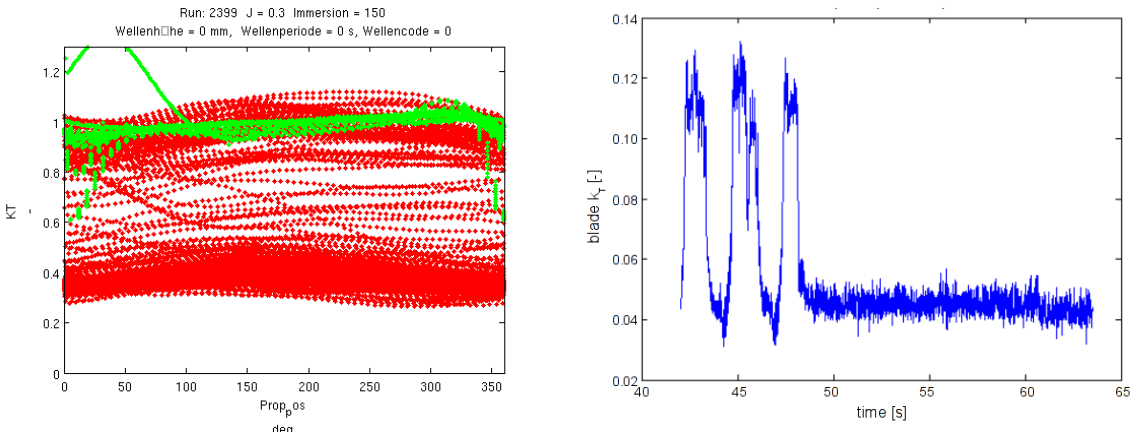

Figure 5.14: Comparison between measurements (red) and simulations (green) for $J = 0.3$ and $H/R = 1.5$ (left). The right picture displays the measured time series of the blade-thrust coefficient.

As a concluding example, the computed results for $J = 0.3$ and $H/R = 0$ shall be compared to the corresponding measurements. The respective result is displayed in fig. 5.15. In this case, the propeller is out of water for half a rotation. Then, the blade does not generate any thrust and a good agreement between the measured values and the computed results can be found. But if the blade moves down, the increase in the thrust values is larger in the simulations than in the experiments. Near the lowest position the computed thrust losses are approximately twice as large as the measured ones. These larger thrust losses in the experiments are again a result of the fully ventilated blade in this stage of the rotation. In contrast to this, the blade in the lowest position is partly wetted in the simulations as can be seen in fig. 5.11 on the right.

In conclusion, the flow visualisations show a substantially larger amount of air in the water during the measurements than in the computations. In agreement to this, the measured

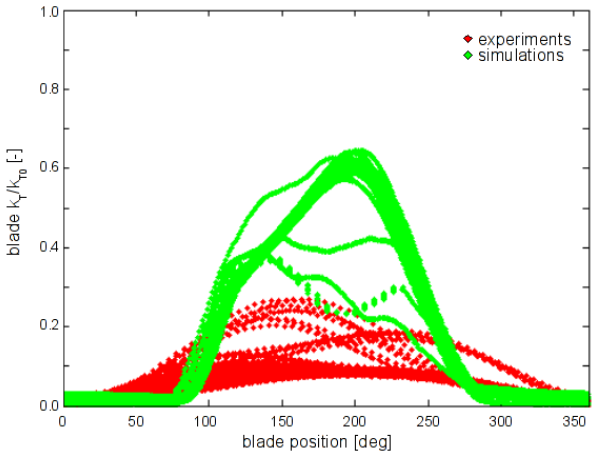

Figure 5.15: Comparison between measurements (red) and simulations (green) for an advance coefficient of $J = 0.3$ and an immersion ratio of $H/R = 0$.

thrust losses are also larger than the computed ones. In the experiments the whole propeller is surrounded by air when the propeller ventilates, while the blade looses contact to the free surface before it reaches the lowest position in the computations. These findings are in agreement with the computational results of Califano et.al in [12], where also less amounts of ventilation are observed after the blade passes the lowest position. The results reveal that a rational comparison between simulation and experiments is difficult. Due to the large computational effort it is not possible to simulate more than a few (10-15) revolutions, while in some experiments stable ventilation starts after a significantly higher number of revolutions. Henceforth, only one possible ventilation form can be predicted in the simulations, while different thrust levels are observed in the experiments. Furthermore, equivalent initial conditions can not be realised. In the simulations the propeller starts with the full number of revolutions and the flow is initialised with the nominal inflow velocity, while both values are increased up to 100% in the initial phase of the experiment. Additionally, it is possible that an amount of liquefied gas is available in the tank water, which is not existing in the simulations. Despite to the observed discrepancies, the computed results are encouraging as the main characteristics are identified properly. This includes the prediction of the correct dependency of ventilation on the propeller loading and the immersion ratio and the determination of the load variations between a ventilated and a non-ventilated blade.

5.5 Evaluation of the capabilities of the coupling procedure

The large computational effort of RANS-based simulations with a geometrically modelled propeller strongly restricts the possible field of applications. The aim of this section is to investigate, whether the coupling procedure can be used to predict the main effects on ventilating propellers as well. To analyse this, simulations analogues to the ones in section 5.2 and 5.3 are performed. The obtained results are verified with the results presented beforehand with a geometrically modelled propeller.

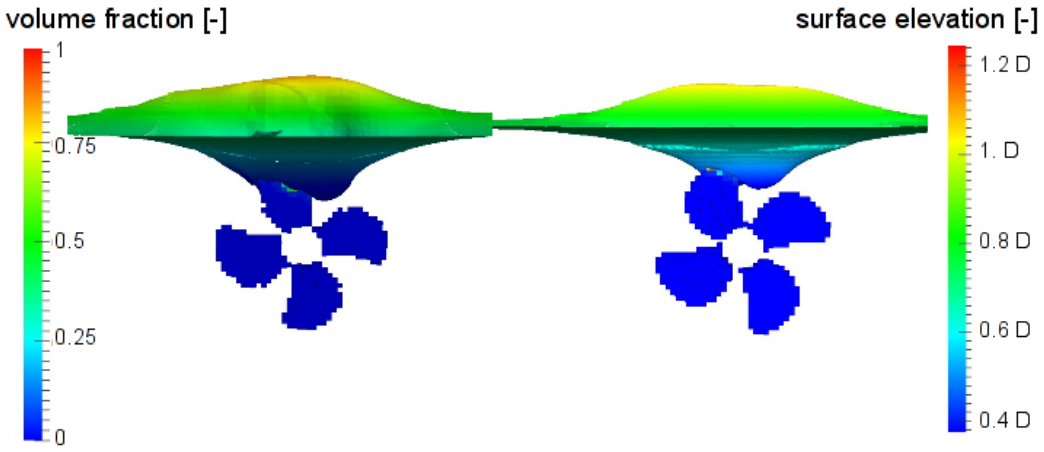

Figure 5.16: Investigation of propeller ventilation with the coupling procedure at $H/R = 1.5$ (Left: $J = 0.15$, Right: $J = 0.3$).

In fig. 5.16 it becomes obvious, that also the body-force propeller interacts with the free surface. Both figures are obtained from simulations with an immersion ratio of $H/R = 1.5$. The advance coefficients are assigned to $J = 0.15$ (left) and $J = 0.3$ (right). Analogues to fig. 5.6 the blades in the upper positions become surface piercing, while the blade looses the contact to the free surface in the lower positions. Similar to the results obtained with a geometrically resolved propeller, the coupling procedure predicts larger amounts of ventilation in case of the smaller advance coefficients. Figure 5.17 compares the thrust losses predicted by the coupling procedure to the ones computed with a geometrically resolved propeller for the parameter set of fig. 5.16. The results predicted by the coupling method are displayed with black stars, while the results of the geometrically modelled propeller are labelled with "RANS" and marked with red dots. Although slightly larger thrust losses are predicted by the coupling algorithm, the overall agreement is very good. The deviation in the thrust losses can be attributed to the applied

split technique in *panMARE*. This method sets the dipole strength of the panels above the free surface to zero, which omits the production of thrust in air. Due to numerical stability problems, the panels directly below the free surface must also have a dipole strength of zero. Thus, slightly larger parts of the blade do not generate any thrust in case of the coupling approach.

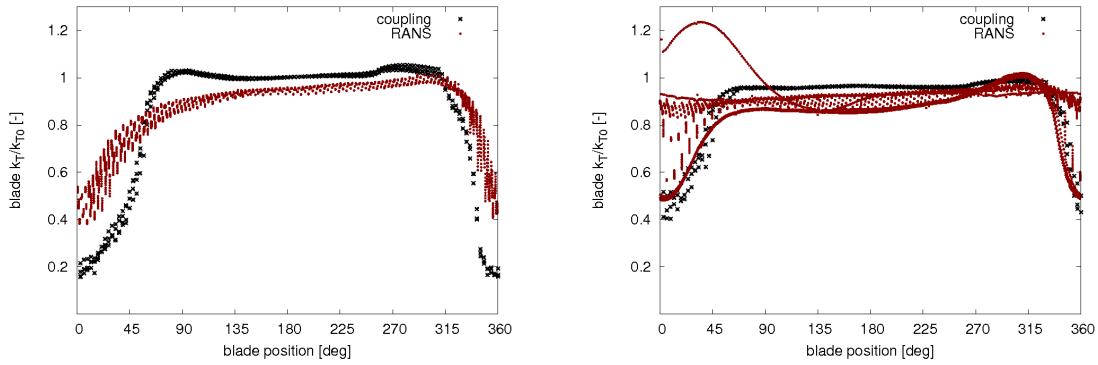

Figure 5.17: Comparison of the computed thrust losses between the coupling procedure and *FreSCo*$^+$ simulations with a geometrically resolved propeller for $H/R = 1.5$ ($J = 0.15$ (left) and $J = 0.3$ (right)).

The coupling procedure is afterwards used to study the dependency of ventilation on the immersion ratio as well. The left picture in fig. 5.18 displays a result of a simulation with $H/R = 1$, while the right picture is obtained with an immersion ratio of $H/R = 0$. In both cases the advance coefficient is set to $J = 0.3$. A comparison with the corresponding images in fig. 5.11 depicts a fair agreement in the shape of the free surface. Only in the case of the smaller immersion ratio, the figure reveals some discrepancies in the lower blade positions. Here, the coupling procedure predicts fully wetted blades, while the blades of the geometrically resolved propeller are partly ventilated. A possible reason for this deviation might be the Fourier transformation, which smooths the shape of the free surface. Moreover, the blades in the upper positions are not visible in the viscous-flow solver as the forces in this part are zero. Figure 5.19 compares the corresponding thrust losses for these two cases. A very good agreement is observed for $H/R = 1$ (left picture) with only minor differences around a blade angle of 120°. In contrast, the results for $H/R = 0$ reveal a larger deviation. Here, the coupling procedure predicts larger thrust values in the lower blade positions, which corresponds to the flow visualisations in fig. 5.18 and fig. 5.11. Still, the results for the coupling procedure are promising and allow for an application of the present method for investigations of propeller ventilation.

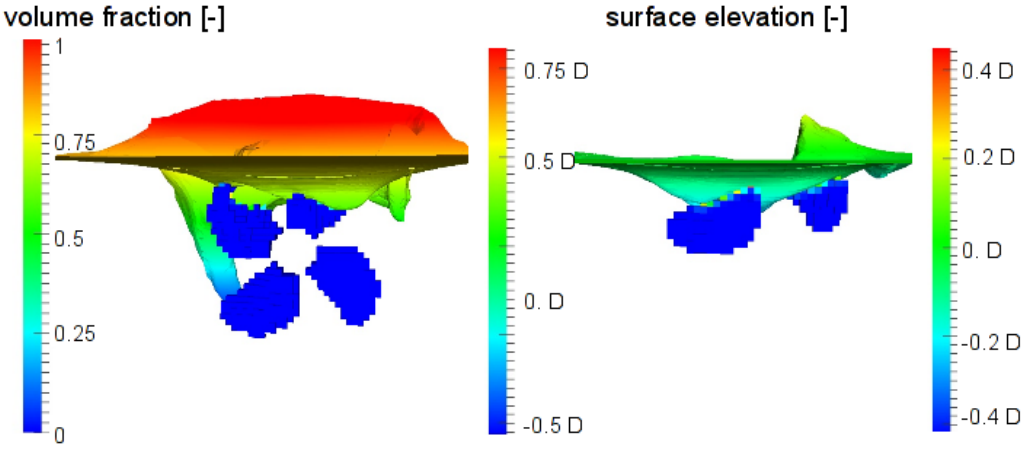

Figure 5.18: Coupled simulation of propeller ventilation at $J = 0.3$ (Left: $H/R = 1$, Right: $H/R = 0$).

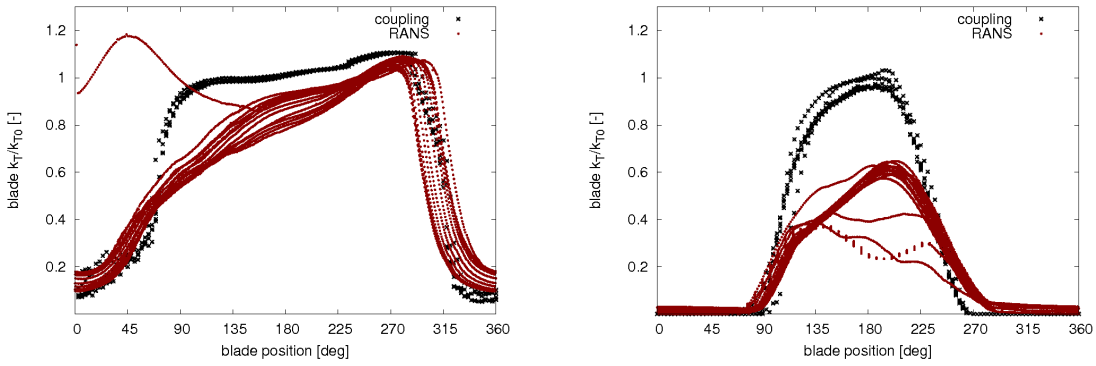

Figure 5.19: Comparison of the computed thrust losses between the coupling procedure and *FreSCo*$^+$ simulations with a geometrically resolved propeller for $J = 0.3$ ($H/R = 1$ (left) and $H/R = 0$ (right)).

5.6 Investigation on the Reynolds number influence

Nowadays a model test is still the most common method for propeller-flow investigations, despite the increasing capacities of numerical methods. For the prediction of the respective full-scale values various procedures exist. An overview on common procedures is given by Müller in [61]. Within, an approach based on viscous numerical simulations is presented as well. However, all of these methods are restricted to deeply submerged propellers and only very little knowledge is available on scale effects during ventilation events, due to the lack of sufficient simulation tools and full-scale measurements. To estimate whether the effect of the scale is important for the magnitude of the thrust losses caused by ventilation, this effect shall be investigated with *FreSCo*$^+$ in this section. Due to the larger Reynolds number in full-scale and the resulting requirements on the cell size in near-wall regions, the computational times are expected to be significantly larger compared to model scale. Thus, only a small number of simulations is possible. To reduce the computational effort, some aspects shall be investigated beforehand with the help of two simple geometries.

5.6.1 Scale effects on surface-piercing bodies

The aim of this section is to study possible scale effects on two surface-piercing bodies and to validate the capabilities of *FreSCo*$^+$ for such simulations. The investigated geometries refer to a NACA0012 hydrofoil and a circular cylinder as displayed in fig. 5.20. The

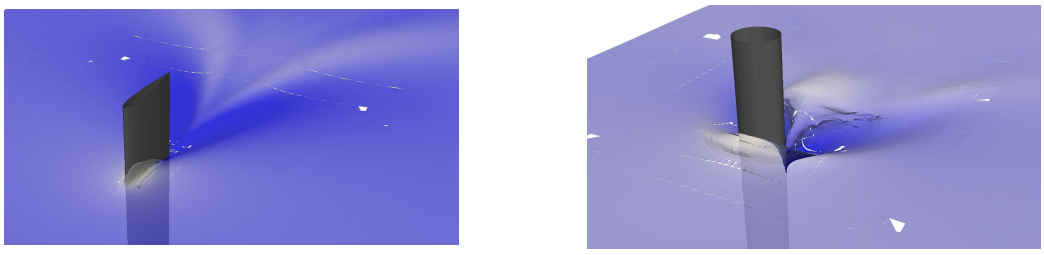

Figure 5.20: Geometry of the surface-piercing foil (NACA0012, left) and the circular cylinder (right).

simulations are performed for three Froude numbers and four different scale factors to account for a large range of Reynolds numbers. A summary of the selected simulation parameters can be found in table 5.3. The geometrical dimensions in the table are given for a scale factor of 1. The resulting Reynolds numbers vary between $R_e = 5 \cdot 10^4$ and $R_e = 10^8$. Thus, the range of Reynolds numbers is quite large and covers laminar as well as fully turbulent flows and the typical values for full and model scale propellers. The selected Froude numbers are quite high compared to typical values for a ship, but

profile		cylinder	
parameter	**value**	**parameter**	**value**
chord length	0.203m	diameter	0.4m
height	0.5m	height	4m
draught	0.3m	draught	3m
Froude number	0.5,1.0,1.5	Froude number	0.5,1.0,1.5
scale factors	0.1,1,10,100	scale factors	0.1,1,10,100

Table 5.3: Overview of the main parameters for the two investigated geometries.

an immersing propeller blade or a surface piercing strut of a podded propeller has Froude numbers in this range. Furthermore, Califano [11] expects a dependency of the Froude number on the wake behind a surface-piercing body up to a value of $F_n = 3$. Before the effect of the scale is investigated for the two geometries, the capabilities of the flow solver for such simulations are validated with the help of a grid-study and the comparison to available experimental data.

To study the grid dependency of the results, the resistance of the profile for a Froude number of $F_n = 1$ is computed on three different grids. The coarsest grid consists of approximately 200000 cells, while the two finer grids are obtained by applying one or two more levels of cell refinement around the body. This results in a number of 530000 cells for the medium grid and 1.6 million cells for the finest grid, respectively. The resulting resistance coefficients are depicted in fig. 5.21. An asymptotic convergence is visible in

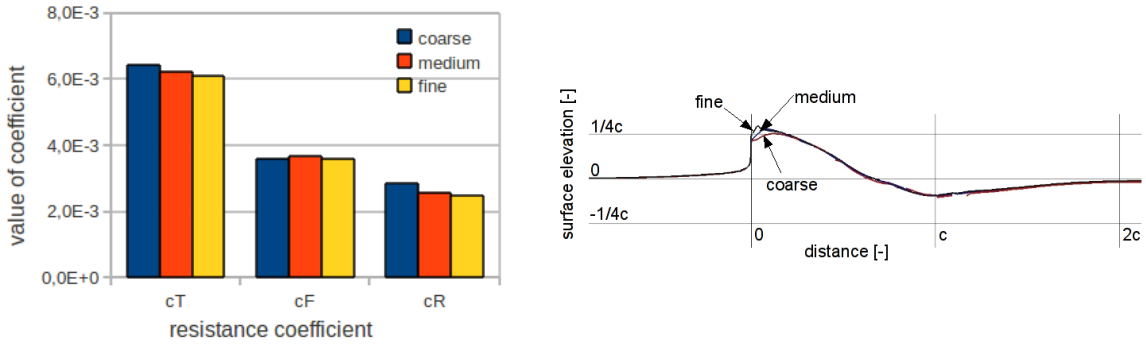

Figure 5.21: Computed resistance coefficients and wave elevations for the profile on three different grids and $F_n = 1$.

the total resistance and the residual resistance, while the highest frictional resistance is obtained for the medium grid. Overall, the differences are small with a maximal deviation

of 5% in the total resistance between the coarse and the fine grid. Furthermore, equivalent shapes of the wave elevation are predicted, as displayed in the right picture of fig. 5.21. Here, only little differences are visible near the leading edge of the profile. Afterwards, an analogues study is performed for the cylinder. Here, the coarsest grid consists of approximately 230000 cells, while the medium grid contains 490000 cells and the fine grid has 1.5 million cells, respectively. No asymptotic convergence in the resistance values is obtained in fig. 5.22 (left), but the changes between the medium and the fine grid are below 3%. Taking into account the complex and unsteady shape of the resulting wave system with a breaking bow wave, the deviation is within acceptable limits. Additionally, the results for the cylinder are validated with the help of experimental data (Rhee [70]) for the observed wave heights behind the cylinder. A comparison between this data and the computed wave contour at two different y-z-planes is depicted in fig. 5.22 on the right hand side. Analogues to the observations made by Rhee, the surface elevation is over-predicted by the numerical results within one diameter out of the symmetry plane compared to the measurements. Outside this sector the agreement is good, especially for the plane located less than one diameter behind the propeller. The larger deviations in the second plane ($x/D = 2$) can be attributed to the coarser grid resolution in this region. Overall, the quality of the results seems to be sufficient and in both cases the medium grid is chosen for the subsequent investigations.

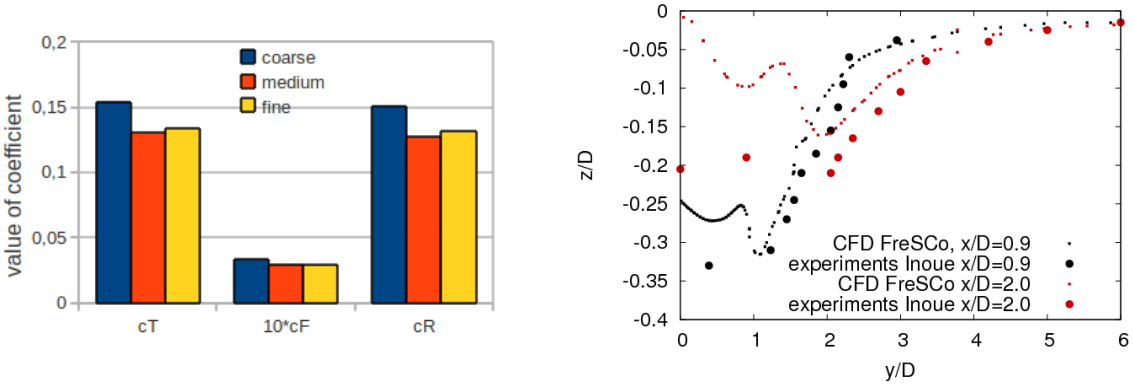

Figure 5.22: Computed resistance coefficients for the cylinder on three different grids and $F_n = 1$ (left). The right picture shows the comparison of the computed wave elevation to experimental data.

In the following, calculations are performed for three Froude numbers and four scale factors according to table 5.3. In the simulations for $\lambda = 0.1$ the flow is considered to be laminar, while the $k - \omega$ turbulence model is applied for the larger scale factors. The results are analysed in terms of the computed wave elevation and the pressure distribution on the body surface. Here, the aim of this study is to determine the influence of the

scale on the flow around the surface-piercing body. Figure 5.23 shows the comparison of the computed wave elevation for the different scale factors and two Froude numbers. In both cases, the largest deviations can be found between the laminar case $\lambda = 0.1$ and the turbulent cases, but in the case of $F_n = 0.5$ the differences are smaller.

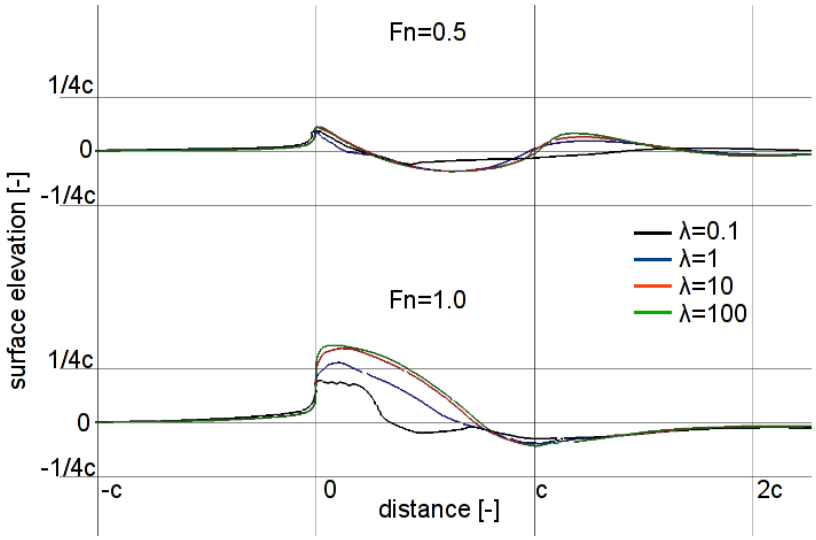

Figure 5.23: Influence of the scale on the wave elevation for the surface- piercing cylinder and two different Froude numbers.

An analogues conclusion can be derived from the obtained results for the wave system around the cylinder. Again, the largest deviations are visible between the laminar case and the turbulent cases. But compared to the investigations on the profile larger deviations are visible between the results at $F_n = 1$, due to the unsteady behaviour of the wave system around the cylinder.

To follow, the pressure distribution on the body surfaces is analysed. Fig. 5.25 depicts the pressure coefficient along the waterline for both geometries and a Froude number of $F_n = 0.5$. The left picture displays the obtained results for the profile and the right picture shows the respective values for the cylinder. In both cases, the results for the three largest Reynolds numbers are qualitatively similar, while a different contour of the pressure coefficient is obtained for the laminar case. In conclusion, the results reveal only a small influence of the Reynolds number on the results, when the flow is assumed to be fully turbulent.

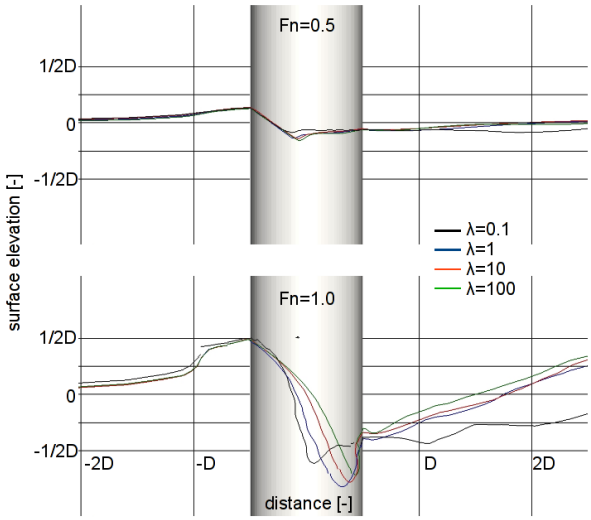

Figure 5.24: Influence of the scale on the wave elevation for the surface- piercing cylinder and two different Froude numbers.

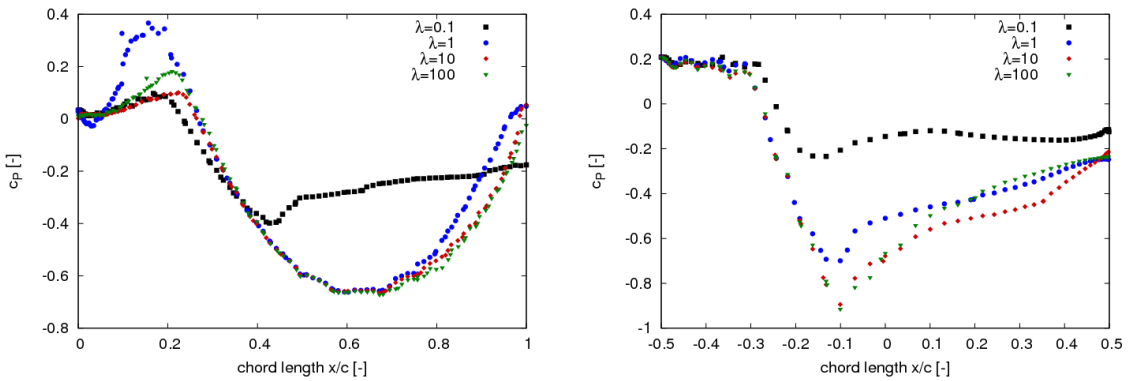

Figure 5.25: Scale influence on the pressure coefficient along the water line at $F_n = 0.5$. The left picture displays the result for the profile, while the results for the cylinder are depicted on the right.

5.6.2 Ventilating propeller at two different Reynolds numbers

Following, simulations with a ventilating propeller are made at two different Reynolds numbers to review the above made conclusion for propeller flows. For these calculations an immersion ratio of $H/R = 1.5$ is chosen and the advance coefficient is assigned to $J = 0.15$. The Reynolds number based on the chord length at $r/R = 0.7$ for the model propeller refers to $R_e = 0.5 \cdot 10^6$ and the corresponding value for the full scale propeller is $R_e = 2.8 \cdot 10^7$. Thus, in both cases the flow is considered fully turbulent using the $k - \omega$ turbulence model. The results are analysed in terms of the predicted thrust losses and the shape of the free surface. The latter is exemplary illustrated in fig. 5.26, where an almost equivalent amount of ventilation at the propeller blades is visible.

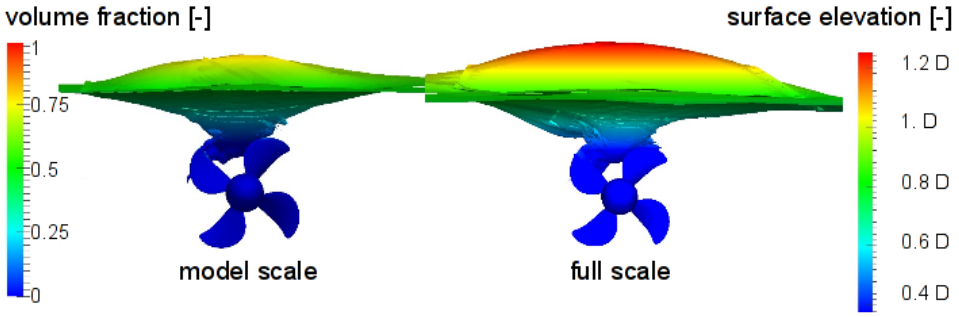

Figure 5.26: Ventilating propeller at two different Reynolds numbers ($J = 0.15$ and $H/R = 1.5$.)

Figure 5.27 compares the computed thrust losses for these two cases. Therein, the model scale results are shown in black, while the red crosses depict the obtained values for full scale. Equivalent thrust losses are observed for the two Reynolds numbers and an impact of the scale factor is again not visible. This result is in agreement with the findings of Minsaas [59], who finds scale effects to be negligible above a critical Reynolds number of $R_e = 3 * 10^5$. Although Minsaas draws his conclusion from deeply submerged propellers, he is in line with Shiba [76]. Shiba's findings are based on model tests with surface piercing cylinders and profiles. Therein, the author observes an impact of the Reynolds number only for small geometries and laminar flows, while the influence of the Reynolds number vanishes above a certain value ($R_e \approx 10^5$), which again confirms the findings in section 5.6.1.

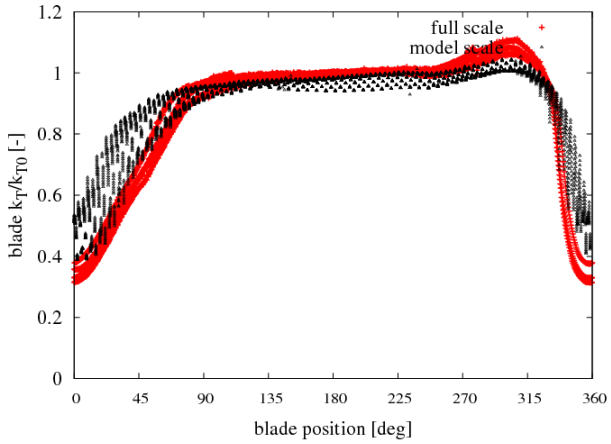

Figure 5.27: Thrust losses due to ventilation for different Reynolds numbers at $J = 0.15$ and $H/R = 1.5$.

6 Approach for efficient sea-keeping simulations

In the previous chapter the interaction of an open-water propeller with the free surface has been investigated. During these simulations, the inflow towards the propeller is considered to be homogeneous. However, in the case of a manoeuvring vessel in waves, where the propeller works in the inhomogeneous wake field, the operating conditions of the propeller vary strongly over time. Here, especially the heave and pitch motions have a significant impact by changing the distance between the free surface and the propeller. With these scenarios in view, also a procedure for the simulation of the ship motions is necessary. As inviscid-flow methods are not able to predict the wake flow accurately, the RANS method *FreSCo*$^+$ shall be used within this thesis to determine the ship motions. Thereby, the motions are computed with the six degree of freedom motion solver described in section 3.4.3, while the waves are generated by using the Airy theory (section 3.4.2).

The associated challenge of viscous sea-keeping simulations refers to the large computational times. Alongside the problem of the different time scales between ship and propeller motions (c.f. section 3.1.2), the computational effort is mainly influenced by the strong grid and time-step requirements. The grid requirements are a result of the challenge to accurately simulate the propagating wave-field towards the floating body without any significant wave damping. In consequence of this, the possible time-step size is strongly limited due to the Courant number (section 3.4.2), and due to this a large number of time steps become necessary to resolve the ship motions. Another big issue in viscous sea-keeping simulations refers to the avoidance of wave reflections at the outflow boundaries. Typically, large amounts of numerical damping are introduced in front of the outflow to remove all waves before reaching the domain boundary. In the classical case, grid-stretching techniques are used. These techniques are often referred to as numerical beach methods (see Xing [90] for example). Due to their inherent directionality, such grids are not suitable for simulations of variable wave directions or waves from behind. An example for such a computation refers to the simulation of a turning test in waves, as demonstrated by Manzke et. al in [58]. Therein, the wave direction is earth-fixed, while the physical domain is moving with the vessel and waves can enter or leave the domain in all directions. To overcome the difficulties at the outflow boundaries, various approaches can be found in the literature. An overview of the different groups of methods is given in

section 3.3.2, where the SWENSE approach (Gentaz et. al [31]) is also presented. This method uses an inviscid formulation to model the waves in the far-field, while the flow in the vicinity of the floating body is considered to be viscous. The method described in this chapter shows some similarities to the SWENSE approach by trying to couple a previously determined inviscid wave-field to the RANS method. The aim of this effort is to combine the merits of both methods, i.e. the accuracy of the viscous-flow method regarding the prediction of the inflow conditions towards the propeller, and the small computational times of potential flow methods to simulate a propagating wave field. Additionally, a unique formulation of the flow conditions at the inflow and outflow boundaries allows for the simulation of arbitrary wave directions. The procedure facilitates the use of very compact domains to reduce the required amount of cells and therewith computational times. In the next section, the developed algorithm is described in more detail, while the following sections are devoted to some validation and verification cases.

6.1 Description of the algorithm

The present approach tries to establish an implicit coupling of an inviscid wave description in the far field to the viscous flow in the interior of the domain. Analogues to the SWENSE approach, the solution of the coupling approach is consistent to the inviscid method in the far-field, whereas the inviscid method does not contain the floating body. Near the floating body the approach fulfils the boundary conditions for the viscous-flow method. While the SWENSE approach uses a decomposition of the variables (e.g. velocity, pressure) in a diffracted and a baseline solution resulting in a different formulation of the governing equations, the present coupling employs a manipulation of the original formulation of the equation system. Thus, deviating from the usual formulation of the linear equation system (LES) in eq. (6.1)

$$A_P \cdot \phi_P + \sum_{NB} A_{NB} \cdot \phi_{NB} = S_\phi \,, \tag{6.1}$$

the following formulation is used:

$$\left[1 + \ \beta \ \alpha^n(\mathbf{x})\right] \ A_P \, \phi_P + \sum_{NB} A_{NB} \, \phi_{NB} = S_\phi + \left[A_P \ \beta \ \alpha^n(\mathbf{x}) \ \phi_P^*\right] . \tag{6.2}$$

In these equations, A_P marks the main diagonal (central) coefficient, the sum $\sum_{NB} A_{NB}\phi_{NB}$ denotes to the implicit contributions from the neighbouring cells and S_ϕ refers to the source term. This modification of the equation system is applied to the momentum equations and the VOF-equation. Thus, ϕ is a synonym for the velocity components and the mixture fraction. Obviously, the manipulation results in $\phi_P \approx \phi_P^*$ for large values

of $\beta \times \alpha(\mathbf{x})$. The two extra terms in eq (6.2) contain the parameter β, which controls the intensity of the manipulation, and the shape function $\alpha = \alpha(\mathbf{x})$, which restricts the manipulation to a certain region located between the boundaries and the interior of the domain as shown by the dashed line in fig.6.1. Within this zone the damping of the diffracted wave field has to be managed by an appropriate construction of the parameters α and β to match a compatible wave description at the boundaries.

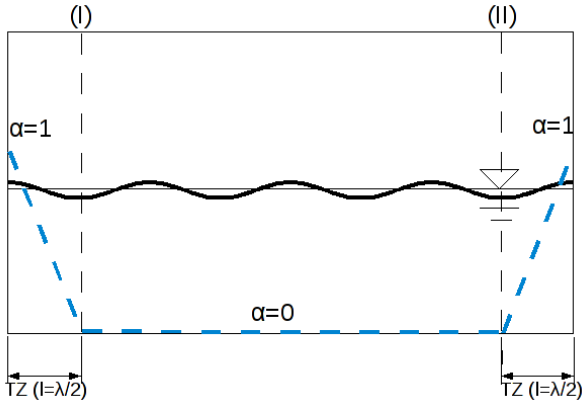

Figure 6.1: Illustration of the extensions of the transition zone and the shape of the α-function.

In the interior of the domain the shape function is set to zero, while the value for α increases to $\alpha = 1$ inside the transition zone. The length of this zone (TZ) is typically set to $l = \lambda/2$. In the picture, α is shown as a linear function $(n = 1)$, while in some of the below described cases a quadratic shape function $(n = 2)$ is used. Although other authors like Clement [22] recommend larger zones $(l = 2\lambda)$, the simulations in section 6.2 - 6.4 show that even such a small zone ensures the compliance of the viscous-flow method and the inviscid-flow method. Next to the length of the transition zone, the most crucial parameter in the procedure is the intensity β. The choice of this parameter is important for the avoidance of incompatibilities between the involved wave fields, that would induce a disturbance in the wave field. Too small values for β result in an incompatibility at the boundaries, while too large values for β produce a disturbance at the beginning of the transition zone. In both cases wave reflections are the result.

As stated above, the manipulation of the equation system yields $\phi_P \approx \phi_P^*$ for large values of $\beta \times \alpha(\mathbf{x})$. Therein, ϕ_P is the unknown variable and ϕ_P^* corresponds to the respective variable value determined by the inviscid method. Within this thesis, the implementation of the inviscid-flow method is based on the Airy theory. Thus, the equations 3.13 - 3.15 are used to determine the variable ϕ_P^*. Additionally, the same equations are used to apply the inviscid-flow method as identical Dirichlet boundary condition at all lateral

and longitudinal boundaries of the domain, which are indicated by the grey planes in fig. 6.2.

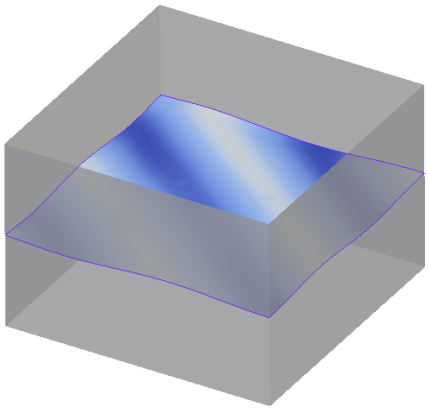

Figure 6.2: Illustration of a typical computational domain.

The horizontal planes of the domain are idealised by pressure boundaries. Here, the hydrostatic pressure is prescribed, while a Neumann-type boundary condition is used for the velocities and the mixture fraction. Although identical formulations for all vertical boundaries are used in the mathematical model, the boundaries are subdivided into "wave-inlets" and "wave-outlets" in the following discussion. A boundary is called "wave-inlet" , if the wave-velocity vector points inside the domain, while the waves leave the computational domain at a "wave-outlet".

6.2 Identification of the required control parameters

A test case using a simple two-dimensional wave tank without any floating body is used to determine the necessary control parameters introduced in eq. (6.2). Main focus of this study is to gain experience on the required values for the amplitude parameter β. In a first step, three different wave lengths in combination with four wave amplitudes and three different inflow velocities are chosen to investigate the influence of the amplitude parameter on the wave elevation inside the transition zone. During this parameter study, six different amplitude parameters between $\beta = 0.01$ and $\beta = 0.25$ are applied, which result in a computational exercise of more than 200 simulations. As the magnitude of the amplitude parameter is unknown, the first set of values is only a rough estimation. The computational grid for this analysis consists of approximately 20000 cells and is shown in fig. 6.3 on the right hand side, while the dimensions of the computational domain are

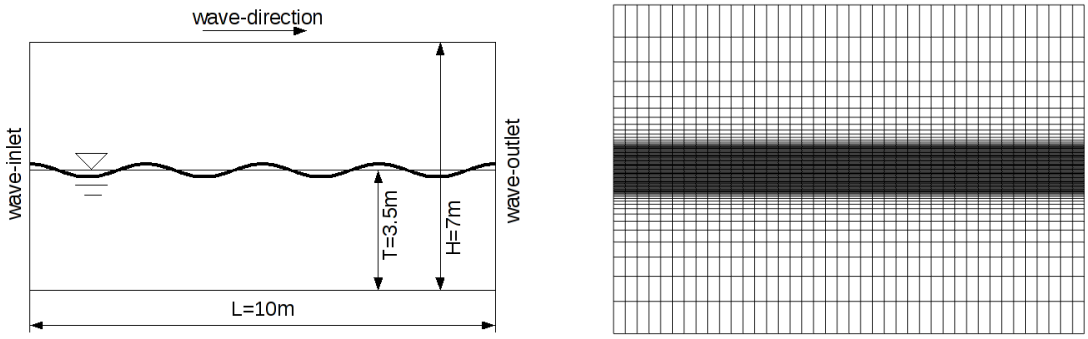

Figure 6.3: Dimensions and computational grid of the two-dimensional wave tank.

given on the left. The grid spacing in the horizontal direction is equidistant ($dx = 0.1m$), while a refinement in the free-surface region is used in vertical direction. Around the initial free surface position a grid spacing of $dz = 0.02m$ is achieved. Each calculation runs over a number of 30000 time steps, which results in a simulation time of $t = 150s$. Hence, for the largest wave length 83 wave periods and for the smallest wave length 108 wave periods are simulated. The main parameters for the calculations are summarized in table 6.1. According to the method described before, a Dirichlet condition for the velocity components and the volume fraction is applied at the boundaries marked with "wave-inlet" and "wave-outlet" in fig. 6.3. At both boundaries a regular Airy wave is generated, which travels from left to right in all simulations.

parameter	**value**
amplitude parameter	$(0.01, 0.02, 0.03, 0.05, 0.1, 0.25)^T$
inflow velocity $\left(\frac{v_{s_x}}{(g \cdot \nu)^{1/3}}\right)$	$(-4.67, 0, 4.67)^T$
wave length (λ/L)	$(0.3, 0.5, 0.7)^T$
wave height (H_W/L)	$(0.008, 0.012, 0.016, 0.02)^T$
time-step size	$5e^{-3}s$

Table 6.1: Parameters varied during the study on the influence of the amplitude parameter.

In the following, the evaluation procedure is described which is used to analyse the results of the different simulations. To assess the influence of the applied manipulations in the transition zones, the wave elevation is monitored at a number of observation points inside the tank. Most of the points are located near the boundaries, while one point is placed in the middle of the domain. From the time signal ($\zeta(x_B, t)$) observed at the different points (x_B) and the shape of the undisturbed Airy wave at the specific location, a time independent wave amplitude ($\tilde{\zeta}$) can be computed with the help of a least-square

algorithm:

$$\sum_t \left(\zeta(x_B, t) - \tilde{\zeta} \cos(\omega t - k x_B) \right) = \min \ . \tag{6.3}$$

Hence, the computed wave signal is projected on a regular Airy wave, which has the same wave period as the wave generated at the boundaries. Possible deviations between the computed wave and the Airy wave in terms of the wave amplitude, the wave period or the wave phase will result in larger or smaller amplitudes $(\tilde{\zeta})$ compared to the undisturbed Airy wave. An exemplary result for one simulation is displayed in fig. 6.4. Here, the time-independent wave amplitudes, normalised with the wave elevation obtained from the Airy theory $(\hat{\zeta})$ are displayed with open symbols at the different monitoring points. Additionally, the borders of the transition zones are marked with red circles in the figure. Due to viscous and numerical effects (e.g. discretisation errors), the wave height decreases inside the tank. But due to the imposed modification inside the transition zone in front of the outflow boundary, the computed wave is transformed back into the Airy wave, which results in an amplitude ratio close to one at $x/L = 1$.

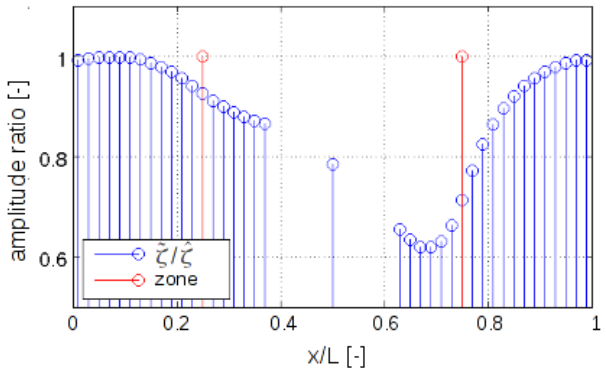

Figure 6.4: Exemplary result for the normalised wave elevation at the single points ($\lambda/L = 0.5$, $H_W/L = 0.02$ and $v_{s_x} = 4.67\,(g\nu)^{1/3}$).

This observation of the amplitude ratio $(\tilde{\zeta}/\hat{\zeta})$ provides a measure for the local deviation between the computed wave and the wave elevation obtained from the Airy theory. In the example shown in figure 6.4, the amplitude ratio increases smoothly and the computed wave coincides with the Airy wave at the boundary, which indicates a appropriate choice of the amplitude parameter. In the case of a smooth transformation of the wave in the transition zones, the increase of the amplitude ratio shows a s-shape. This contour, as illustrated in fig. 6.5 is similar to a logistic sigmoid function, which is given in eq. (6.4) in a generalised form.

$$\frac{\tilde{\zeta}}{\hat{\zeta}} \approx 1 - \frac{1}{1 + e^{\ \tilde{x}/\lambda + \ldots}} \ . \tag{6.4}$$

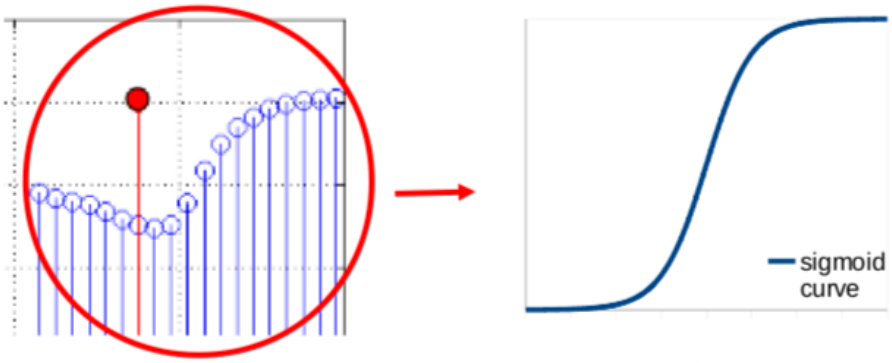

Figure 6.5: Observed normalised wave-amplitude ratio (left) and typical shape of a sigmoid function (right).

The path of the amplitude increase depends on the wave parameters and the applied amplitude parameter. In the work of Drazyk [24], the influence of the single wave parameters on the increase of the amplitude ratio is studied carefully. The authors effort finally results in an extended sigmoid function, which contains the influence of the single parameters:

$$\frac{\tilde{\zeta}}{\hat{\zeta}} = 1.01 - \frac{\tau_1\ (\lambda/L) + \tau_2\ (H_W/\lambda)}{1 + e^{\left[\xi/\lambda + \tau_3\ (v_{s_x}/(g\,\nu)^{1/3})\right]\ \tau_4\ \beta}}\,. \tag{6.5}$$

The variable ξ/λ denotes to the normalised position inside the transition zone ($\xi/\lambda \in [0, 0.5]$. Thereby, a value of $\xi/\lambda = 0$ refers to the position at the domain boundary, while $\xi/\lambda = 0.5$ denotes to the beginning of the transition zone. The unknown parameters τ_i are determined from an optimisation approach using a least-square algorithm provided by the MATLAB-suite[1]. Afterwards, the optimisation facilitates an approximate analytical expression of the amplitude ratio $(\tilde{\zeta}/\hat{\zeta})$ in the transition zone. Figure 6.6 displays an exemplary comparison between the sigmoid approximation (dashed blue line) and the observed values for the amplitude ratio (open symbols), which reveals a fair agreement. A similar agreement is experienced for all investigated cases featuring appropriate values for β. Henceforth, eq. (6.5) is considered as a reliable analytical approximation of the computed free-surface elevation.

Finally, the inverse function of the sigmoid function is calculated to determine a formula to estimate an appropriate β-value for further calculations.

$$\beta = \frac{\ln\left[\frac{\tau_1\ (\lambda/L) + \tau_2\ (H_W/\lambda)}{1.01 - (\tilde{\zeta}/\hat{\zeta})} - 1\right]}{\left[(\xi/\lambda) + \tau_3\ (v_{s_x}/(g\,\nu)^{1/3})\right]\ \tau_4}\,. \tag{6.6}$$

[1] www.mathworks.de

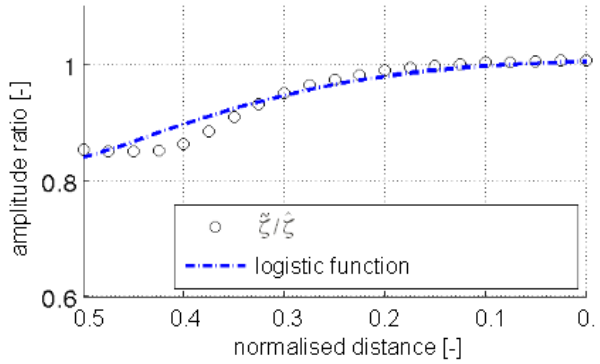

Figure 6.6: Comparison of approximated (logistic function) and computed ratios $\tilde{\zeta}/\hat{\zeta}$ inside the transition zone.

However, the result analysis shows that overall smaller values for the amplitude parameter can be used, as a smooth increase of the amplitude ratio in the transition zone can only be observed for the smaller β-values. Furthermore, the grid has to be refined to provide a sufficient grid resolution for all investigated wave heights. Hence, a second set of parameters is investigated on a finer grid. The resolution in the horizontal direction is found to be sufficient and can therefore be kept constant. For the smallest investigated wave length ($\lambda = 4m$) the applied grid spacing of $dx = 0.1m$ provides a resolution of 40 cells per wave length. This grid resolution still results in slightly damped waves, but a finer grid resolution in wave direction is not practical for three-dimensional applications, due to the large computational effort. In the clustered zone around the initial free surface a grid spacing of $dz = 7 \cdot 10^{-3}m$ is used, which results in a minimum of 10 cells per wave amplitude. Overall, the grid consists of 25000 cells. The parameters varied during the second set of computations are summarized in table 6.2.

parameter	**value**
amplitude parameter	$(0.001, 0.002, 0.003, 0.004, 0, 005, 0.006, 0.007,$ $0.008, 0.009, 0.01, 0.03, 0.05, 0.1)^T$
inflow velocity $\left(\frac{v_{s_x}}{(g \cdot \nu)^{1/3}}\right)$	$(-4.67, 0, 4.67)^T$
wave length (λ/L)	$(0.4, 0.5, 0.6)^T$
wave height (H_W/L)	$(0.014, 0.02, 0.026)^T$
time-step size	$5e^{-3}s$

Table 6.2: Parameter variation for the computational exercise on the refined grid.

The results are analysed according to the previously described evaluation procedure. An

τ_i	1	2	3	4
value	0.2873	0.9497	-0.0412	$1.055 \cdot 10^3$

Table 6.3: Parameters τ_i obtained for the investigated data set.

example for one set of wave parameters and two different amplitude parameters is given in fig. 6.7. In the left figure only small modifications are applied on the wave in the transition zones. Here, the amplitude ratio at the outflow boundary is smaller than one, which indicates deviations between the approaching wave and the Airy wave. This discrepancy in the surface elevation causes wave reflections at the outflow. Henceforth, the used value for β is assumed to be too small for the given set of wave parameters. Opposite to this, the right figure demonstrates the effect of a larger amplitude parameter. In this case, strong modifications are applied on the wave in the transition zone, which result in a sudden increase of the amplitude ratio in the first part of the zone. As a result of this, wave reflections can occur at this point. Thus, the used amplitude parameter is found to be too large for these parameters. Valid amplitude parameters for this set of parameters can be found in the range of $\beta = 0.004$, as indicated by fig. 6.8.

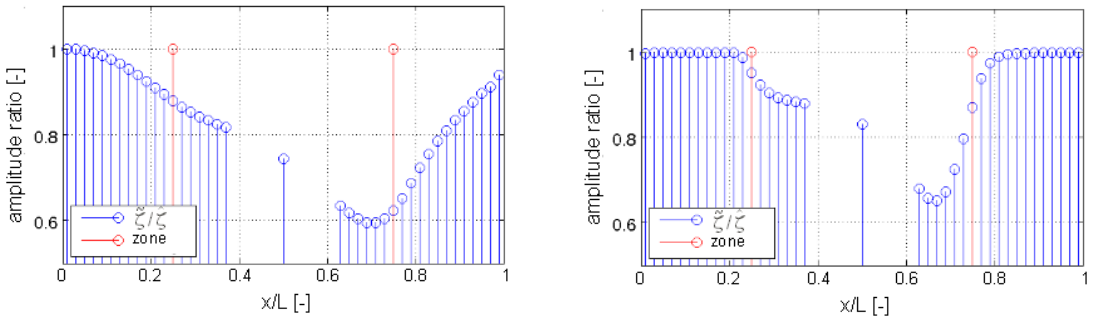

Figure 6.7: Results obtained with a wave length of $\lambda/L = 0.5$, a wave height of $H_W/L = 0.02$ and an inflow velocity of $v_{s_x} = -4.67\,(g\nu)^{1/3}$ ($\beta = 0.001$, (left) and $\beta = 0.05$ (right)).

In summary, the evaluation of the results reveals that amplitude parameters in the range of $\beta = 0.003$ and $\beta = 0.01$ are suitable to achieve a smooth increase of the amplitude ratio in the transition zone. Henceforth, this range of parameters enables a transformation of the computed wave into the Airy wave in front of the outflow boundary without generating wave reflections. The results of all simulations using a valid value for the amplitude parameter are afterwards used to determine the unknown parameters τ_i in eq. 6.6. For the present data set the values given in table 6.3 are obtained.

As a last parameter the influence of the grid density is investigated with three systemat-

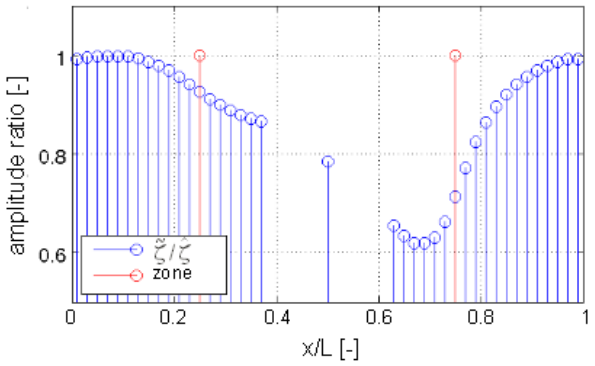

Figure 6.8: Example for an appropriate choice of the amplitude parameter for $\lambda/L = 0.5$, $H_W/L = 0.02$ and $v_{s_x} = -4.67\,(g\nu)^{1/3}$.

ically refined grids. The grid used previously serves therein as medium grid, whereas the grid spacing of the coarse grid is twice the value of the medium grid. The finest grid is obtained by dividing each cell of the medium grid into four equivalent cells.

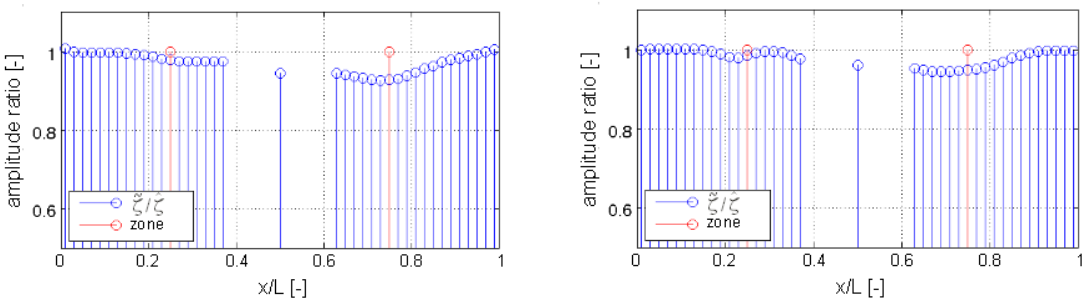

Figure 6.9: Exemplary results obtained for the medium grid (left) and the fine grid (right) for an amplitude parameter of $\beta = 0.005$ ($\lambda/L = 0.5$, $H_W/L = 0.02$, $v_{s_x} = 0$).

In general the obtained results show only a small grid dependency. Figure 6.9 depicts exemplary results for a wave length of $\lambda/L = 0.5$ and a wave amplitude of $H_W/L = 0.02$. An additional inflow velocity is not considered in these examples and the amplitude parameter is set to $\beta = 0.005$. The medium grid is used to obtain the picture on the left, while the fine grid is used for the corresponding result on the right hand side of the figure. Only small differences between the two results are visible and a smooth increase of the amplitude ratio is observed in both cases. Reviewing eq. (6.2) the amplitude parameter is a factor applied on the central coefficient (A_P), which already contains informations on the grid topology. Thus, the grid resolution is already included in eq. (6.2) and it is

therefore not necessary to include an influence of the grid density in eq. (6.6).

Figure 6.10 depicts the corresponding results for the coarsest grid. Despite the small oscillations in the amplitude ratio, which are a result of the algorithm to reconstruct the free-surface height at the observation points, the computed wave is consistent to the undisturbed Airy wave at the "wave-outlet". Thus, the same value for the amplitude parameter can be used on all three grids.

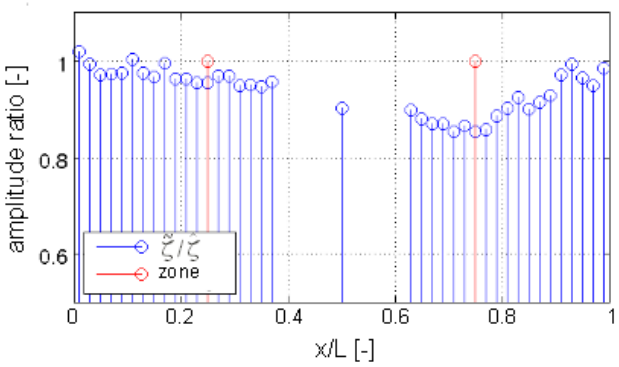

Figure 6.10: Corresponding result to fig. 6.9 for the coarsest grid ($\lambda/L = 0.5$, $H_W/L = 0.02$, $v_{s_x} = 0$, $\beta = 0.005$).

6.3 Wave loads on a simple floating body

Towards practical relevant applications, the next test refers to a three-dimensional wave tank with a fixed cuboid. The objective of this test is to examine the performance of the approach in case of wave diffraction due to a floating body. The cuboid is located in the middle of a rectangular domain, as illustrated in figure 6.11 on the left hand side. As can be seen from the figure, the dimensions of the domain are rather compact compared to the size of the cuboid. Especially the short distance between the cuboid and the "wave-outlet" is expected to be very challenging for the present approach. Due to the severe disturbances of the propagating wave field generated by the cuboid, large modifications on the wave field are necessary in the transition zone in front of the "wave-outlet" . This in turn transforms the diffracted wave into the undisturbed Airy wave. The employed block-structured grid consists of 100x100x50 cells and is illustrated in fig. 6.11 on the right hand side.

The simulations are performed for a wave length of $\lambda = 5m$ and a wave amplitude of $\hat{\zeta} = 0.1m$. The inflow velocity is set to $v_{S_x} = 1m/s$ and the amplitude parameter is

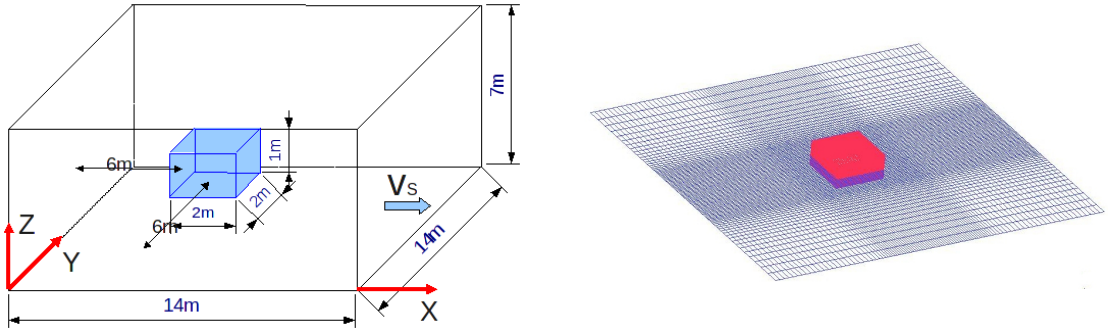

Figure 6.11: Computational domain and grid for the cuboid in a wave tank.

varied between $\beta = 0$ and $\beta = 1$. Analogues simulations are done with the conventional approach using a numerical beach to generate a reference solution. The extended domain has a total length of $L = 25m$ and provides a region with stretched cells in front of the outflow boundary.

Snapshots of the predicted wave fields are shown in fig. 6.12. The upper left picture refers to the simulation using the numerical beach method, while in the three other cases different values for the amplitude parameter are used. The upper right picture is obtained from a simulation with an amplitude parameter of $\beta = 0$. Here, the undisturbed Airy wave is imposed at the boundaries, but no manipulation of the equation system is applied in the transition zones.

The pictures shown in the lower part of fig. 6.12 pertain to simulations with an amplitude parameter of $\beta = 0.0026$ (left) and $\beta = 1$ (right). In all four cases the computed wave field in front of the cuboid is similar. Nearly no deviations between the viscous wave and the Airy wave occur in this region and nearly no modifications of the computed wave are necessary in the transition zone near the "wave-inlet". A different situation is observed in front of the "wave-outlet", where the shape of the wave field depends on the applied boundary condition and the selected value for the amplitude parameter. In this region, the wave field consists of the propagating wave as well as the radiation and diffraction waves generated by the cuboid. To obtain a closer look on the differences between the simulations, the wave elevation in the centre plane is depicted in fig. 6.13.

As indicated above, the results for the different simulations are more or less similar in front of the floating body (left part of the figure). But in the transition zone near the "wave-outlet" (right boundary), a predictive disparity can be observed. Thus, the picture offers a closer look on the influence of the manipulations inside the transition zones and provides a better understanding of the wave transformation. At the beginning of the transition zone, the curve for an amplitude parameter of $\beta = 1.0$ (red curve) shows a sudden ascend. This indicates an overvalued amplitude parameter. In this case, the solution is dominated by the

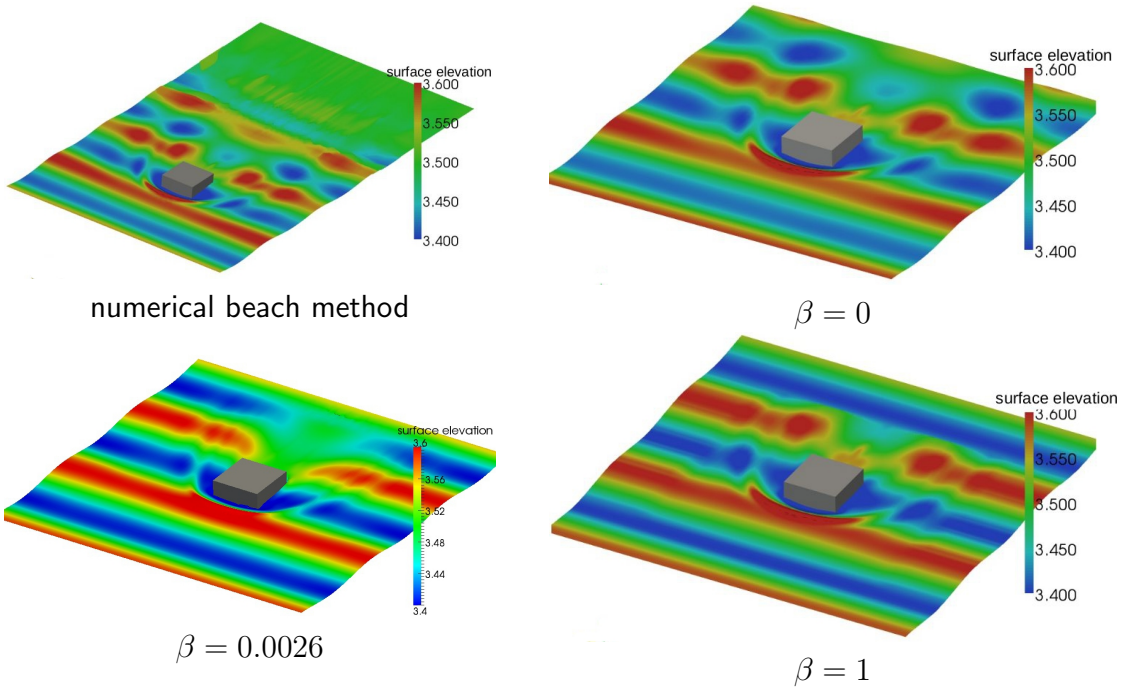

Figure 6.12: Cuboid exposed to regular head waves.

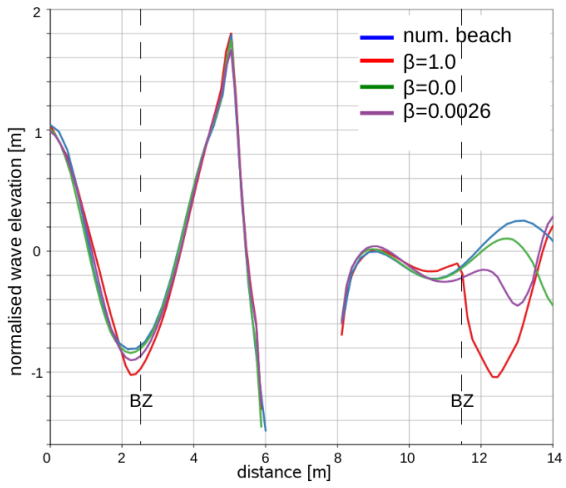

Figure 6.13: Wave elevation in the y-z plane for the four investigated cases.

imposed manipulations over the full length of the transition zone and the wave elevation strictly follows the Airy wave contour. Without a modification inside the transition zone (green curve), the solution shows some similarities to the results of the numerical-beach method (blue curve). The differences between these two solutions are a result of wave reflections at the outflow for $\beta = 0$ due to incompatibilities between the calculated wave field and the prescribed Airy wave. For appropriate values of β (purple curve) the wave contour approximately follows the wave contour of the "non-manipulated" solutions in the first part of the transition zone. With an increasing value for the shape-function α, the influence of the inviscid solution on the wave elevation increases and the computed wave contour follows the Airy wave contour near the "wave-outlet". Henceforth, a smooth transformation between the RANS solution into the Airy wave without any wave reflections can be observed in this case.

The evolution of the predicted drag forces is shown in fig. 6.14. Again, a comparison is made between the results obtained in conjunction with the numerical beach and the computations using the three different amplitude parameters. Only small differences are visible between the result for $\beta = 0.0026$ (red curve) and the reference solution using the numerical beach (green curve). In contrary to this, large deviations can be found between these results and the black curve ($\beta = 1$). Here, a footprint of the imposed modifications and the resulting wave reflections can be clearly seen. Furthermore, differences in the drag force can also be observed between the simulation with $\beta = 0$ (blue curve) and the reference solution.

Afterwards, a Fourier transformation is performed to provide a closer look on the observed discrepancies in the computed drag forces. Therefore, the percentage deviation between the Fourier coefficient obtained for one specific amplitude parameter and the corresponding coefficient from the reference solution is computed. The result for the first three Fourier coefficients is displayed in fig. 6.14 on the right. This result confirms the above made observations, whereas the coefficient manipulation does not influence the forces acting on the body for an appropriate choice of the amplitude parameter. In contrast, over- or undervalued amplitude parameters lead to a disturbance of the wave field, which influences the wave loads on the body.

6.4 Motion amplitudes of a container vessel

Next to the wave loads acting on a floating body, also the resulting motions are of specific interest when investigating floating bodies in waves. Henceforth, the aim of the present section is to investigate the capabilities of the six degree of freedom motion solver for such simulations and to study the influence of the applied manipulations in the transition zones on the ship motions. Large amplitude ship motions can cause stability problems,

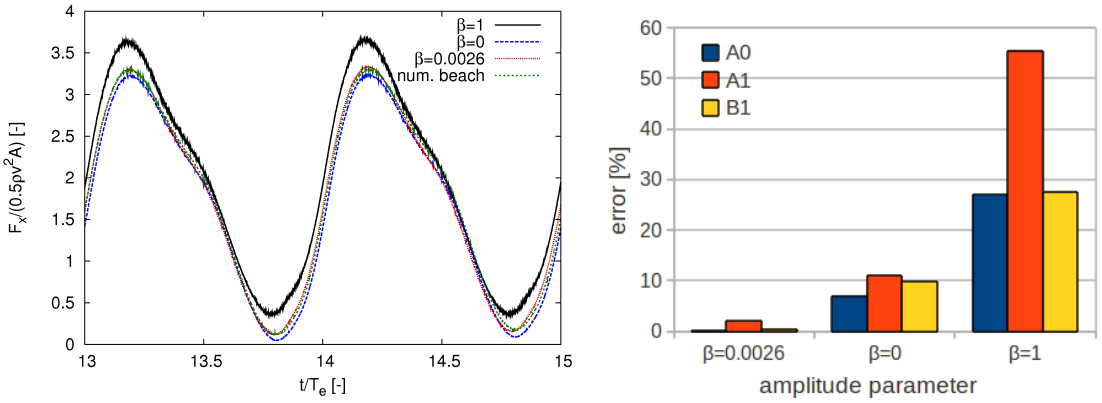

Figure 6.14: Drag forces due to regular head waves acting on the cuboid. The left picture shows a detail of the time series. The right picture depicts the corresponding deviations in the Fourier coefficients.

which endanger the safety of a ship. But also moderate motions might have a large impact on the added resistance in waves and therefore, on the possible loss of forward speed. Additionally, the motions of a vessel can lead to a pronounced unsteady behaviour of the propeller, which might yield large thrust and loading variations. The tested ship geometry refers to the KRISO container vessel (KCS) investigated experimentally at the Korean Institute for Ships and Ocean Engineering and numerically at the last Gothenborg CFD-workshop [1]. The main dimensions of the model can be found in table 6.4.

parameter	**value**
Length between perpendicular (L_{pp})	$4.367m$
Breadth (B)	$0.611m$
Draft (T)	$0.205m$
Displacement (Δ)	$0.594m^3$
wetted Surface (S)	$3.397m^2$
Froude number (F_n)	0.26

Table 6.4: Main dimensions of the container-ship model.

The location of the vessel inside the computational domain and the initial position of the free surface are displayed in fig. 6.15 on the left hand side. Further, the figure illustrates the compact dimensions of the domain, where the inlet is located approximately $1/3L_{pp}$ in front of the ship and the outlet is placed only $2/3L_{pp}$ behind the transom. The distance between the centre line of the model and the lateral side of the domain refers to $0.5L_{pp}$. The computational grid is depicted on the right hand side of fig. 6.15 and consists of

approximately 800000 cells. Most of the cells are located near the free surface and around the vessel. Only head waves are investigated here, which allow the use of only one half of the ship and a symmetry boundary condition at the centre plane.

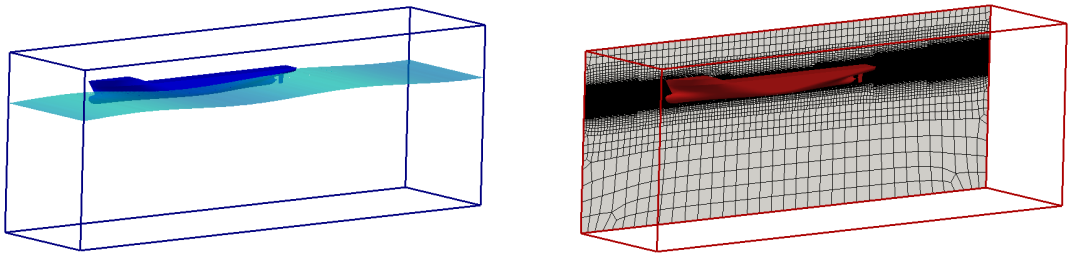

Figure 6.15: Computational domain and grid used for the investigation of the container ship.

The vessel is investigated in regular waves with a wave length of $\lambda = 1.15 \cdot L_{pp}$ and a wave amplitude of $\hat{\zeta}/L_{pp} = 0.0096$. This condition refers to one of the cases investigated at the Gothenborg CFD-workshop in 2010 [1]. Henceforth, the results of the simulations can be validated with the experimental data published during the workshop. The ship travels with a Froude number of $F_n = 0.26$ against the waves, which result in an encounter frequency of $\omega_e = 5.61\ 1/s$. To study the influence of the modifications in the transition zones on the ship motions, three different values for the amplitude parameter are chosen ($\beta = 0.0022, 0.05, 0.1$).

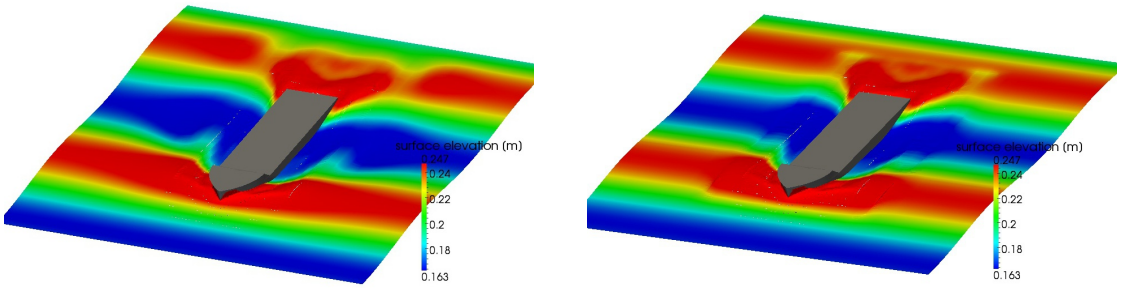

Figure 6.16: Snapshots of the predicted wave contour for the container ship in head waves ($\beta = 0.0022$ (left),$\beta = 0.1$ (right).)

Coloured plots of the computed wave field are shown in fig. 6.16 for the smallest and largest investigated amplitude parameter. Analogues to the findings in the previous subsection, disturbances of the wave field can be observed for $\beta = 0.1$ at the beginning of the transition zone, where the wave shape changes very suddenly. Opposite to this, the

wave field obtained with the smallest amplitude parameter does not show an influence of the modifications.

During the computations the heave and pitch motions of the vessel are monitored. A comparison of the computed motion amplitudes to the experimental values is displayed in fig. 6.17. Especially in the evolution of the heave amplitude, a good agreement is observed between the experiments and the simulation using an amplitude parameter of $\beta = 0.0022$ (left picture). In this case, the analysis of the pitch amplitudes reveals a sufficient agreement as well. Here, only a small phase shift is visible between the computed results and the measurements. In both cases larger discrepancies to the experimental values are obtained for the two larger β-values due to upstream travelling disturbances of the wave field, generated by the manipulations in the transition zone.

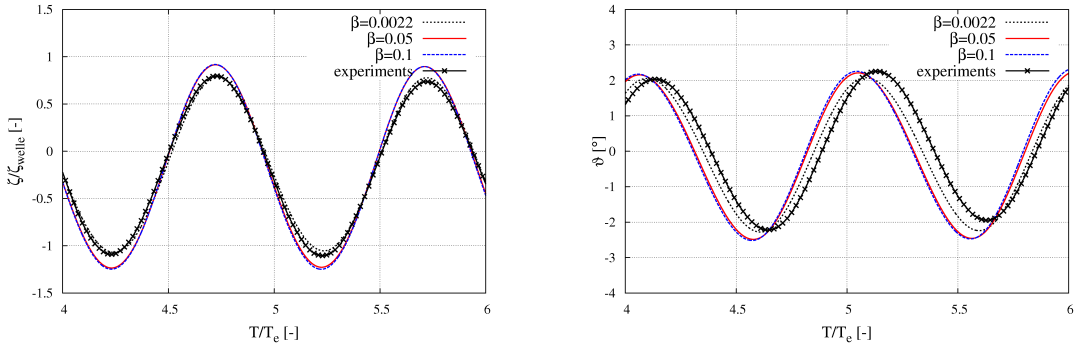

Figure 6.17: Comparison of the computed heave and pitch amplitudes to the experimental results.

7 Simulation of a self-propelled ship in waves

Throughout the preceding investigations, outlined in chapter 5 and 6 propeller and ship are treated separately, while possible interaction effects are still neglected. Henceforth, aim of the present chapter is to simulate a ship-propeller configuration. During these computations, the propeller is modelled with the coupling procedure presented in chapter 4. Henceforth, only the geometry of the ship is geometrically resolved inside *FreSCo*$^+$, while the influence of the propeller is considered by applying the forces computed by *panMARE*. Secondly, the approach introduced in chapter 6 for handling the boundary conditions for sea keeping simulations is used in the RANS solver. The investigated ship geometry refers to the platform-supply vessel "Far Searcher" from the Norwegian shipping company Farstad Shipping (see fig. 7.1 on the left). The vessel is investigated in the research project *PropSeas* in model and full scale as notable ventilation problems occur at the propulsion system during operation. The calculations presented below refer to simulations in model scale. In the following section the computational model is described, while the later sections show the results of the computations.

7.1 Description of the vessel

The vessel "Far Searcher" operates in the north sea off the coast of Norway. In this region heavy seas are likely to occur. Hence, large ship motions are expected, which can lead to propeller ventilation. The vessel is equipped with two pulling pod propellers each having a power of 2200 kW. The body plan of the vessel can be found in fig. 7.1 on the right hand side. The main dimensions of the ship are given in table 7.1, the propeller is the one described in chapter 5.

The following simulations refer to cases in calm water and in head seas. Thus, only one half of the ship has to be modelled as depicted in fig. 7.2 on the left. According to the coupling procedure, the computational domain in the RANS solver contains the ship hull and the pod housing as illustrated in the figure. Additionally the figure displays the refinements in the free surface region and around the ship hull and depicts that a rather

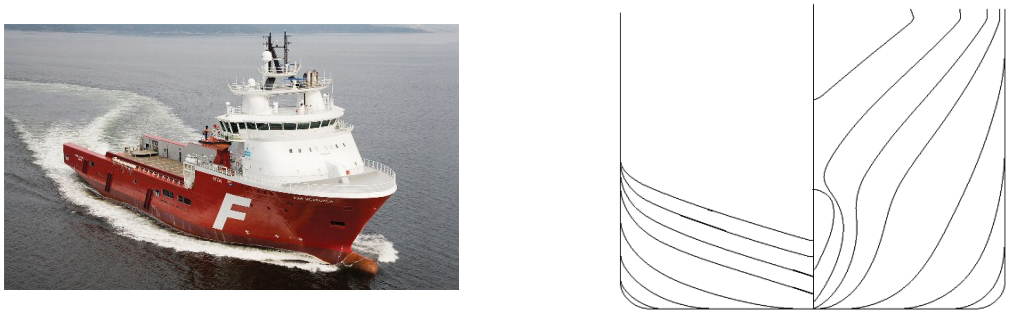

Figure 7.1: Investigated vessel "Far Searcher" and the corresponding body plan.

parameter	value	parameter	value
L_{pp}	80.8m	B	21
LCG	36.2m	VCG	7.52m
T	6.6m	scale	0.0625
n	9rps	D	3.2m

Table 7.1: Main dimensions of the platform-supply vessel.

compact domain is used for the simulations. Wave reflections at the boundaries are not expected as the procedure described in chapter 6 is applied in the boundary regions using an amplitude parameter of $\beta = 0.002$. The picture on the right hand side shows a detailed view of the grid in the aft-ship region, where the Cartesian grid in the propeller plane is shown. Overall the grid consists of 1.6 million hexahedral cells.

7.2 Estimation of the self-propulsion point

During the first simulation the vessel operates in calm water. Aim of this calculation is to estimate the self-propulsion point for the number of revolutions specified in table 7.1. The forward velocity of the vessel is initialised with an estimated value of $F_n = 0.22$, which corresponds to $v_S = 12kn$ in full scale. Throughout the simulation the vessel is free to perform movements in the vertical plane (surge, trim and sinkage). The wave system generated by the vessel in the final stage of the simulation is depicted in fig. 7.3, where the vessel reaches a stationary velocity. The corresponding Froude number can be estimated to $F_n = 0.214$. In this situation, the propeller generates a thrust of approximately $k_T = 0.244$, which results in an advance coefficient of about $J = 0.81$.

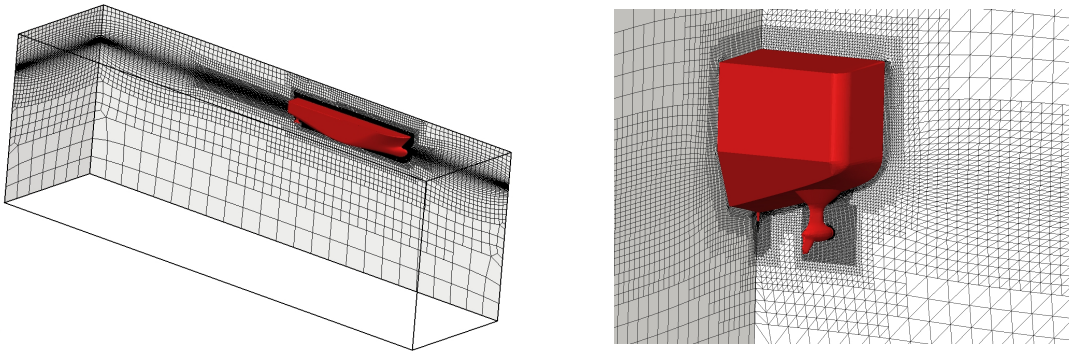

Figure 7.2: Computational grid used for the simulations of the platform-supply vessel.

Afterwards, a simulation without the operating propeller is performed. Therein, a constant inflow velocity of $F_n = 0.214$ is considered, while the position of the ship in longitudinal direction is kept constant. Aim of this simulation is to estimate the ship's resistance and the thrust deduction fraction at the self-propulsion point. The resistance of the ship and the pod-housing at the given speed refers to $\frac{R_T}{\rho n^2 D^4} = 0.212$, which results in a thrust deduction fraction of $t = 0.1$.

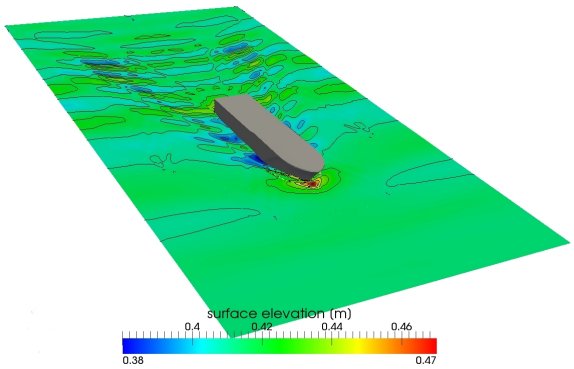

Figure 7.3: Wave system generated by the vessel at the self-propulsion point.

7.3 Added resistance in waves

Afterwards two simulations in regular head waves are performed to determine the added resistance in waves in these conditions and the corresponding loss of forward speed. The wave length is set to $\lambda = L_{pp}$, while two different values are used for the wave height.

In the first case, the wave amplitude is set to $\hat{\zeta} = 0.0125 \cdot L_{pp}$, while in the second simulation, the wave amplitude is twice the value of the first simulation. Analogues to the calm-water case, the speed of the vessel is initialised with $F_n = 0.22$, which leads to a model speed of $v_M = 1.55\,\frac{m}{s}$. Again, the propeller operates with a constant number of revolutions ($n = 9\,rps$). The evolution in time of the ship speed is shown in fig. 7.4 on the left. Therein, the red line displays the results presented beforehand for the calm-water case, while the blue and black lines illustrate the time series of the forward velocity in waves. As stated before, a steady velocity corresponding to $F_n = 0.214$ is reached at the end of the simulation in calm water. The obtained target speeds of the vessel in waves are considerably smaller. In the first case, the added resistance leads to a velocity reduction of almost 12.5%. A doubling of the wave amplitude results in a velocity reduction of almost 40%. Furthermore, in both cases larger fluctuations in the target velocity are observed. Thus, this result illustrates how even moderate wave heights can lead to a significant reduction of forward speed, although the propeller is not ventilated during the simulations.

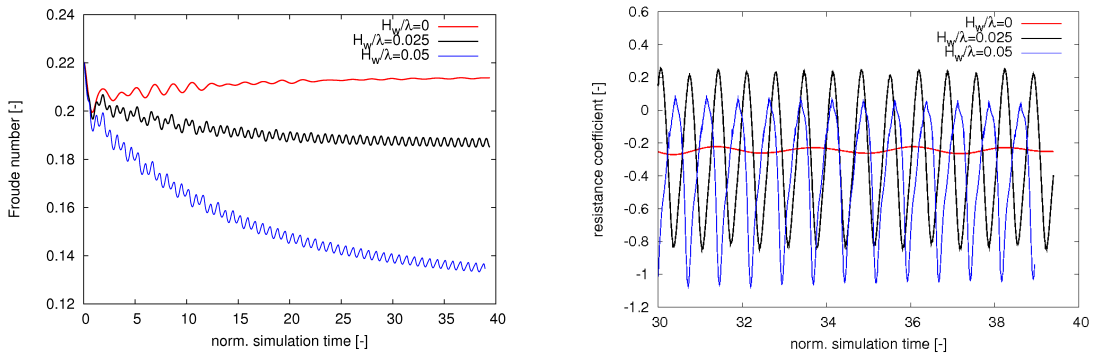

Figure 7.4: Time series of the forward speed of the vessel (left) and time history of the computed resistance coefficient $(R_T/(\rho n^2 D^4))$.

The corresponding resistance values for the investigated cases are plotted in fig. 7.4 on the right hand side for a time interval of 10 wave periods. Again, the calm-water results are illustrated with the red line, while the blue and black lines displays the ship resistance in waves. Large fluctuations are observed during the simulations in waves. In total, the increase in the time averaged resistance value for the smaller wave height can be estimated to 23% compared to the resistance in calm water. In case of the larger wave amplitude (blue curve) a time averaged added resistance of 50% can be observed. Additionally, the figure illustrates the influence of the encounter frequency. Due to the smaller forward speed in case of the larger wave height, the encounter frequency is reduced. Furthermore, due to the non-constant ship speed, the encounter period is not constant over time. In the cases investigated here, the encounter period for the case with the smaller wave height

becomes approximately $T_e = 1.22\,s$ at the end of the simulation, while the encounter period for the second case can be estimated to $T_e = 1.34\,s$. The added resistance in head waves is strongly influenced by the pitch motions of the vessel. The time history of the pitch motion for a corresponding time frame of the simulation is depicted in the left picture of fig. 7.5. The red line displays the dynamic trim of the vessel in calm water, while the blue and black lines depict the pitch motions due to head waves. Mind that the vessel trims down by the stern in static conditions as well as in calm water due to the defined loading condition. This results in a negative averaged pitch angle in head waves. Analogues to the results presented before, the influence of the encounter frequency is also visible in this figure as the period of the oscillations in the pitch angle is larger in case of the larger wave amplitude.

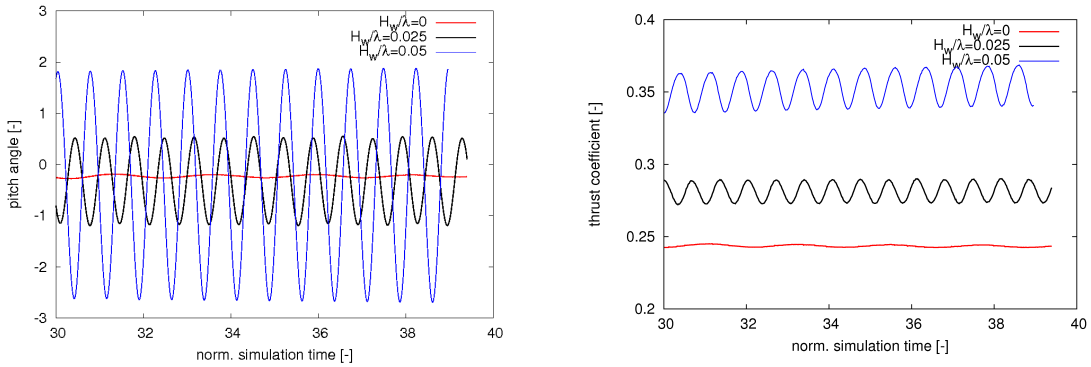

Figure 7.5: Pitch angle $(\theta\lambda/\hat{\zeta})$ of the vessel during the last 10 wave periods (left) and comparison of the computed thrust coefficients $(T/(\rho n^2 D^4))$ (right).

In addition to the previous results, the right hand picture of fig. 7.5 displays the time history of the computed thrust values. Due to the smaller forward velocity in waves, the propeller operates at a decreased advance coefficient, which leads to larger values of the thrust coefficient. Moreover, the oscillations in the thrust coefficient during a simulation are a result of the changing inflow towards the propeller due to the orbital velocities of the waves. In a situation, where a wave trough is located above the propeller, the horizontal component of the orbital velocity of the wave is directed against the propeller inflow. This results in a smaller approach flow towards the propeller, which increases the loading of the propeller. As opposed to this, a wave crest above the propeller reduces the loading of the propeller. In such a situation, the orbital velocities lead to an increased propeller inflow, which results in an larger advance coefficient. The difference between these two situations is displayed in fig. 7.6. Therein, the upper pictures show the wave field around the ship, while the lower pictures depict a longitudinal slice of the velocity field in the propeller region. In these pictures, the pressure distribution on the pod housing and the grid refinements around the pod housing are displayed as well. The left pictures

correspond to the first situation, where a wave trough is located above the propeller, while the propeller lies beneath a wave crest in the pictures on the right hand side. As can be seen from the figures, the inflow velocity towards the propeller is small compared to the velocities in the propeller stream, but the larger propeller loading in the first situations leads to smaller pressure values on the pod housing.

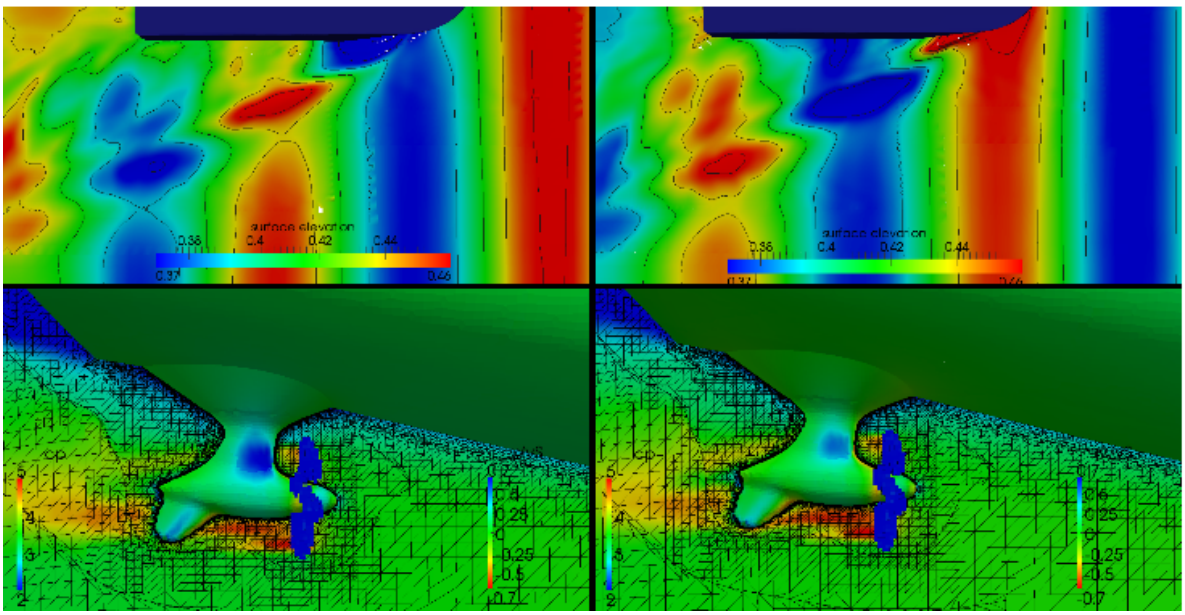

Figure 7.6: Wave pattern and velocity distribution in a longitudinal slice in the propeller position for two different situations ($\lambda = L_{pp}$ and $\hat{\zeta} = 0.0124 \cdot L_{pp}$).

Due to the lack of validation data for these simulations, only a qualitative assessment of the results is possible. But the shown results seem to be plausible and demonstrate the capabilities of the coupling procedure for the investigation of ship-propeller interaction.

8 Conclusion

This thesis documents the development of a computational procedure for the investigation of the interaction between ship and propeller, including a simulation of the ship's motions in waves. The main part of this method is a close and unsteady coupling procedure between a viscous-flow method and a method based on potential-flow theory. In the developed algorithm, the viscous-flow method is used to compute the operating conditions for the propeller, as the viscous effects in a ship's wake can not be determined with inviscid-flow methods with a sufficient accuracy. Despite the today available large computational resources, the direct computation of the rotating propeller in the ship's wake with viscous-flow methods is still very time consuming. Thus, an inviscid-flow method is used in the approach to predict the propeller forces. These forces are used afterwards to mimic the propeller in the viscous-flow method. Henceforth, the interaction of ship and propeller can be investigated without an explicit modelling of the rotating propeller in the ship's wake by combining the advantages of the two baseline methods in an efficient computational procedure.

Most available computational methods that are based on potential theory, investigate ship and propeller separately and the interaction of both is neglected. Viscous effects are assumed to be of minor importance, as the flow around propellers is dominated by lift forces. However, if the influence of the ship shall be considered, a previously computed or measured nominal wake field is used as inflow condition. In recent times viscous-flow methods are also used for simulations of the propeller flow, but here again, the interaction of ship and propeller is mostly neglected. The only exception being simulations of steady ship-propeller interaction in a numerical propulsion test. In all these methods, the propeller is typically investigated in unconfined flows and deeply submerged. This is founded on the belief that the propeller is fully submerged during normal operation and the alteration of the wake field is the most crucial factor when determining load variations. Therefore, the variations in the wake field represent the critical design criterion.

For ships operating in waves, ventilation is considered to be responsible for much larger load variations than the ones caused by the wake oscillations. Due to ventilation, load variations for a single blade or for the whole propeller from 0% to 100% are found. These large variations are mainly caused by the deviation in the fluid density of the surrounding medium, which changes by a factor of a thousand, if the propeller emerges. Even if the

propeller operates below the free surface, the propeller might be at risk of ventilation, especially when the propeller is highly loaded. In these situations an air-filled vortex is formed between the suction side of the blade and the free surface. Then, air is transported through this funnel and the respective blade becomes ventilated.

Ventilation was already a focus point of researchers since the 1930's, but was often investigated only for surface-piercing propellers. Recent investigations show an increasing occurrence of damage to mechanical components, due to ventilation on conventional propellers. A lot of this damage is reported from offshore-supply vessels and similar ships, especially while operating in dynamic-positioning mode, where large ship motions are expected and the propeller loading is at a maximum level.

Thus, methods are required to investigate the risk for ventilation and the resulting load fluctuations during the design process of a propeller. Traditionally, model tests introducing unknown scaling effects are the only possibility to capture the physics around ventilated propellers. Due to the increasing computational resources, the investigation of propeller ventilation with numerical methods becomes possible. However, the difficulties to model a ruptured free surface restrict the use of potential-flow methods, while viscous-flow methods are still afflicted with high computational expenses.

The algorithm developed within this thesis, tries to investigate the above mentioned scenarios by using a coupling procedure of a viscous and an inviscid-flow method. Therein, the operating condition for the propeller, which are computed by the viscous-flow method, are defined by the velocity distribution in front of the propeller and the position of the free surface above the propeller. These data are then used within the inviscid-flow method as inflow condition to compute the forces and moments generated by the propeller. The resulting distribution of propeller forces at the single blades is afterwards used to model the propeller influence in the viscous-flow solver by applying the propeller forces as volumetric body forces in the actual blade positions. Both methods are coupled in an unsteady algorithm to capture the actual flow conditions. One critical issue in the algorithm is the determination of the propeller induced velocities. These velocities are part of the velocity distribution computed by the viscous-flow method and they are computed by the potential-flow method as well to obtain the effective wake as inflow condition for the propeller. Verification of this aspect is achieved by analysing the propeller induced velocities for an one-bladed open-water propeller. As this study reveals a sufficient accuracy, equivalent working conditions of the propeller in both solver are assured.

Furthermore, the accuracy in capturing the position of the free surface is a critical aspect to ensure equivalent operating conditions of the propeller in the involved numerical methods. Here, the developed approach uses a Fourier transformation to derive an analytical description of the free-surface shape to allow for independent grid settings. The influence of the free surface on the flow around an open-water propeller is initially investigated with the RANS method *FreSCo*$^+$ and a geometrically resolved propeller, prior to the coupling

approach being used. The agreement of both methods in the predicted results is good and both approaches are able to capture the correct dependencies of the advance coefficient and the immersion ratio on the occurrence of ventilation. But remarkable deviations can be found between the computed and the available experimental results. When ventilation is observed in the experiments during the whole rotation of a propeller blade, the blade losses the contact to the free surface after half a rotation in the simulations. Additionally, different forms of ventilation are observed during one experiment, which can not be captured by the numerical methods due to the large computational times. Here, further improvements of the numerical methods are necessary to capture all flow phenomena caused by ventilation. However, the magnitude of the load variation is captured by the numerical approaches in most of the investigated cases. This allows to use the methods for an estimation of the expected load variations during a ventilation event.

To investigate an operating propeller behind a ship's hull, the influence of the ship motions on the propeller flow have to be additionally examined. As the working conditions of the propeller are computed in the viscous-flow solver, the ship motions have to be computed inside *FreSCo*$^+$ as well. However, sea-keeping simulations with viscous-flow methods are still afflicted with a high computational effort, due to the requirements on the cell size and the time step. Another serious issue to be considered is the suppression of wave-reflections. The approach developed in this thesis combines the RANS method with an inviscid wave description in the far-field. Between both, a transition zone is introduced. Within this zone, the compliance of the diffracted wave field around the floating body and the undisturbed waves at the boundaries is implicitly enforced by a manipulation of the equation system. Then, the approach allows for sea-keeping simulations on very compact domains and as such in acceptable computational times. In combination with the coupling approach to model the propeller, a self-propelled ship in regular waves is simulated to investigate the added resistance in waves and the resulting loss of forward speed. Although validation data for this case are not available, the results are encouraging and allow the employment of the developed methods for investigations of ship-propulsion problems in waves. Furthermore, the computational effort for such computations is greatly decreased compared to equivalent investigations with a geometrically resolved propeller. This is due to the simple and coarse grids, which can be used in the propeller plane during a coupled simulation. With this, larger time steps are possible.

To sum up, the developed coupling procedure allows to compute the load variations of a propeller for a given working condition and wave sequence, although improvements in the numerical methods are still necessary to allow for a better and more detailed prediction of the different ventilation forms, which are for example observed in the MARINTEK experiments. One example for this, might be numerical models for two-phase flows, which consider an amount of non-condensible gas in the water, which possibly will allow for a more exact prediction of ventilation also in the lower blade positions. Furthermore, conceivable possible extensions of the coupling procedure might consider a variation of the

propeller pitch or characteristics of the machinery, to capture the working conditions of the propeller more realistically. Nevertheless, open questions are still remaining regarding the risk for ventilation, as long term investigations and statistical statements on the occurrence of ventilation can not be derived from the presented methods. Here, additional investigations using sea-keeping methods based on potential flow (for example strip theory or panel methods) might be a possibility to determine for example the probability of occurrence for an emergence of the propeller.

Bibliography

[1] Gothenborg 2010 - A Workshop on CFD in Ship Hydrodynamics. URL `http://www.gothenburg2010.org/`.

[2] Abdel-Maksoud, M., Brandt, H. and Hochkirch, K. Berechnung der turbulenten Strömung um einen vereinfachten Propeller. Technische Universität Berlin, Institut für Schiff- und Meerestechnik, 1995.

[3] Abdel-Maksoud, M., Menter, F. and Wuttke, H. Viscous Flow Simulations for Conventional and High-Skew Marine Propellers. *Ship Technology Research*, 45, pp. 64–71, 1998.

[4] Abdel-Maksoud, M. and Rieck, K. Calculation of the pressure reduction in the tip vortex core of a skew propeller in model and full-scale. In *4th Numerical Towing Tank Symposium (NuTTS01), Hamburg, Germany*. 2001.

[5] Abels, W. *Zuverlässige Prognose propellererregter Druckschwankungen auf die Außenhaut mittels Korrelation direkter Berechnung*. Ph.D. thesis, Hamburg University of Technology, 2006.

[6] Bauer, M., Greve, M., Druckenbrod, M. and Hundemer, J. *Dokumentation panMare (in german)*. Hamburg University of Technology, Institute for Fluid Dynamics and Ship Theory, 2010.

[7] Berchiche, N. and Janson, C.-E. Numerical Computations and Comparison to Experiments for a Propeller in Open-Water Condition. *Ship Technology Research*, 53, pp. 9–17, 2006.

[8] Bertram, V. *Practical Ship Hydrodynamics*. Butterworth - Heinemann, 2000.

[9] Bugalski, T. and Hoffmann, P. Numerical Simulation of the Interaction between Ship Hull and Rotating Propeller. In *Gothenborg 2010 A Workshop on Numerical Ship Hydrodynamics, Proceedings, Volume II*. 2010.

[10] Bugalski, T. and Hoffmann, P. Numerical Simulation of the Self-Propulsion Tests. In *Second International Symposium on Marine Propulsors (smp'11), Hamburg, Germany*. 2011.

[11] Califano, A. *Dynamic loads on marine propellers due to intermittent ventilation*. Ph.D. thesis, Norwegian University of Science and Technology, 2010.

[12] Califano, A. and Steen, S. Analysis of different propeller ventilation mechanisms by means of RANS simulations. In *First International Symposium on Marine Propulsors (smp'09), Trondheim, Norway*. 2009.

[13] Caponnetto, M. RANSE Simulations of Surface Piercing Propellers. In *Numerical Towing Tank Symposium (NuTTs)*. 2003.

[14] Carlton, J. *Marine Propellers and Propulsion*. Butterworth - Heinemann 2. Edition, 2007.

[15] Carrica, P., Castro, A. M. and Stern, F. Self-propulsion computations using a speed controller and a discretized propeller with dynamic overset grids. *Journal of Marine Science and Technology*, 2010.

[16] Carrica, P., Fu, H. and Stern, F. Self-Propulsion Free to Sink and Trim and Pitch and Heave in Head Waves of a KCS Model. In *Gothenborg 2010 A Workshop on Numerical Ship Hydrodynamics, Proceedings, Volume II*. 2010.

[17] Carrica, P. and Stern, F. DES Simulations of KVLCC1 in Turn and ZigZag Maneuvers with Moving Propeller and Rudder. In *SIMMAN 2008*. 2010.

[18] Castro, A. M., Carrica, P. and Stern, F. Full Scale Self-Propulsion Computations with Discretized Propeller on Kriso Container Ship KCS. In *Gothenborg 2010 A Workshop on Numerical Ship Hydrodynamics, Proceedings, Volume II*. 2010.

[19] Chao, K.-Y. Numerische Propulsionsversuche. *Hansa*, 137, 9, pp. 168–174, 2000.

[20] Cieslawski, M. *Erweiterung des RANSE-Lösers FreSCo$^+$ zur Simulation nichtlinearer Wellendynamik*. Bachelor thesis (in german), Hamburg University of Technology, 2011.

[21] Clauss, G. F., Stück, R., Stempinski, F. and Schmittner, C. Computational and experimental simulation of nonbreaking and breaking waves for the investigation of structural loads and motions. In *International Conference on Offshore Mechanics and Arctic Engineering (OMAE)*, 2006-92238. 2006.

[22] Clement, A. Coupling of Two Absorbing Boundary Conditions for 2D Time-Domain Simulations of Free Surface Gravity Waves. *J. Computational Physics*, 126, pp. 139–151, 1996.

[23] Committee, S. Recommended Procedures for Resistance, Propulsion and Propeller Open Water Tests. International Towing Tank Conference, 2002.

[24] Drazyk, W. *Parameterstudie zur Bestimmung der Steuergrößen in Seegangsrandbedingungen für RANS Simulationen*. Student project (in german), Hamburg University of Technology, 2010.

[25] Duncan, J. H. The breaking and non-breaking wave resistance of a two-dimensional hydrofoil. *Journal of Fluid Mechanics*, 126, pp. 507–520, 1983.

[26] Fahrbach, M. *Bewertung der Güte von Nachstromfeldern (in german)*. Master's thesis, Hamburg University of Technology, 2004.

[27] Faltinsen, O. M. *Sea Loads on Ships and Offshore Structures*. Cambridge Univ. Press, Cambridge, UK, 1990.

[28] Faltinsen, O. M., Minsaas, K. J., Liapis, N. and Skjordal, S. Prediction of Resistance and Proppulsion of a Ship in a Seaway. In *13th Symposium on Naval Hydrodynamics, Tokyo, Japan*. 1980.

[29] Ferziger, J. and Peric, M. *Computational Methods for Fluid Dynamics*. Springer, 1996.

[30] Fleischer, K. Freifahrtversuche bei Unterdruck mit teilgetauchten Propellern. Versuchsanstalt für Wasserbau und Schiffbau, Berlin, 1979. Bericht in Bibliothek verfügbar, Nummer 3209-408 4.

[31] Gentaz, L., Allesandrini, B., Ferrant, P. and Luquet, R. Numerical simulation of the 3D viscous flow around a vertical cylinder in non-linear waves using explicit incident wave model. In *International Conference on Offshore Mechanics and Acrtic Engineering (Paper 2004-51098)*. Vancouver, Canada, 2004.

[32] Givoli, D. and Neta, B. Hig-order non-reflecting boundary conditions for dispersive waves. *Wave Motion*, 37, 3, pp. 257–271, 2003.

[33] Greve, M., Abdel-Maksoud, M., Eder, S. and Causmaecker, J. D. Unsteady viscous flow calculation around the KCS-model with and without propeller under consideration of the free surface. In *Gothenborg 2010 A Workshop on Numerical Ship Hydrodynamics, Proceedings, Volume II*. 2010.

[34] Hafermann, D. and Marzi, J. Propulsion Enhancements for a Greener Environment. In *Second International Symposium on Marine Propulsors (smp'11), Hamburg, Germany*. 2011.

[35] Hally, D. and Laurens, J.-M. Numerical Simulation of Hull-Propeller Interaction Using Force Fileds within Navier-Stokes Computations. *Ship Technology Research*, , 45, pp. 28–36, 1998.

[36] Han, K.-J. *Numerical optimization of hull/propeller/rudder configurations*. Ph.D. thesis, Department of Shipping and Marine technology, Chalmers University of Technology, 2008.

[37] Hess, J. Panel methods in computational fluid dynamics. *Annual Review of Fluid Mechanics*, 22, pp. 255–274, 1990.

[38] Isay, W. H. Zur Theorie des Propellers mit aus dem Wasser herausschlagenden Flügeln (in german). Schriftenreihe Schiffbau, Hamburg University of Technology, 1966.

[39] KEMPF, G. *Immersion of propellers*. North East Coast Inst. of Engineers and Shipbuilders, 1934.

[40] KIM, K.-H. Simulation of Surface Ship Dynamics Using Unsteady RANS Codes. In *RTO AVT Symposium on "Reduction of Military Vehicle Acquisition Time and Cost through Advanced Modelling and Virtual Simulation" RTO-MP-089*. 2002.

[41] KINNAS, S. A. and YOUNG, Y. L. Modelling of cavitating or ventilated flows using BEM. *International Journal of Numerical Methods for Heat and Fluid Flow*, 13, 6, pp. 672–697, 2003.

[42] KLEEFSMAN, T. *Water impact loading on offshore structures*. Ph.D. thesis, Rijksuniversiteit Groningen, the Netherlands, 2005.

[43] KOLIHA, N. *Entwicklung eines 6DOF-Moduls auf Basis von Quaternionen zur Simulation freier Bewegungen schwimmender Körper*. Bachelor thesis (in german), Hamburg University of Technology, 2011.

[44] KOUSHAN, K. Environmental and interaction effects on propulsion systems used in dynamic positioning, an overview. In *9th Symposium on Practical Design of Ships and Other Floating Structures, Luebeck-Tavemünde, Germany*. 2004.

[45] KOUSHAN, K. Dynamics of Ventilated Propeller Blade Loading on Thrusters Due to Forced Sinusoidal Heave Motion. In *26th Symposium on Naval Hydrodynamics Rome, Italy*. 2006.

[46] KOUSHAN, K. Dynamics of Propeller Blade and Duct Loading on Ventilated Thrusters in Dynamic Positioning Mode. In *Dynamic Positioning Conference*. 2007.

[47] KOUSHAN, K., SPENCE, S. and HAMSTAD, T. Experimental Investigation of the Effect of Waves and Ventilation on Thruster Loadings. In *First International Symposium on Marine Propulsors (smp'09), Trondheim, Norway*. 2009.

[48] KOUSHAN, K., SPENCE, S. and SAVIO, L. Ventilated Propeller Blade Loadings and Spindle Moment of a Thruster in Calm Water and Waves. In *Second International Symposium on Marine Propulsors (smp'11), Hamburg, Germany*. 2011.

[49] KOZLOWSKA, A., STEEN, S. and KOUSHAN, K. Classification of Different Type of Propeller Ventilation and Ventilation Inception Mechanism. In *First International Symposium on Marine Propulsors (smp'09), Trondheim, Norway*. 2009.

[50] KOZLOWSKA, A. ET AL. Numerical and Experimental Study of Propeller Ventilation. In *Second International Symposium on Marine Propulsors (smp'11), Hamburg, Germany*. 2011.

[51] KRÖGER, P. *Simulation der Rollbewegung von Schiffen*. Ph.D. thesis, Institut fuer Schiffbau der Universität Hamburg, 1987.

[52] KRÜGER, S. Grundlagen der Propulsion. Hamburg University of Technology, 2004.

[53] Lee, J. H. and Rhee, S. H. Flexible CFD Meshing Strategy for Prediction of Ship Resistance and Propulsion Performance. In *Gothenborg 2010 A Workshop on Numerical Ship Hydrodynamics, Proceedings, Volume II*. 2010.

[54] Lerbs, H. On the Effects of Scale and Roughness on Free Running Propellers. *Journal of the American Society of Naval Engineers*, 1951.

[55] Magnus, K. and Müller, H. *Grundlagen der Technischen Mechanik*. Teubner Studienbücher Mechanik, 1990.

[56] Manzke, M. *Numerical Simulation of Unsteady Body Motion in Turbulent Flow*. Master's thesis, Hamburg University of Technology, 2008.

[57] Manzke, M., Will, J. and Rung, T. Efficient Viscous Wave Resistance Analysis. In *Proceedings of the 11th International Symposium on Practical Design of Ships and other Floating Structures (PRADS)*, Paper 2010-2253. 2010.

[58] Manzke, M. et al. Efficient viscous simulation approaches to maneuvring in seaways. In *Assesment of stability and control prediction methods for air and sea vehicles*, AVT specialists meeting (AVT189), North Atlantic Treaty Organisation. 2011.

[59] Minsaas, K. J., Wermter, R. and Hansen, A. Scale Effects on Propulsion Factors. In *Report of Performance Committee*. International Towing Tank Conference, 1975.

[60] Morino, L., Chen, L.-T. and Suciu, E. Steady and Oscillatory Subsonic and Supersonic Aerodynamics around Complex Configurations. *AIAA Journal*, 13, 3, pp. 368–374, 1974.

[61] Müller, S.-B. *Numerische Untersuchung der Maßstabseffekte an Schiffspropellern*. Ph.D. thesis, Universität Duisburg-Essen, 2010.

[62] Müller, S.-B. et al. Comparing a Propeller Model with a Rotating Propeller in a CFD-Simulation of the Viscous Flow around a Ship. In *9th Numerical Towing Tank Symposium*. 2006.

[63] Muscarin, R. and Di Mascio, A. Numerical simulation of the flow past a rotating propeller behind a hull. In *Second International Symposium on Marine Propulsors (smp'11), Hamburg, Germany*. 2011.

[64] Muzaferij, S. and Peric, M. Computation of free-surface flows using interface-tracking and interface-capturing methods. In *Nonlinear Water Wave Interaction*, pp. 59–100. WIT-Press, 1999.

[65] Palm, M., Jürgens, D. and Bendl, D. Numerical and Experimental Study on Ventilation for Azimuth Thrusters and Cycloidal Propellers. In *Second International Symposium on Marine Propulsors (smp'11), Hamburg, Germany*. 2011.

[66] Pankajakshan, R. et al. Validation of Control Surface Induced Submarine Maneuvering Simulations using UNCLE. In *Proceedings of the Twenty-Fourth Symposium of Naval Hydrodaynamics (2003)*. 2003.

[67] Paterson, E., Wilson, R. and Stern, F. General-Purpose Parallel Unsteady RANS Ship Hydrodynamics CODE: CFDShip-Iowa. IIHR-Hydroscience and Engineering, College of Engineering, The University of Iowa, USA, 2003.

[68] Pereira, R. Simulation nichtlinearer Seegangslasten. *Schiffstechnik*, 35, pp. 173–193, 1988.

[69] Phillips, A. B., Turnock, S. R. and Furlong, M. Evaluation of manoeuvring coefficients of a self-propelled ship using a blade element momentum propeller model coupled to a Reynolds averaged Navier Stokes flow solver. *Ocean Engineering*, 36, pp. 1217–1225, 2009.

[70] Rhee, S. H. Unsteady Reynolds Averaged Navier-Stokes Method for Free Surface Wave Flows around Surface Piercing Cylindrical Structures. *Journal of Waterway, Port, Coastal and Ocean Engineering*, 2009.

[71] Rhie, C. and Chow, W. A numerical study for the turbulent flow past an isolated airfoil with trailing edge separation. *AIAA Journal*, 26, 17, pp. 1525–1531, 1983.

[72] Rung, T. et al. Challenges and Perspectives for Maritime CFD Applications. *Jahrbuch der Schiffbautechnischen Gesellschaft*, 103, 2009.

[73] Schellin, T. E. and El Moctar, O. Numerical prediction of impact-related loads on ship. *Journal of offshore mechanics and arctic engineering*, 129, pp. 39–47, 2007.

[74] Schetz, J. A. and Favin, S. Numerical Solution for the Near Wake of a Body with Propeller. *Journal of Hydronautics*, 11, 4, pp. 136–141, 1977.

[75] Schetz, J. A. and Favin, S. Numerical Solution of a Body-Propeller Combination Flow including Swirl and Comparison with Data. *Journal of Hydronautics*, 13, 2, pp. 46–51, 1979.

[76] Shiba, H. Air-Drawing of Marine Propellers. Transportation technical Research Institute, Japan, 1953.

[77] Simonsen, C. and Carstens, R. RANS Simulation of the flow around a ship appended with rudder, ice fins and rotating propeller. In *11th Numerical Towing Tank Symposium (NuTTs11), Brest, France*. 2008.

[78] Söding, H. Boundary Element Methods for Seakeeping. *Contribution to the Lectures on Seakeeping and Sea Loads*, Duisburg, Germany, 2010.

[79] Sparenberg, J. On the Potential Theory of the Interaction of an Actuator Disk and a Body. *Journal of Ship Research*, 16, pp. 271–277, 1972.

[80] Sparenberg, J. On the Linear Theory of an Actuator Disk in a Viscous Fluid. *Journal of Ship Research*, 18, 1, pp. 16–21, 1974.

[81] Stern, F. and Kim, H. Computation of Viscous Flow around a Propeller-Shaft Configuration with Inifinite-Pitch Rectangular Blades. In *Proceesings of the fifth International Conference on Numerical Ship Hydrodynamics*. 1990.

[82] Stern, F., Kim, H., Patel, V. and Chen, H. A Viscous-Flow Approach to the Computation of Propeller-Hull Interaction. *Journal of Ship Research*, 32, 4, pp. 246–262, 1988.

[83] Strunk, H. Systematische Freifahrtversuche mit teilgetauchten Propellern unter Druckähnlichkeit. Versuchsanstalt für Wasserbau und Scgiffbau, Berlin, 1986. In Bibliothek verfügbar, Nr. 3222-819 3.

[84] Stück, A., Kröger, J. and Rung, T. Adjoint-based Hull Design for Wake Optimisation. *Ship Technology Research*, 58(1), pp. 34–44, 2011.

[85] Vorhölter, H. *Numerische Analyse des Nachstroms und der Propellereffektivität am manövrierenden Schiff (in german)*. Ph.D. thesis, Hamburg University of Technology, 2011.

[86] Wagner, H. Über die Entstehung des dynamischen Auftriebes von Tragflügeln. *Zeitschrift fur angewandte Mathematik und Mechanik*, 5(1), pp. 17–35, 1925.

[87] Wellens, P., Luppes, R., Veldman, A. and Borsboom, M. CFD Simulations of a Semi-Submersible with Absorbing Boundary Conditions. In *International Conference on Offshore Mechanics and Acrtic Engineering (Paper 2009-79342)*. 2009.

[88] Wilcox, D. C. *Turbulence Modeling for CFD*. DCW Industries, Inc., La Cañada, 1993.

[89] Wöckner-Kluwe, K. Investigation of Propeller Ventilation with Viscous-Flow Methods. In *Dritter Interdisziplinärer Workshop Maritime Systeme, Technische Universität Hamburg-Harburg*. 2011.

[90] Xing-Kaeding, Y. *Unified Approach to Ship Seakeeping and Maneuvring by a RANSE Method*. Ph.D. thesis, Hamburg University of Technology, 2006.

[91] Yeung, R. and Hamilton, J. A spectral-shell solution for visous wave-body interactions. In *24th Symposium on Naval Hydrodynamics*. 2002.

[92] Young, Y. L. and Kinnas, S. A. Numerical Analysis of Surface-Piercing Propellers. In *SNAME 2003 Propeller and Shafting Symposium, Virginia Beach, USA*. 2003.

[93] Zawadzki, I., Fuhs, D. and Gorski, J. Integration of a viscous flow rans solver with an unsteady propulsor force code. Carderock Division, Naval Surface Warfare Center, 1997.